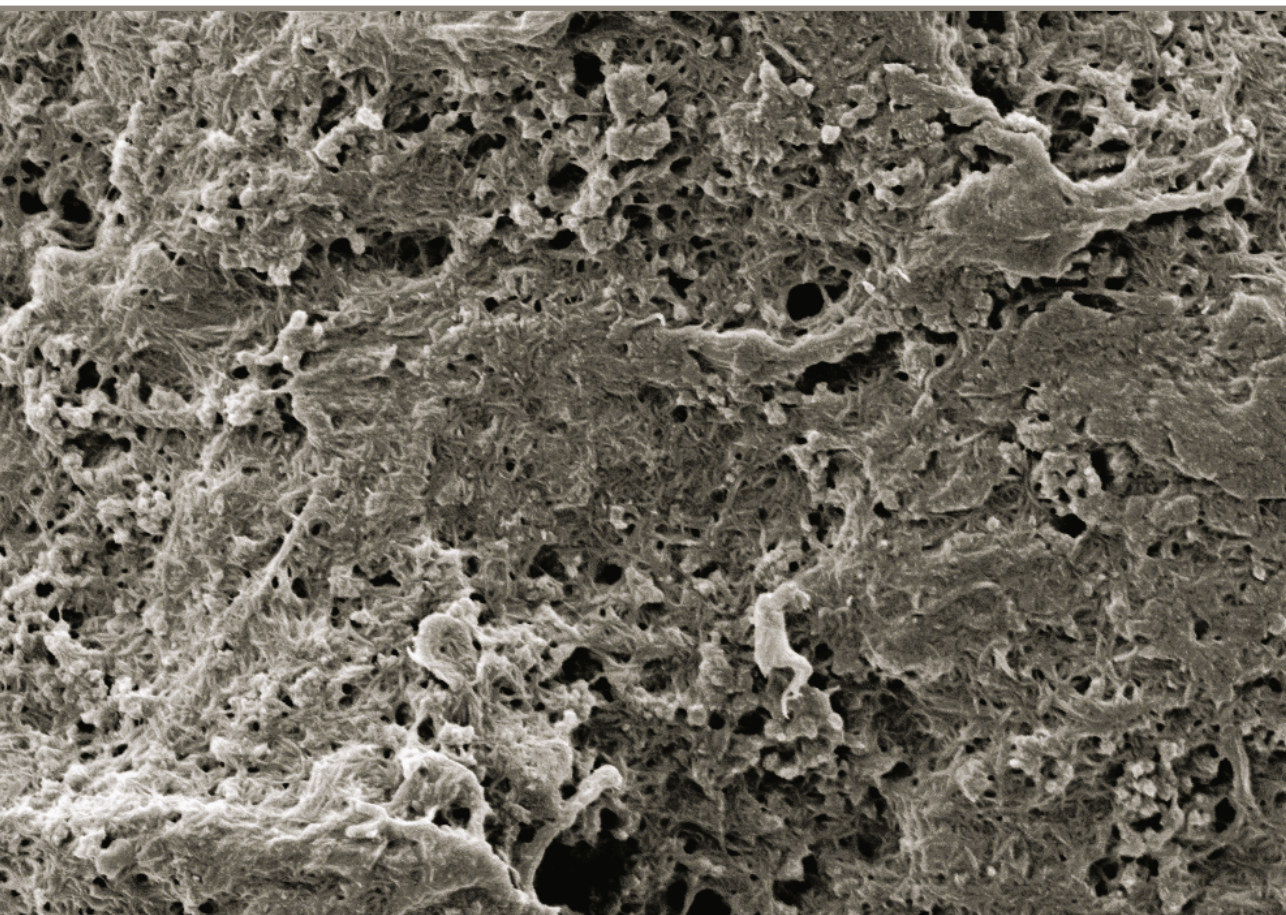**Anda Barkāne**

PHOTO-CURABLE VEGETABLE OIL-BASED ACRYLATE RESINS WITH LIGNOCELLULOSE COMPONENTS

Summary of the Doctoral Thesis

RIGA TECHNICAL UNIVERSITY

Faculty of Natural Sciences and Technology
Institute of Chemistry and Chemical Technology

Anda Barkāne

Doctoral Student of the Study Programme "Chemistry, Materials Science and Engineering"

PHOTO-CURABLE VEGETABLE OIL-BASED ACRYLATE RESINS WITH LIGNOCELLULOSE COMPONENTS

Summary of the Doctoral Thesis

Scientific supervisor
Professor Dr. sc. ing.
SERGEJS GAIDUKOVS

RTU Press
Riga 2024

The materials were investigated, prepared, and tested at Riga Technical University Institute of Chemistry and Chemical Technology.

ACKNOWLEDGEMENTS

One step at a time is all it takes to get you there.
/*Emily Dickinson*/

DOCTORAL THESIS PROPOSED TO RIGA TECHNICAL UNIVERSITY FOR PROMOTION TO THE SCIENTIFIC DEGREE OF DOCTOR OF SCIENCE

To be granted the scientific degree of Doctor of Science (Ph. D.), the present Doctoral Thesis has been submitted for defence at the open meeting of RTU Promotion Council on 15 May 2024 at 13.00 at the Faculty of Natural Sciences and Technology of Riga Technical University, Paula Valdena Street 7, Room 272.

OFFICIAL REVIEWERS

Associate Professor Dr. Ingars Reinholds
University of Latvia, Latvia

Professor Dr. Alexander Bismarck
University of Vienna, Austria

Dr. Tobias Robert
Fraunhofer Institute for Wood Research, Germany

DECLARATION OF ACADEMIC INTEGRITY

I hereby declare that the Doctoral Thesis submitted for review to Riga Technical University for promotion to the scientific degree of Doctor of Science (Ph. D.) is my own. I confirm that this Doctoral Thesis has not been submitted to any other university for promotion to a scientific degree.

Anda Barkane ……………………………. (signature)

Date: ………………………

The Doctoral Thesis has been written in English, and the has a total of 174 pages. Doctoral Thesis consists of an Introduction, Literature Review, Materials and Methods, Results and Discussion, Conclusions, 51 figures, 12 tables, and schematics 6. The Bibliography contains 340 titles.

TABLE OF CONTENTS

ABBREVIATIONS

A	Adhesion factor
AC	Acryloyl chloride
AESO	Acrylated epoxidized soybean oil
AM	Additive manufacturing
C	Nanocrystalline cellulose
$C*$	Filler-matrix stress efficiency transfer parameter
$DBC\%$	Double bond conversion rate
DMA	Dynamic mechanical analysis
DMAc	N,N-dimethylacetamide
DMF	N,N-dimethylformamide
E'_c	Storage modulus for composite (95 °C)
E'_g	Storage modulus at glassy state (–45 °C)
E'_m	Storage modulus for polymer matrix (95 °C)
E'_v	Storage modulus at viscoelastic/rubbery state (95 °C)
F	Nanofibrillated cellulose
FTIR	Fourier transform infrared spectroscopy
H	Hemicellulose
HMDI	Hexamethylene diisocyanate
HDDA	1,6-hexanediol diacrylate
L	Lignin
LiCl	Lithium chloride
M_c	Molecular weight between crosslinks
N	Crosslinking density
pC	Nanocrystalline cellulose from filter paper
pCI	Nanocrystalline cellulose from filter paper functionalized with isocyanate
PI	Photoinitiator
pF	Nanofibrillated cellulose from filter paper
pFA	Acrylated nanofibrillated cellulose from filter paper
r	Reinforcement parameter
SEM	Scanning electron microscopy
SLA	Stereolithography apparatus
tanδ	Loss factor
T_g	Glass transition temperature
TGA	Thermogravimetric analysis
TMPTA	Trimethylolpropane triacrylate
TPO	2,4,6-trimethylbenzoyldiphenylphosphine oxide
UV-Vis	Ultraviolet-visible light
V_f	Nanofiller volume fraction in the composite
wt%	Weight percent
YI	Yellowing index

INTRODUCTION

In recent years, bio-based acrylates, especially those derived from vegetable oils, have gained prominence within polymer chemistry due to their renewability. These materials are increasingly recognized for their potential to reduce reliance on petroleum resources. However, there are still some performance properties challenges, such as mechanical and thermal durability, weathering resistance, and interface compatibility. These issues can be effectively addressed by incorporating lignocellulose components, such as nanocellulose, hemicellulose, and lignin. Surface functionalization of nanocellulose with hydrophilic groups is crucial for improving the compatibility with the hydrophobic acrylate matrix. This work highlights the significance of bio-based acrylates, emphasizing their role in modern markets and their ability to enhance performance characteristics through the strategic use of lignocellulose constituents and nanocellulose surface functionalization. Moreover, these bio-based acrylate lignocellulose composites hold promise in various applications, including film production, coatings, and UV-assisted 3D printing, aligning with the growing demand for bio-based materials across industrial sectors.

The Doctoral Thesis focuses on the development of lignocellulose composites using vegetable oil-based acrylate resins. As a reinforcing filler, it assesses various lignocellulose components, including nanocellulose, hemicellulose, lignin, and recycled cellulose. The Thesis also explores the chemical surface functionalization of cellulose to address hydrophobicity issues. Notably, the transformation of cellulose into nanoscale particles demonstrates exceptional properties with promising applications, while maintaining precision in 3D printing. Mechanical testing reveals substantial improvements in performance due to nanocellulose reinforcement. Hemicellulose's potential as a nonreactive diluent is also highlighted. The extensive range of composite resin formulations developed in this study offers a versatile platform for systematic selection and optimization of performance properties.

Within the Doctoral Thesis, two distinct strategies are employed for preparing vegetable oil-based acrylate/lignocellulose composites: film curing for highly loaded compositions (up to 30 wt%) and UV-assisted 3D printing for lower loading (down to 0.1 wt%) compositions. Both methods utilize UV-light curing, reducing the energy requirements for sample preparation. The Thesis extensively examines the impact of lignocellulose fillers on mechanical and thermomechanical properties, thermal stability, and accelerated weathering endurance. Changes in double bond conversion rate and crosslinking degree are meticulously analyzed. The effectiveness of chemical surface functionalization of nanocellulose in enhancing the interface is investigated through mechanical performance and reinforcing efficiency analysis. Sample morphology and printing accuracy are evaluated using scanning electron microscopy and optical microscopy.

Aim of the Doctoral Thesis

To utilize bio-based resources and UV-light assisted sustainable technologies to develop acrylated epoxidized soybean oil/lignocellulose nanocomposite resin materials with enhanced performance compared to other bio-based acrylate resin materials.

Tasks of the Doctoral Thesis

1. To formulate bio-based liquid resin from lignocellulose nanoparticles and bio-based acrylated epoxidized soybean oil (AESO) and reactive diluents, which are suitable for UV-light assisted curing of film/coating and 3D printing applications.
2. To assess AESO nanocomposite materials containing different contents of single and hybrid combinations of nanocrystalline cellulose, nanofibrillated cellulose, hemicellulose, and lignin.
3. To test resins' processing properties, such as 3D printing accuracy and resolution, UV-light curing efficiency, and cured materials' performance properties like crosslinking degree, thermal, thermomechanical, and mechanical properties of the obtained resin materials for film and 3D printing processing.
4. To develop different nanocellulose surface functionalization methods to enhance the compatibility and interaction with the polymer matrix.
5. To evaluate the durability and accelerated weathering of obtained nanocellulose-polymer composites.

Thesis statements to be defended

1. The addition of reactive diluents (1,6-hexanediol diacrylate (HDDA) and trimethylolpropane triacrylate (TMPTA) to acrylated epoxidized soybean oil (AESO) results in increased performance, and UV-curable formulations have potential for coating/film and 3D printing applications.
2. The good processing and outstanding performance properties of AESO/lignocellulose resin materials are tuned up by using lignocellulose fillers to outperform other bio-based acrylate resins, and hybrid combinations present significant advantages by reducing the total filler loading and benefitting the mechanical, thermal, wetting and durability performance characteristics.
3. Ultra-low loads of nanocellulose in AESO resin for 3D printing applications ensure their outstanding mechanical performance and long-term durability.
4. Surface functionalization of nanocellulose significantly enhances compatibility with the resin and improves composite materials' exploitation properties.
5. The introduction of nanofibrillated cellulose increased the durability and resistance to accelerated weathering of obtained nanocellulose-polymer composites.

Scientific novelty

1. Demonstration of novel bio-based composites as an alternative to fossil-based plastics for high-performance applications.
2. Demonstration of lignocellulose filler benefit for AESO resins UV-light processing and performance.
3. Development of a UV-light-assisted stereolithography 3D printing process for vegetable oil-based/nanocellulose composites.
4. Development of different functionalization routes for nanocellulose crystals and fibrils to regulate the mechanical performance properties of the 3D printed composite materials.
5. In-depth analysis of accelerated weathering effect on UV-light cured AESO/nanocellulose composite materials.

Practical significance

1. Development of a bio-based AESO resin with enhanced processing and performance properties to replace petroleum-based acrylates used in photocuring applications.
2. Increase of mechanical performance with the introduction of lignocellulose components into the resin formulation.
3. Validation of the developed resin for 3D printing and film/coating production.
4. The shown nanocellulose surface functionalization methods improve the nanocellulose reinforcement efficiency for bio-based acrylate resin.
5. Determinate the 3D printed materials' mechanical performance after weathering the composite material.

Approbation of the Thesis in Scopus and Web of Science indexed articles

Literature review
1. S. Briede, **A. Barkane**, M. Jurinovs, V. K. Thakur, S. Gaidukovs, Acrylation of biomass: A review of synthesis process: Know-how and future application directions. Current Opinion in Green and Sustainable Chemistry 35 (2022) 100626.
   Section 3.1.1.
2. **A. Barkane,** O. Platnieks, M. Jurinovs, S. Kasetaite, J. Ostrauskaite, S. Gaidukovs, Y. Habibi, UV-light curing of 3D printing inks from vegetable oils for stereolithography. Polymers 13 (2021) 1195, doi:10.3390/polym13081195
   Section 3.2.1.
3. **A. Barkane,** O. Platnieks, L. Grase, S. Gaidukovs, Simultaneous wettability and stiffness control of UV-curing vegetable oil resin composites by lignocellulosic components. Polymer 255 (2022) 125154, doi:10.1016/j.polymer.2022.125154
4. **A. Barkane,** E. Kampe, O. Platnieks, S. Gaidukovs, Cellulose Nanocrystals vs. cellulose nanofibers: A comparative study of reinforcing effect in UV-cured vegetable oil nanocomposites. Nanomaterials, 11 (2021) 1791, doi:10.3390/nano11071791

Section 3.2.2.

5. **A. Barkane,** E. Kampe, S. Gaidukovs, New reinforcing approach for biobased UV-curing resins: hybrid lignocellulose fillers with improved synergy and wood structure mimics. ACS Sustainable Chemistry & Engineering, 11 (17) (2023), 6578, doi:10.1021/acssuschemeng.2c07288

   Section 3.3.1.

6. **A. Barkane**, M. Jurinovs, O. Starkova, L. Grase, D. F. Schmidt, S. Gaidukovs, Enhancing stiffness, toughness and creep in a 3D printed bio-based photopolymer using ultra-low contents of nanofibrillated cellulose. Journal of Composites Science, 7 (10) (2023) 435, doi:10.3390/jcs7100435

7. **A. Barkane,** M. Jurinovs, S. Briede, O, Platnieks, P. Onufrijevs, Z. Zelca, S. Gaidukovs, Biobased resin for sustainable stereolithography: 3D printed vegetable oil acrylate reinforced with ultra-low content of nanocellulose for fossil resin substitution. 3D Printing and Additive Manufacturing, (2022) 1–16, doi:10.1089/3dp.2021.0294

   Section 3.4.1.

8. M. Jurinovs, **A. Barkane,** O, Platnieks, S. Beluns, L. Grase, R. Dieden, M. Strapolim D. F. Schmidt, S. Gaidukovs, Vat photopolymerization of nanocellulose-reinforced vegetable oil-based resins: synergy in morphology and functionalization. ACS Applied Polymer Materials, 5 (4) (2023), 3104, doi:10.1021/acssapm.3c00245

   Section 3.5.1.

9. **A. Barkane,** O. Platnieks, J. Vecstaudza, S. Gaidukovs, Analysis of bio-based acrylate accelerated weathering: A study of nanocellulose impact on the bulk durability of 3D-printed nanocomposites. Materials Today Chemistry, 33 (2023) 101737, doi:10.1016/j.mtchem.2023.101737

Other Publications on the Topic that are not included in the Thesis

1. S. Briede, O. Platnieks, **A. Barkane**, I. Sivacovs, A. Leitans, J. Lungevics, S. Gaidukovs, Tailored biobased resins from acrylated vegetable oils for application in wood coatings. Coatings, 13 (2023)657, doi:10.3390/coatings13030657

2. **A. Barkane**, O. Platnieks, M. Jurinovs, S. Gaidukovs, Thermal stability of UV-cured vegetable oi epoxidized acrylate-based polymer system for 3D printing applications. Polymer Degradation and Stability 181 (2020) 109347, doi:10.1016/j.polymdegradstab.2020.109347

Dissemination in international scientific conferences

1. **A. Barkane,** O. Platnieks, S. Gaidukovs, Accelerated weathering of 3D-printed nanocomposites. RTU *64th International Scientific Conference - Materials Science and Applied Chemistry*, Riga, Latvia, October 6, 2023.

2. **A. Barkane,** S. Gaidukovs, New reinforcing approach for bio-based UV-curing resins: hybrid lignocellulose fillers with improved synergy and wood structure mimics. *38th*

International Conference of the Polymer Processing Society, St. Gallen, Switzerland, May 22–26, 2023.

3. **A. Barkane,** S. Gaidukovs, Photo crosslinking kinetics for bio-based 3D printing resins: FTIR vs. photorheology. *Nordic Rheology conference*, Aarhus, Denmark, April 12–14, 2023.

4. **A. Barkane,** O. Paltneiks, S. Gaidukovs, Comparison of Lignin, Hemicellulose and Nanocellulose as Green Additives to Reinforce Vegetable Oil Resins for UV Curing. *POLY-CHAR 2022 conference*, Online, May 22–25, 2022.

5. **A. Barkane,** M. Jurinovs, S. Gaidukovs, Bio-based, nanocellulose reinforced, UV-curable inks for additive manufacturing. *6th Green and Sustainable Chemistry Conference – Elsevier*, Online, November 16–18, 2021.

6. **A. Barkane,** S. Gaidukovs, Reinforcement Efficiency of Cellulose Nanofibers And Nanocrystal in UV-curable Vegetable Oil Polymer Matrix. *Riga Technical University 62nd International Scientific Conference – Materials Science and Applied Chemistry,* Riga, Latvia, Online, October 22, 2021.

7. **A. Barkane,** E. Kampe, M. Bleija, M. Jurinovs, Y. Habibi, S. Gaidukovs, Thermal properties of modified NFC bio-based photocurable polymer composites. *ACS Spring 2021 Macromolecular chemistry: The second century*, USA, online, April 5–16, 2021.

8. **A. Barkane,** E. Kampe, M. Jurinovs, Y. Habibi, S. Gaidukovs, Bio-based polymer nanocomposite for photopolymerization applications. *1st Greenering international conference*, Online, February 15–17, 2021.

9. **A. Barkane,** M. Jurinovs, Z. Zelca, Y. Habibi, S. Gaidukovs, Nanocellulose filled acrylated epoxidized soybean oil inks for UV-assisted 3D printing. *Functional Materials and Nanotechnologies FM&NT-2020* Vilnius, Lithuania, online, November 23–26, 2020.

10. **A. Barkane,** E. Kampe, Y. Habibi, S. Gaidukovs, Photopolymerization of epoxidized soybean oil acrylate / lignocellulose biocomposites. *Materials Science and Applied Chemistry-2020,* Riga, Latvia, online, October 23, 2020.

11. E. Kampe, **A. Barkane,** S. Gaidukovs, Y. Habibi, Photopolymerization of epoxidized soybean oil acrylate / lignocellulosic biocomposites. *Riga Technical University 61st International Scientific Conference – Materials Science and Applied Chemistry*, Riga, Latvia, October 23, 2020.

12. **A. Barkane,** O. Platnieks, Y. Habibi, S. Gaidukovs, UV-assisted additive manufacturing of lignocellulosic nanomaterials. *ACS Fall 2020 Virtual Meeting & Expo – Moving chemistry from bench to market* online, USA, August 17–20, 2020.

1. LITERATURE OVERVIEW

Acrylic resins dominate the resin market, representing 74 % of resin usage based on *SpecialChem's* 2020 market research [1]. Vegetable oils have emerged as promising, abundant, renewable, and cost-effective resources within this context, offering structural attributes that make them an appealing and sustainable foundation for diverse intermediates and products [2, 3]. Modified vegetable oils derived from sources like soybean, grapeseed, linseed, and rapeseed serve as viable alternatives to fossil-based thermoset polymer resins [4, 5]. These modified oils can undergo radical polymerization, and acrylates and methacrylates are among the most reactive monomers suitable for UV-initiated photopolymerization [6–9]. Common methods involve acrylation or similar functionalization reactions to introduce polymerizable groups to vegetable oil molecules [10, 11]. Utilizing acrylic derivatives of vegetable oils and cellulose, both naturally obtained materials, yields durable bio-based polymers with diverse exploitable properties and wide-ranging applications.

Vegetable oil-based polymers find applications in adhesives [12], plasticizers [13], lubricants [14], resins [15], nanocomposite matrices [16, 17], and coatings [18]. Acrylation of plant oils enhances their reactivity and introduces additional oxygen atoms, making them suitable for producing thermoset polymers [19]. Bio-based acrylate resin exhibit competitive performance compared to petroleum-based counterparts [20–25]. Acrylated epoxidized soybean oil (AESO) has been commercialized and is available under the trademark *Ebecryl 860* as a relatively competitive solution for coatings and UV-assisted additive manufacturing (AM) [26–28]. AESO polymer prepared by UV-light-assisted 3D printing technologies like stereolithography (SLA) and digital light processing methods (DLP) have been evaluated and compared with commercial 3D printing resin's mechanical performance and are still lacking [28, 29].

Commonly oil component develops a polymer matrix, while cellulose is applied as a reinforcing filler [16, 17]. Lignocellulose comprises cellulose (40–50 %), hemicellulose (25–35 %), and lignin (15–20 %) [30, 31]. Acrylate resin commonly employ nanocrystalline cellulose (C) and cellulose nanofibrils (F) as primary fillers to reinforce acrylic resin [32–35]. However, hemicellulose and lignin (L) have been less explored in UV-curing resin composites. Hemicellulose, forming polymer blends, should not be discounted as a diluent for UV-curable polymer compositions, offering tunable barrier properties and compatibility between the nanocellulose and the polymer matrix [36, 37].

Due to L's UV-light absorption properties, it remains relatively underexplored in UV-curing resin, despite possessing excellent water and UV-light barrier properties along with thermal stability and strong interfacial adhesion with polymers related to the hydrophobic nature [38, 39]. Therefore, investigating hemicellulose and L in UV-curable resins is crucial to unleashing their potential. A promising avenue involves creating hybrid lignocellulosic fillers for UV-curable resins, combining nanocellulose to counter L's UV-light absorbance and reinforce the polymer matrix. Hemicellulose, acting as a nonreactive diluent, can reduce resin viscosity, benefiting UV-curing [40]. Moreover, integrating hybrid lignocellulose fillers can offer wood-like properties, expanding their potential in coating applications or UV-light-based 3D printing technologies [41] and presenting numerous versatile applications.

IDTechEx projects a global 3D printing materials market worth \$29.5 billion by 2032 [42]. The first 3D printing technique, SLA, was pioneered and patented by Charles (Chuck) Hull et al. in 1984 [43]. SLA involves a laser-assisted process using a container filled with liquid photopolymerizable resin, a lowering platform, and a sweeper for even resin layer distribution [44]. It employs a light source for selective curing, solidifying the resin layer by layer. Finding bio-based materials suitable for SLA proves challenging due to its reliance on photopolymerizable resin [45] and the scarcity of sustainable feedstocks [46, 47]. While vegetable oil-based resin exhibit printing accuracy akin to costly high-resolution commercial resin, the resulting mechanical properties, particularly with AESO, may be relatively poor [48]. Various cellulose fibers are common fillers in polymer composites, including photocurable resins [49–52]. However, the highly hydrophilic nature of nanocellulose compromises reinforcement efficiency in many AM resin, especially as they tend to be hydrophobic [50]. Nevertheless, advancements in nanocellulose-reinforced photocurable AM resin have been achieved through ongoing research and development [53–55].

Due to the highly hydrophilic nature of cellulose and the high aspect ratios of F, their tendency to agglomerate is much more pronounced than that of C [56]. However, if agglomeration is overcome and adequate dispersion is achieved, the higher aspect ratios of Fs promise more significant reinforcement [56, 57]. Nanocellulose has high stiffness and aspect ratios, and F has an even higher ratio than C, ensuring the ability to form a percolated filler network faster (~ 0.1 wt%) [58–60]. In addition, it can be argued that the production of Fs is more sustainable because it does not require treatment with strong acids or bases [61]. The hydrophilicity of nanocellulose fillers is a crucial factor that promotes their agglomeration [62]. The functionalization of nanocellulose is considered a promising solution [33, 63]. Functionalization efforts to date have been focused mainly on C [33, 64], with a relative lack of knowledge concerning the effects of F functionalization.

Understanding the aging behavior of bio-based acrylate polymers is paramount in various industries to ensure their adaptation, long-term performance, and durability. At an accelerated rate, QUV accelerated weathering equipment allows the reproduction of sunlight, rain, and dew-caused damage in samples [65]. Published research on the artificial weathering of UV-cured acrylate polymers has been devoted almost exclusively to coatings [66–69]. The investigations examined coating cracking, yellowing, gloss loss, and some chemical degradation processes occurring on the coating's surface. Bulk properties have not been investigated due to the small thickness of the layer. As a result, bulk properties affecting mechanical performance have not been investigated despite their extreme importance. Another aspect is that 3D printing introduces the concern of layer adhesion. In addition, the weathering of vegetable oil-based acrylic resin has not been investigated. However, vegetable oil-based acrylates, with their triglyceride form and ester bonds, are expected to act differently than widely investigated polyurethanes, epoxides, and systems with stabilizers [68, 70, 71].

2. MATERIALS AND METHODS

AESO-based resin	AESO-based resin + lignocellulose components (single filler)	AESO-based resin + lignocellulose components (hybrid filler)	AESO-based resin + nanofibrillated cellulose	AESO-based resin + functionalized nanocellulose
	Nanocellulose water suspension via solvent replacement with centrifugation and ultrasound transfered to acetone	Nanocellulose water suspension via solvent replacement with centrifugation and ultrasound transfered to acetone	Nanocellulose water suspension via solvent replacement with centrifugation and ultrasound transfered to acetone	Nanocellulose water suspension via solvent replacement with centrifugation and ultrasound transfered to acetone / DMAc / DMF
				Nanofibrillated cellulose acrylation Nanocrystalline cellulose isocianate functionalization
Magnetic stirrer for homogeneous → VO	Ultrasonification with magnetic stirrer for homogeneous VO + lignocellulose component suspension	Ultrasonification with magnetic stirrer for homogeneous VO + lignocellulose component suspension	Highshare mixer for homogeneous VO + nanocellulose suspension → degasification in vacuum	Highshare mixer for homogeneous VO + nanocellulose suspension → degasification in vacuum
AESO + photoinitiator (1, 3, 5, 7, wt%) AESO + M (30 wt% HDDA, 5 wt% TMPTA) + (1, 3, 5, 7, wt%)	VO + 5, 10, 20, 30 nanofibrillated cellulose nanocrystalline cellulose 5, 10 wt% hemicellulose lignin	VO + 10 wt% lignocellulose (5 wt% lignin + 5 wt% nanocrystalline cellulose (C) / nanofibrillated cellulose (F) / hemicellulose (H)) C3F3H1; C2F3H1; C3F1H1; C2F2H1; C1F3H1; C3F3H2; C3F2H2; C2F1H1; C3F2H3; C2F3H3; C2F1H3; C1F2H2; C3F1H3; C1F3H3; C2F1H3; C1F2H3; C1F1H3	VO + 0.1 wt% nanofibrillated cellulose 0.5 wt% nanofibrillated cellulose 1 wt% nanofibrillated cellulose	VO + 0.1 wt% nanofibrillated cellulose 0.1 wt% acrylated nanofibrillated cellulose 0.1 wt% nanocrystalline cellulose 0.1 wt% nanocrystalline cellulose with isocianate
Thin film obtaining with UV-light curing	Thin film obtaining with UV-light curing	Thin film obtaining with UV-light curing	UV-assisted 3D printing	UV-assisted 3D printing
Thin film samples (8.5 mm × 4 mm × 0.3 mm): FTIR (DBC%), DMA (T_g), density, sol-fraction	Thin film samples (8.5 mm × 4 mm × 0.3 mm): TGA (T_{max}, char yield), FTIR (DBC%, hydrogen bonding), DMA (T_g, M_c, N), density, sol-fraction, SEM, AFM, UV-Vis, water contact angle,	Thin film samples (8.5 mm × 4 mm × 0.3 mm): TGA (T_{max}, char yield, kinetics), FTIR (DBC%, hydrogen bonding), TGA-FTIR, DMA (T_g, M_c, N, Cole-Cole plot), density, sol-fraction, SEM, AFM, UV-Vis, water contact angle,	Printed, as per ISO-178 (80 mm × 10 mm × 4 mm), ISO 527-1BA (dog bone): viscosity, optical microscopy, TGA (T_{max}, char yield%), FTIR (DBC%, hydrogen bonding), DMA (M_c, N, C*, r, T_g, Cole-Cole), SEM, AFM, UV-Vis, TGA-FTIR, density, sol-fraction, tensile (toughness), flexural	Printed, as per ISO-178 (80 mm × 10 mm × 4 mm), ISO 527-1BA (dog bone): viscosity, optical microscopy, TGA (T_{max}, char yield%), FTIR (DBC%, hydrogen bonding), DMA (M_c, N, C*, r, A, T_g), SEM, AFM, UV-Vis, water contact angle, TGA-FTIR, density, sol-fraction, tensile (toughness)
UV-assisted 3D printing			VO + 0.1 wt% nanofibrillated cellulose 0.5 wt% nanofibrillated cellulose Accelerated weathering (0, 250 h, 500 h, 750 h, 1000 h)	
			Printed, as per ISO-178 (80 mm × 10 mm × 4 mm), ISO 527-1BA (dog bone): optical microscopy, FTIR, DMA (T_g), UV-Vis, density, sol-fraction, tensile, flexural, colorimetry, weight	

Scheme 2.1. The work schematics of the Doctoral Thesis.

2.1. Materials

2.1.1. Resin formulation

The neat resin was formulated from:
- acrylated epoxidized soybean oil (AESO) (specification: contains 4000 ppm monomethyl ether hydroquinone as an inhibitor, viscosity 18,000–32,000 cps., and density 1.04 g/mL) purchased from Merck KGaA (Darmstadt, Germany);
- 1,6-hexanediol diacrylate-technical grade (HDDA) (specification: contains 100 ppm monomethyl ether hydroquinone as an inhibitor, purity of > 77.5 %, molecular weight 226.27 g/mol, density 1.01 g/mL) purchased from Merck KGaA (Darmstadt, Germany);
- trimethylolpropane triacrylate (TMPTA) (specification: contains 600 ppm monomethyl ether hydroquinone as an inhibitor, purity of > 70.00 %, molecular weight 296.32 g/mol, density 1.10 g/mL) purchased from Merck KGaA (Darmstadt, Germany);
- 2,4,6-trimethylbenzoyldiphenylphosphine oxide (TPO) photoinitiator (PI) (specification: purity of 97.00 %, molecular weight 348.37 g/mol) obtained from Arkema Lambson (Wetherby, UK).

All chemicals were used as received without any additional purification.

2.1.2. Lignocellulose components for thin films

All lignocellulosic components used for thin film composite preparation were kindly provided by the Luxembourg Institute of Science and Technology (LIST) and used without any additional manipulations. Lignocellulosic components:
- lignin (L), powder;
- hemicellulose (H), H_2O suspension (13.5 wt%);
- nanocrystalline cellulose (C), H_2O suspension (3.0 wt%);
- nanofibrillated cellulose (F), H_2O suspension (3.0 wt%).

Other used chemicals: acryloyl chloride (AC) (stabilized with phenothiazine), N,N-dimethylacetamide (DMAc) (anhydrous, purity 99.8 %), lithium chloride (LiCl) (analysis grade), N,N-dimethylformamide (DMF) (purity 99.8 %), hexamethylene diisocyanate (HMDI) (purity > 98 %), hydrochloric acid (ACS reagent, 37 %), ethanol (96.6 %), were purchased from Sigma Aldrich. The materials were used as received.

2.1.3. Nanocellulose for 3D printing composites

Nanocellulose (C and F) used for 3D printing composite preparation was made in a lab from filter paper. Briefly, the preparation of C from filter paper was as follows: filter paper nanocrystalline cellulose (pC) – dry milling (ball mill) of cellulose and thermocatalytic degradation were applied to produce microcrystalline cellulose. Cellulose particles were then

suspended in a 0.05 % hydrochloric acid solution for degradation of the amorphous phase, washed, and dried. Afterwards, the dry powder was heated up to 110 °C to disrupt the cellulose structure slightly, and the powder was then milled for 15 h using JAR MILL 755RMV1 (US Stoneware, USA).

For C to prepare nanocellulose, a 1 wt% water suspension of microcellulose was processed using the high-shear fluid processor LM 20 Microfluidizer (Microfluidics, USA). A Z-shaped chamber with a diameter of 200 µm was used to microfluidize the suspension for five cycles at 30 000 PSI.

Filter paper nanofibrillated cellulose (pF) production differed. Cellulose shredding was used to obtain microcrystalline cellulose using a Retsch SM300 with a sieve size of 2.00 mm for the first pass-through and a 0.25 mm sieve for the second pass-through. The mill rotation speed was 1500 RPM. To prepare nanocellulose, a 1 wt% water suspension of microcellulose was processed using the high-shear fluid processor LM 20 Microfluidizer (Microfluidics, USA). A Z-shaped chamber with a diameter of 200 µm was used to microfluidize the suspension for five cycles at 30 000 PSI. The desired amount of prepared aqueous nanocellulose suspension was centrifuged for 15 min at 5000 RPM, and the water was then replaced with acetone. The exchange process was repeated 4 times, after which the obtained nanocellulose/acetone suspension was stored in a refrigerator.

All used lignocellulose fillers and their abbreviations are combined in Table 2.1. Their characterization was done with AFM and SEM. Lignocellulose components received from LIST have simple abbreviations like C, F, H, and LN for nanocrystalline cellulose, nanofibrillated cellulose, hemicellulose, and lignin, respectively. Nanocelluloses prepared from filter paper have "p" before the same abbreviations as for LIST lignocellulose components and additional "I" or "A" for the appropriate functionalization.

Table 2.1

Lignocellulose Fillers Used for Further Resin Formulations

Source	Lignocellulose filler	Abbreviation	Length, nm	Width, nm
Luxembourg	Nanocrystalline cellulose	C	256 ± 44	47 ± 9
	Nanofibrillated cellulose	F	488 ± 142	70 ± 18
	Hemicellulose	H	-	-
	Lignin	L	-	74 ± 16
Filter paper	Nanocrystalline cellulose	pC	275 ± 70	50 ± 14
	Nanocrystalline cellulose + isocyanate	pCI	349 ± 91	150 ± 32
	Nanofibrillated cellulose	pF	-	58 ± 12
	Nanofibrillated cellulose + acrylation	pFA	-	-

2.2. Sample preparation

2.2.1. Resin preparation

2.2.1.1. Neat resin formulation

The resin vegetable oil (VO) matrix was prepared as follows: photoinitiator was dissolved in acetone and then HDDA and TMPTA as reactive diluents and mechanical performance enhancers [72–74] and AESO resin were added. The resin contains the following: 65 wt%, 30 wt%, and 5 wt% of AESO, HDDA, and TMPTA, respectively, with 3 wt% of TPO.

2.2.1.2. Lignocellulose component preparation

Acetone was used as a solvent replacement for H_2O suspensions (C, F, H). Acetone was added to water suspensions and sonicated (UIS250V, Hielscher, Germany) for 5 min and then centrifuged at 5000 RPM for 15 min for complete separation. This solvent replacement procedure has been repeated a total of 4 times. L powder was dispersed in acetone using a sonification procedure with no solvent replacement.

2.2.1.3. Functionalization of nanocellulose

The nanocellulose acrylation was performed by a widely adopted method described in the literature [75–77]. First, freeze-dried pF (1 g) was mixed with 20 mL of anhydrous dimethylacetamide (DMAc) at 120 °C for 1 h. After that, the mixture was cooled down to 100 °C, and LiCl (2.4 g) was added. The resulting mixture was stirred for another 30 min; then, the mixture was cooled down to room temperature and stored overnight. Next, acryloyl chloride (AC, 3 g) was added dropwise to the homogenous solution in an ice/water bath for 1 h. After the pFA was added, the solution was mixed for 3 h, heated to 50 °C, and mixed for another 3 h. Afterwards, the solution was cooled to room temperature and the resulting product was precipitated in ethanol. The obtained acrylated pF (pFA) was vacuum filtered, thoroughly washed with ethanol for purification, and re-dispersed in acetone. The pFA was kept immersed in the solvent during filtration to avoid drying.

The isocyanate functionalization method described by Gafurov et al. was used for pC [78]. pC was solvent exchanged to DMF in the same manner as described above for pF. Next, pC (1 g) was suspended in a mixture of DMF (25 g) and HMDI (2.5 g). The suspension was heated to 110 °C and vigorously stirred for 4 h. Afterwards, the mixture was cooled down to 20 °C, ethanol (25 g) was added, then the solution was mixed for 30 min and vacuum filtered. For further purification, the obtained powder was washed with ethanol, vacuum filtered, solvent exchanged with acetone, and stored as a suspension. As a result, isocyanate functionalized pC (pCI) was obtained.

In the last step, the nanocellulose dispersion in acetone was added to the resin and mixed with a high-shear mixer for 5 min at 6000 RPM. Afterwards, the resin was placed in a vacuum

chamber at a vacuum of 1000 mbar for 2 h to remove all the excess air and remaining acetone. To prevent curing, the prepared resin was stored in a dark environment.

2.2.2. Film curing

The prepared resins (neat and composite) were applied to a glass substrate using an applicator with a thickness of 200–250 µm. Resin curing was performed with a 5.5 W UV-LED lamp with a 405 nm wavelength at a 2.5 cm distance between the UV-light source and the applied resin on the substrate.

2.2.3. 3D printing

An Original PRUSA SL1 (PRUSA research, Czech Republic) 3D masked stereolithography 3D printer was used for all 3D printed sample preparation. To print samples from the CAD models, a PRUSA SL1 printer was used, with a 5.5' LCD mask and a 25 W LED with a wavelength of 405 nm. Briefly, the 3D printing process consists of four steps. Firstly, the desired CAD model is created using CAD software. In the next step, the prepared CAD models are sliced into layers of a certain height (a layer thickness of 50 µm). Then, the sliced models are transferred to a 3D printer, and the desired 3D objects are produced. Finally, following printing, any remaining resin is washed off the printed part, and then the part is post-cured. All resins were subject to an optimization process to achieve the optimal printing time without defects or failures. The single-layer UV-light irradiation time was increased in 1 s increments, starting at 3.5 s, until parts were printed with no defects. In this way, optimum layer printing times of 8 s for the neat resin formulation and 15 s for the composite resin formulation were found. The first 10 layers of each sample were printed at a constant time of 35 s to ensure adhesion to the printing platform. After printing, all parts were washed in isopropanol and post-cured in a Prusa Curing and Washing Machine (CW1). It was equipped with four 52.8 W UV-LED strips with a wavelength of 405 nm. The washing and drying time was 5 min, while the post-curing time was maintained at 3 min.

2.3. Testing methods

Fourier transform infrared spectroscopy performed in attenuated total reflectance mode

Photopolymerization kinetics was evaluated with a Nicolet 6700 (Thermo Scientific, Germany) Fourier transform infrared spectroscopy (FTIR) spectrometer, and the functionalization of the nanocellulose and the filler-matrix interactions was analysed. FTIR was measured using the attenuated total reflectance (ATR) method. Sixteen parallel measurements were taken with a 4 cm^{-1} resolution for each sample in the 400–4000 cm^{-1} range, and the average spectra were used.
Double bond conversion rate of the cured samples was calculated according to Eq. (2.1) [79]:

$$DBC\% = \left(1 - \frac{A_t / A_{ra}}{A_0 / A_{rb}}\right) \times 100\ \%, \tag{2.1}$$

where A_0 and A_t are the absorption intensities of the C=C bond (at 810 cm^{-1}) before and after polymerization and A_{rb} and A_{ra} are the absorption intensities of the ester C=O bond (at 1722 cm^{-1}) before and after polymerization.

Theoretical spectra for filler-matrix interaction analysis were calculated using Eq. (2.2):

$$A_{Xf} = X \times A_f + (1 - X) A_{pol}, \tag{2.2}$$

where A_f and A_{pol} are the absorbances % for components in the composition spectra, lignocellulose component (f), and polymer matrix (pol), respectively, X = wt% of a lignocellulose component in a specific composition.

Sol-fraction measurements

Curing efficiency was evaluated by sol-fraction measurements performed for 10 parallel samples using a manual Soxhlet extraction setup with acetone as the solvent. The extraction was conducted for 72 h. Samples were weighed before and after wrapping in filter paper and then again after Soxhlet extraction before and after unwrapping.

Thermogravimetric analysis

Thermal stability was evaluated with a Mettler TG50 instrument (Greifensee, Switzerland) on 10 mg samples at a temperature range of 25–750 °C, with a heating rate of 10 °C/min, under an inert atmosphere (N$_2$) with an 80 mL/min flow rate.

Hydrostatic density testing

The densities of prepared cured samples were determined by hydrostatic weighing. Samples were weighed using Sartorius MC-1 (Sartorius, Germany) analytical balance with a density measurement kit. For each sample, 10 parallel sample measurements were performed. Each sample was weighed twice, first in air and then in ethanol. Equation (2.3) was then used to determine the density of each composite:

$$\rho = \frac{W_a \times (\rho_{etanols} - 0.0012)}{0.99983 \times (W_a - W_{etanols})} + 0.0012, \tag{2.3}$$

where W_a and $W_{ethanol}$ are the sample weight in air and ethanol, respectively, and $\rho_{ethanol}$ is the experimentally determined density of ethanol.

Calculated theoretical density ρ_t and the apparent polymer density ρ_{poly}^a were calculated by Eqs. (2.4) and (2.5) [80]:

$$\rho_t = \rho_{cel} \times \varphi_{cel} + \rho_{pol} \times (1 - \varphi_{cel}), \tag{2.4}$$

$$\rho_{pol}^a = \frac{\rho - \rho_{cel} \times \varphi_{cel}}{1 - \varphi_{cel}}, \tag{2.5}$$

where ρ is the experimental density of the printed samples; ρ_{cel} is the nanocellulose absolute density (1.6 g/cm^3) [81]; ρ_{poly} is the 0% experimental density (1.1167 g/cm^3); and φ_{cel} is the cellulose volume percent.

Dynamic mechanical analysis

Thermomechanical analysis was performed with a dynamic mechanical analyser Mettler DMA/SDTA861e (Mettler Toledo, USA) and storage modulus, loss modulus, and loss factor as a function of temperature were recorded.

Thin film samples with dimensions of 8.5 mm × 4 mm × 0.3 mm were tested in attention mode with a 1 Hz frequency, a force of 10 N, and an elongation of 10 μm, in the temperature range from –70 to 100 °C and at a heating rate of 3 °C/min.

3D printed samples were tested at a dual cantilever deformation mode with a heating rate of 3 °C min^{-1}, the applied force of 10 N, displacement of 20 μm, and at a frequency of 1 Hz from –70 to 100 °C. DMA samples were printed in a rectangular form, as per ISO-178 (80 mm × 10 mm × 4 mm). All samples, before the test, were stored in sealed plastic bags in a dark place, and the tests were performed after 2 days from the moment the samples were printed.

The molecular weight between the crosslinks (M_c) and crosslinking density (N) were calculated according to the theory of entropic rubber elasticity using Eqs. (2.6) and (2.7) [82, 83]:

$$M_c = \frac{3\rho RT}{E'}, \tag{2.6}$$

$$N = \frac{\rho}{M_c}, \tag{2.7}$$

where ρ is the density of the composite, R is the gas constant, E' is the storage modulus at 95 °C, and T is the temperature at which E' is obtained.

The adhesion parameter A was calculated from tanδ at 20 °C via Eq. (2.8) [84].

$$A = \frac{1}{1-V_f} \frac{\tan \delta_{composite}}{\tan \delta_{matrica}} - 1. \tag{2.8}$$

To calculate the filler-matrix stress efficiency transfer parameter (C^*), Eq. (2.9) was used [50]:

$$C^* = \frac{\left(E'_g / E'_v\right)_{composite}}{\left(E'_g / E'_v\right)_{matrica}}, \tag{2.9}$$

where E'_g and E'_v are glassy and rubbery storage modulus values measured at –45 °C and 95 °C, respectively.

For reinforcement parameter r calculations, Eq. (2.10) was used:

$$r = \frac{E'_c}{E'_m V_f} - \frac{1}{V_f}, \tag{2.10}$$

where E'_c and E'_m are storage modulus values at 95 °C for the composite and polymer matrix, respectively, and V_f is the nanofiller volume fraction in the composite.

Scanning electron microscopy

Thin film surface morphology was evaluated by using the Tescan Vega II instrument (Brno, Czech Republic) with a magnification of 1000× and an accelerating voltage of 5 kV. Before the analyses, the samples were coated with gold.

The 3D printed sample fracture surface was investigated with field emission scanning electron microscopy using a Nova NanoSEM 650 (FEI, USA) operated at an accelerating voltage of 3 kV. The sample fracture surfaces were obtained following freezing in liquid nitrogen.

Contact angle measurements

Contact angle measurements with sessile droplet distilled water (Crystal 10, Adrona, Latvia) were performed on Theta Lite optical tensiometer (Attention, China) to evaluate the functionalization effect on the hydrophobicity of the nanocellulose fillers and thin film composite surface.

For functionalised filler sample preparation, fillers were suspended in analysis-grade acetone, sonicated in an ultrasonic bath for 10 min, applied dropwise and then dried on a glass substrate (3 layers).

For thin film sample preparation, the film surface was chemically etched with analytical-grade acetone to remove the sticky surface with unreacted resin and then left to dry.

All measurements were performed at room temperature on dried filler films; data were recorded after 10 s of contact.

Optical microscopy

3D printing accuracy was evaluated by optical microscopy using Leica 301-371.011 DMRBE (Leica Microsystems, Germany) equipped with 5× and 20× objective lenses and the Leica application suite software. The images of 3D printing object surfaces and fracture surfaces of the 3D printed composites were obtained. The sample fracture surfaces were obtained following freezing in liquid nitrogen.

UV-Vis spectroscopy analysis

Optical property changes were evaluated by a SolidSpec3700 UV-VIS-NIR Shimadzu (Kyoto, Japan) spectrophotometer with a 60 mm diameter integration sphere and a wavelength precision of 0.5 nm in the wavelength range of 240–700 nm. Tests were performed on 200–250 μm thin films in transmittance mode and 3D printed samples with a width of 3 mm in transmittance and reflectance modes.

Spectrophotometry analysis

The prepared composition samples' changes regarding to the used reinforcement and yellowing index (YI) were evaluated using the Ci7600 Sphere Benchtop Spectrophotometer (x-rite Pantone, Michigan, USA). Three parallel measurements were performed with a total transmittance aperture of 6 mm, a wavelength range of 360–750 nm, a photometric resolution of 0.01 %, and white paper as a background due to the transparency of the 3D printed samples.

Tensile testing

The mechanical performance of the 3D printed samples was evaluated by a tensile test using a 25ST universal testing machine (Tinius Olsen, United Kingdom) according to EN ISO 527-1BA. Testing speeds were 5 mm/min for stress and strain values and 1 mm/min for modulus values. The average values of elongation at break, elastic modulus, and tensile strength were obtained from parallel 5 samples. The area under the stress-strain curves was integrated to enable the calculation of composite toughness. Before testing, all samples were stored in sealed plastic bags in a dark place; tests were performed 2 days after the printing of the samples.

Flexural testing

Three-point flexural tests were performed on 3D printed rectangular samples with dimensions of $(80 \times 10 \times 4)$ mm^3, according to the EN ISO-178 standard. A Tinius Olsen 25ST universal testing machine (USA) was used, with testing speeds of 1 mm/min for flexural modulus and 5 mm/min for flexural strength, with a 25 kN S-type load cell. The prepared specimens were stored in a sealed bag at room temperature in a dark place. Average flexural strain at break, flexural modulus and flexural strength values were obtained from the testing of 5 parallel specimens. All flexural tests were performed two days after the printing of the specimens.

QUV accelerated weathering

A weathering test with a QUV accelerated weathering tester (Q-Panel Co., USA) equipped with fluorescent UVA-340 lamps (Q-Lab Co., USA) was performed to simulate outdoor conditions in accordance with the ISO 4892–3:2016 standard "Plastics-Methods of Exposure to Laboratory Light Source, Part 3: Fluorescent UV Lamp". The test combines 3 cycles (12 h): ultraviolet sunlight (8 h) at black panel temperature 50 °C ± 3 °C and irradiance 0.75 W/m^2, spray (15 min), and condensation (3 h and 45 min at 50 °C). Each cycle of exposure occurs separately to simulate natural weathering conditions. The fluorescent UVA-340 lamps have a 295–365 nm (maximum at 340 nm) wavelength spectrum. UV light is responsible for most of the sunlight damage to polymer materials exposed outdoors [65, 69]. In the condensation cycle, the water reservoir (bottom of the test chamber) is heated to produce vapor, reaching 100 % relative humidity and forming the dew on the surface responsible for most of the wetness outdoors. The water vapor continuously condensates on the test panels (which are kept at a

lower temperature by room air flowing over the back surfaces of the specimens). Post-processed 3D printed samples were inserted into the QUV weathering chamber, removed, and tested after 0 h, 250 h, 500 h, 750 h, and 1000 h weathering exposures.

3. RESULTS AND DISCUSSION

3.1. Vegetable oil-based photocurable resins for films and additive manufacturing

3.1.1. Neat resin formulation: photoinitiator concentration selection

*Sample abbreviation: AESO-1, AESO-3, AESO-5, AESO-7 – AESO resins with 1 wt%, 3 wt%, 5 wt%, and 7 wt% photoinitiator, respectively; M-AESO-1, M-AESO-3, M-AESO-5, M-AESO-7 – AESO resins with comonomers (30 wt% HDDA and 5 wt% TMPTA) and 1 wt%, 3 wt%, 5 wt%, and 7 wt% photoinitiator, respectively.

3.1.1.1. Investigation of UV-crosslinking process

The occurrence of the crosslinking was followed by Fourier-transform infrared spectroscopy (FTIR) analyses for all formulations (neat AESO and M-AESO). In Figure 3.1, the spectra of AESO-3 and M-AESO-3 are given as examples.
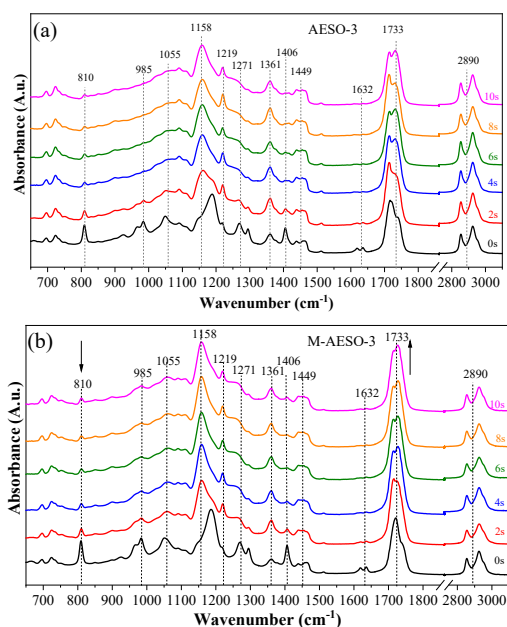
Fig. 3.1. FTIR spectra of AESO-3 (a) and M-AESO-3 (b) resins before and after UV-curing at different exposure times.

Figure 3.2 depicts the variation of *DBC%* (calculated using Eq. (2.1)) with curing time at different TPO loading. The obtained curves confirm that the addition of polyfunctional comonomers increases the conversion degree by means of about 10 %, as the values of *DBC%* obtained for M-AESO are higher than those obtained for neat AESO. *DBC%* for neat AESO reaches around 77 % in 4 s in the case of 5 % TPO loading, while it was slightly below for the

other loading of TPO. After 4 s irradiation time, the DBC% remains constant or drops. In the case of M-AESO, the *DBC*% increases sharply after only 2 s of UV irradiation and then continues to slowly increase after 4 s of UV irradiation, reaching 83 % conversion after 8 s.
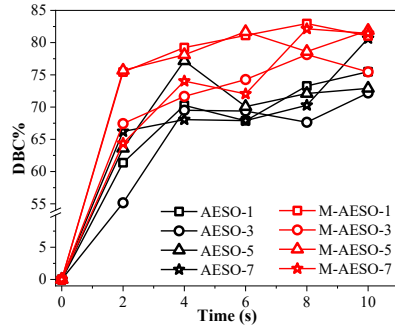

Fig. 3.2. Double bond conversion (*DBC*%) rate as a function of the UV-curing time for neat AESO and M-AESO with different loading of the photoinitiator.

Table 3.1 gathers the calculated values of crosslinking density (*N*) and the related molecular weight between crosslinks (*M*c) for all fully UV-cured resins. The results show that in the case of the studied formulations, the UV-cured resins containing the functional monomers display almost 5-fold enhanced crosslinking density characteristics in comparison to the crosslinked neat AESO resin. For example, M-AESO-3 resin formulation exhibits $M_c = 45$ g/mol and $N = 73.9 \times 10^3$ mol/cc in comparison to cured AESO-3 resin, which has only M_c of 193 g/mol and N of 16.4×10^3 mol/cc, respectively.

Table 3.1

Crosslinking Density (*N*, mol/cc) and Molecular Weight (*M*c, g/mol) Obtained for Different Formulations Cured at 4 s

Sample	M_c, g/mol	$N, \times 10^3$, mol/cc
AESO-1	130	24.6
AESO-3	193	16.4
AESO-5	223	14.4
AESO-7	149	21.5
M-AESO-1	45	73.9
M-AESO-3	45	73.9
M-AESO-5	73	46.2
M-AESO-7	269	12.3

3.1.1.2. Thermomechanical investigation of UV-cured materials

Figures 3.3 (a) and (b) show the weight losses of the samples during the heating and the first derivative curve (DTG) T_{max} (temperature of maximum degradation rate), respectively. Both resins AESO and M-AESO exhibit closely similar degradation behaviors. Yet, the results show

that the addition of the functional monomers in the case of M-AESO has increased the thermal stability by about 17–30 °C for each formulation having the same concentration of PI. Indeed, the main degradation temperature ranges from 387 °C to 400 °C for neat AESO, while it was around 420 °C for M-AESO. Moreover, the presence of the monomer induced a second degradation of the samples at around 460 °C. Overall, there is no significant weight loss until 250 °C (the first 1 % weight loss was detected at 249 °C for sample M-AESO-1), and even at this temperature, the loss is very limited, as it represents only 1–2 %. The main degradation takes place in the range of 300–500 °C. The char yields are 3–5 %.
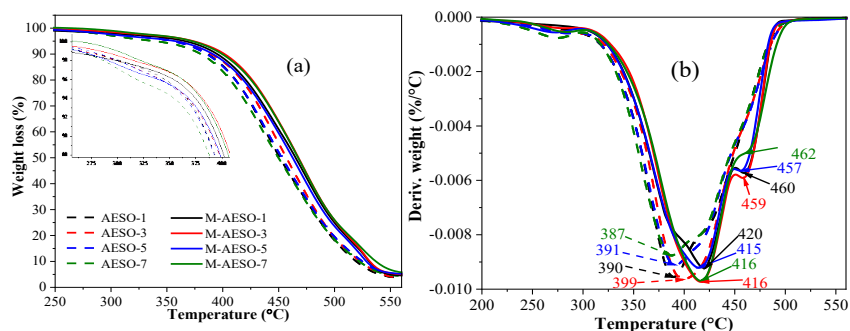
Fig. 3.3. TGA thermograms (a) and the corresponding first derivatives (b) of AESO and M-AESO resin formulations cured at 4 s.

Figure 3.4 depicts the obtained dynamic mechanical analysis (DMA) curves for neat AESO and M-AESO resin formulations loaded with different PI concentrations and UV-cured at 4 s. In the case of neat AESO resins, the storage modulus and loss moduli values are similar at the glassy state regardless of the concentration of the PI and, thus, the crosslinking density. The glass transition, in this case, occurs in a very narrow temperature window ranging between 24 °C and 29 °C, and the profiles show only one well-defined peak for each formulation. The sample with 5 wt% initiator stands out with the best values of the storage modulus in the viscoelastic state and the highest T_g, and a relatively small difference was obtained for the sample with 1 wt% of added PI. The sample with 1 wt% PI shows the highest loss modulus peak values and thus indicates a less stiff response. The M-AESO-3 exhibits the highest loss modulus value, while the formulation M-AESO-7 has the lowest loss modulus. The storage modulus values are strongly enhanced with the addition of the functional monomers by means of a 4-fold and 5-fold increase at room temperature and higher temperatures (80 °C), respectively.

The glass transition occurs at higher temperatures compared to formulations without additives, attesting to a more rigid structure, hence increased crosslinking density. T_g values were 19–34 °C higher compared to those achieved for neat AESO samples. The damping factor (tanδ) peaks of all formulations were broader than those obtained for neat AESO resins, exhibiting a shoulder for which the intensity increases with the decrease of the PI loading.
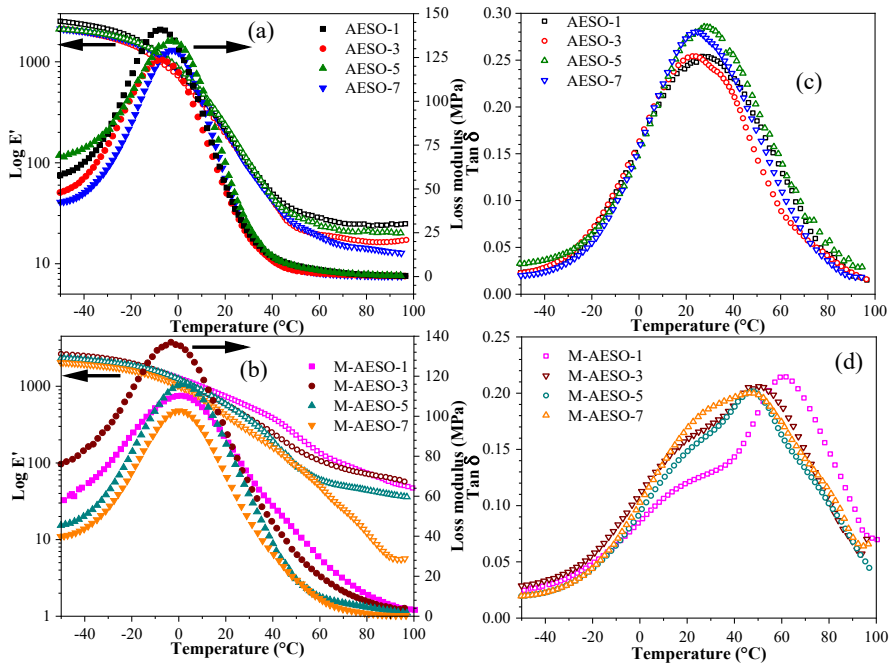
Fig. 3.4. DMA curves for formulations cured at 4 s: (a) storage and loss modulus of AESO resins; (b) tanδ of AESO resins; (c) storage and loss modulus of M-AESO resins; and (d) tanδ of M-AESO resins.

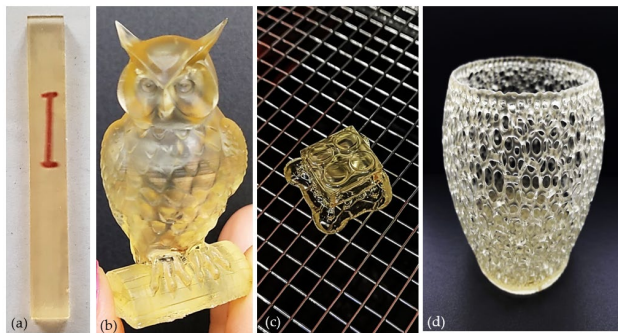### 3.1.1.3. Printability of the materials

Fig. 3.5. Printed M-AESO-3 resin: transparent bar (a), owl (b), Lego cube (c), and basket-like bowl (d).

After the optimization of the formulations and their UV-curing, the formulated resins were validated as UV-sensitive. Objects with more or less complex structures were then printed from all M-AESO formulations using SLA printers (Fig. 3.5). These printed objects demonstrate complete layer fusion and accurate printing quality, as they were defect-free and exhibited high-

resolution features and good mechanical properties, ensuring good stability without undergoing any shrinkage over time.

3.1.1.4. Summary

Acrylated epoxidized soybean oil was used alone or in combination with reactive diluents as the main component to formulate UV-curable resins. The effect of the photoinitiator and UV-light exposure time were studied to understand the curability of these vegetable oil-based formulations. The addition of the reactive diluents induced an increase in the double bond conversion rate ($DBC\%$) by 10 %. Thermal degradation analysis showed good thermal stability of both types of formulations, improved by the reactive diluents reaching about 420 °C. The mechanical properties of the cured resins improved with the crosslinking density. Similarly, these properties were also improved with the addition of the reactive diluents. The storage modulus improved by almost 4-fold at room temperature and 5-fold at 80 °C, reaching 726 MPa and 72 MPa, respectively, for the formulations containing the reactive diluents (AESO-M compositions). Accordingly, the formulated bio-based resins containing the reactive diluents were deemed suitable for UV-assisted 3D printing, and thus they were successfully validated by printing different objects with complex structures with SLA printers. The formulated bio-based resins provided excellent printability showing a high promise for scalability toward commercial applications, yet further development and optimization are still needed.

M-AESO-3 was chosen for further investigations of UV-curable resins for films and 3D printing. The decision was based on the optimal properties of viscosity, crosslinking density, and thermomechanical properties that were not further improved with increasing PI concentration.

3.2 Lignocellulose filler-loaded resins for films

3.2.1. Single lignocellulose filler-loaded resins

* Sample abbreviation: VO – vegetable oil-based composition without fillers; vegetable oil-based composition with lignocellulose components 5–30 wt% summarized in Table 3.2.

Table 3.2

Sample Abbreviation

Filler	Sample abbreviation regarding filler loading, wt%				
	0	5	10	20	30
None	VO	-	-	-	-
Nanocrystalline cellulose	-	VOC5	VOC10	VOC20	VOC30
Nanofibrillated cellulose	-	VOF5	VOF10	VOF20	VOF30
Hemicellulose	-	VOH5	VOH10	-	-
Lignin	-	VOL5	VOL10	-	-

3.2.1.1. Macromolecular chain network structure

The density, *DBC*%, molecular weight between crosslinks (M_c), and the crosslinking density (*N*) for 10 wt% compositions are summarized in Table 3.3. Lignocellulosic component addition causes a slight density increase, as seen in Table 3.3. The increase is related to the absolute density of C and F (1.6 g/cm³) [56], H (1.5 g/cm³) [85], and L (1.4 g/cm³) [85], which are higher than the experimentally determined VO density (1.1 g/cm³). Theoretically calculated densities for VOC10, VOF10, and VOH10 compositions are 1.2 g/cm³ and 1.1 g/cm³ for VOL10. Theoretical and experimental densities overlap in the error range, so it can be concluded that no significant voids are present. The 5 wt% compositions have similar observations.

The data in Table 3.3 shows that 10 wt% composition sol-fractions decrease by –0.51 % for VOC10 and increase by +3.1 % and +1.08 % for VOF10 and VOH10, respectively. VOC10 sol-fraction decrease indicates greater crosslinking than VO composition. The sol-fraction increase for the VOF10 and VOH10 compositions. VOL10 has a much more pronounced increase in the sol-fraction (+15.9 %). A similar trend for data (with sol-fraction changes of –0.31 % for VOC5, –1.5 % for VOF5 and VOH5, and +3.28 % for VOL5 compositions) can be observed in Table 3.3.

M_c has significantly decreased for C, F, and H compositions with 5 wt% and 10 wt% loadings, while it has increased for L compositions (Table 3.3). The decrease is explained by filler-matrix interaction, and the increase is due to the significantly higher sol-fraction. Accordingly, *N* increased for VOC10, VOF10, and VOH10 and decreased (–1.2-fold) for VOL10 composition. The highest increase of *N* was recorded for VOC10 composition (3.2-fold), indicating the most significant filler-matrix interaction. This is followed by a 2.3-fold and a 2-fold increase for VOH10 and VOF10 compositions, respectively. The same tendency is

observed for 5 wt% compositions in Table 3.3 (1.6, 1.3, 2.3, and –1.4-fold increase/decrease for VOC5, VOF5, VOH5, and VOL5, respectively).

Table 3.3

Structural Characteristics of the VO, 5 wt% and Lignocellulose Compositions

Sample	Density, g/cm^3	Sol-fraction, %	$DBC\%_{max}$	M_c, g/mol	$N, \times 10^3$, mol/cm^3	Transmittance at 500 nm, %
VO	1.1197 ± 0.005	2.5	78	161	6.9	96
VOC5	1.1394 ± 0.003	2.2	80	100	11.4	90
VOC10	1.1583 ± 0.015	2.0	80	50	23.3	80
VOF5	1.1299 ± 0.003	1.0	68	127	8.9	83
VOF10	1.1339 ± 0.005	5.6	70	80	14.2	71
VOH5	1.1097 ± 0.010	1.0	75	69	16.2	91
VOH10	1.1457 ± 0.004	3.6	75	71	16.2	82
VOl5	1.1139 ± 0.000	5.7	55	225	5.0	86
VOL10	1.1347 ± 0.014	18.4	24	189	6.0	78

3.2.1.2. Morphological properties
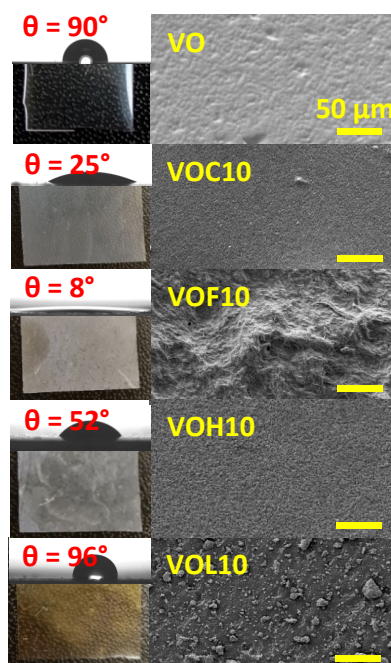
Fig. 3.6. The prepared VO and 10 wt% compositions, SEM micrographs of the composite surface structure with 1000× magnification, and water wetting (θ).

The obtained cured compositions are shown in Fig. 3.6. The VO composition is highly optically transparent, while the VOC10, VOF10, and VOH10 compositions are translucent with white coloring. In contrast, the VOL10 composition is brown. Translucence is confirmed by UV-Vis measurements (Table 3.3), where VO shows the highest transmittance of 96 % at 500 nm, followed by VOH10, VOC10, VOL10, and VOF10 compositions with 82 %, 80 %, 78 %, and 71 % transmittance, respectively. Wetting of the composition surfaces can be observed in Fig. 3.7, where H_2O droplet contact angles (θ) are displayed. In Fig. 3.6, SEM magnification of 1000× shows that the VO composition has a relatively smooth surface structure. VOC10 composition shows exceptionally homogeneous dispersion at the same magnification, resulting in a nanostructured surface with $\theta = 25°$. Only a few agglomerates were detected, demonstrating that the modified vegetable oil-based polymer matrix has excellent interaction and adhesion with C. While the VOF10 composition surface shows a much rougher surface structure than the VOC10 composition, it also shows the lowest $\theta = 8°$. The contact angle of the VOH10 composition with a water droplet is 52°, which is reduced compared to VO. At the same time, the VOL10 composition shows surface-wide particle distribution (2017 ± 736 nm), but a nanostructure pattern has not developed. The contact angle is nearly identical to the VO composition (96° and 90°, respectively).

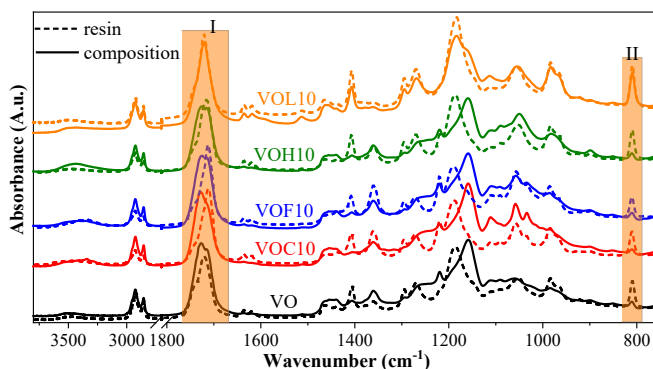### 3.2.1.3. Fourier-transform infrared spectroscopy

Fig. 3.7. FTIR spectra of resins and cured VO and 10 wt% compositions. The curing time was 10 s.

Resins, cured compositions, and lignocellulosic components were characterized with FTIR spectroscopy (VO, 10 wt% compositions in Fig. 3.7). Spectra in Fig. 3.7 show no new absorption peaks, absent in VO and lignocellulosic component spectra. Therefore, it is concluded that no new covalent bonds between the polymer matrix and lignocellulosic components are formed.

Calculated $DBC\%$, representing the covalent bond crosslinking degree, is shown in Fig. 3.8 for VO and 10 wt% samples. The curing trends for all prepared resins are similar. The primary curing occurs in the first 4 s, while the maximum $DBC\%$ was achieved at the 4 s mark. The

Flory–Rehner calculations and $DBC\%_{max}$ are represented in Table 3.3. Crosslinking evaluated by $DBC\%$ corresponds to sol-fraction data. The addition of nanocellulose has resulted in observable inverted changes in sol-fraction and $DBC\%$ data for C and F compositions. Hence, compared to VO, a rise of $DBC\%$ for C compositions (+2 % for both VOC5 and VOC10) and a decrease for F compositions (–10 % and –8 % for VOF5 and VOF10, respectively) LN compositions have a much more significant drop in $DBC\%$ values (–23 % and –54 % for VOL5 and VOL10, respectively). An exception is H compositions with the second polymer phase, creating a slight decrease in $DBC\%$ values (–3 % for both 5 and 10 wt% compositions). Similar tendencies are observed for 5 wt% compositions, with the lowest $DBC\%$ for VOL5 (55 %).
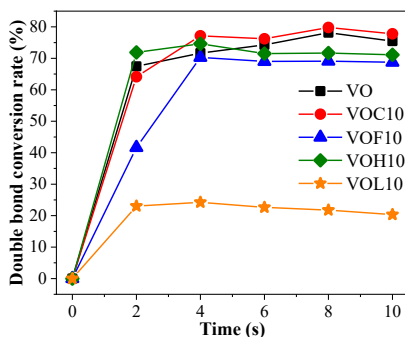
Fig. 3.8. Double bond conversion rate % ($DBC\%$) for VO and 10 wt% compositions.

Theoretical spectra according to Eq. (2.2) (dashed lines) with increased and reduced peak intensities for C=O groups for 10 wt% samples are shown in Fig. 3.9. Experimental spectra do not overlap with theoretical spectra and show significant differences. VOC10 seems to have the most substantial interaction with the triglyceride's carbonyl group but is limited with an acrylate carbonyl group. VOF10 has modified peak intensities for both carbonyl groups in comparison to VOC10 due to interactions of triglyceride and acrylate carbonyl groups, respectively. VOH10 only interacts with the acrylate carbonyl group (for the triglyceride carbonyl group, theoretical and experimental spectra overlap). Due to the reduced $DBC\%$, the VOL10 resin interaction with LN dominates over the cured compositions' interaction. They showed high interaction with the acrylic carbonyl group, which are more mobile than reacted counterparts (after crosslinking).
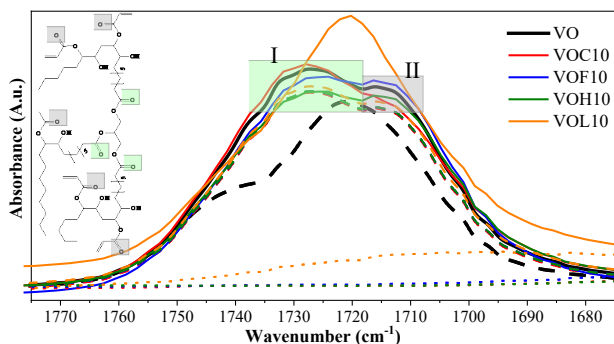
Fig. 3.9. FTIR spectra of the C=O group for VO resin (black dashed line) and cured composition (solid black line), 10 wt% cured compositions (dashed lines – theoretical spectra obtained with Lambert-Beer's equation and solid lines – experimental spectra), and lignocellulosic component (dotted lines).
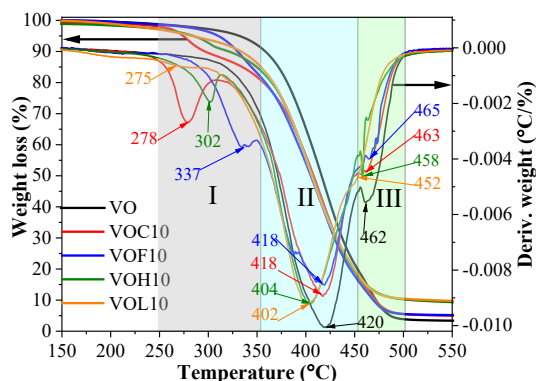
3.2.1.4. Thermal stability

Fig. 3.10. Thermal stability of the VO and 10 wt% compositions (weight loss and derivative weight).

In Fig. 3.10, the efficient derivative weight loss is estimated in the II-blue and III-green sectors, respectively. While T_{max1} (I-grey sector) peaks are present only for loaded compositions, they account for lignocellulosic components close to the composition surface. Thermal destruction of used lignocellulosic components showed T_{max1} 174 °C, 312 °C, 273 °C, and 328 °C for C, F, H, and LN, respectively. T_{max1} values (increased by 104 °C, 25 °C, and 29 °C in comparison to filler T_{max1}) for 10 wt% compositions show that the matrix protects the lignocellulose component in VOC10, VOF10, and VOH10 compositions, respectively. Extreme protection (increase by 104 °C) for C in composition VOC10 confirms better filler-matrix interaction suggested in FTIR analysis. While T_{max1} for VOL10 has been lowered by 52 °C in comparison to LN, no significant mass loss can be observed in Fig. 3.10. T_{max2} accounts for the main AESO matrix degradation. Adding lignocellulose components has not significantly affected the material's thermal stability; the biggest decrease from VO in T_{max2} is 18 °C for

VOL10 composition. The lowest decrease of T_{max2} (2 °C) shows for VOC10 and VOF10 compositions. VOH10 has a narrowed T_{max3} due to the H polymer nature confirmed by SEM, which dilutes the acrylate polymer matrix [36]. All samples showed similar char yields of 3–9 wt%, with the highest for VOH10 and VOL10.

3.2.1.5. Thermomechanical properties

VOC10 shows superior performance compared to the VOF10 composition by achieving up to a 3.5-fold increase in storage modulus values, compared to only a 2-fold improvement achieved with F filler over the VO (Fig. 3.11 (a)). In the case of VOH10, there is a very high increase in the storage modulus, showing a 3.5-fold improvement compared to VO. For LN composition VOL10, there is a drop in properties compared to VO. The loss modulus (Fig. 3.11 (b)) shows that even at –40 °C, the compositions have relatively high viscous responses. The significant enhancement of loss modulus values is visible for VOC10 and VOH10. This is also visible above 30 °C, and VOC10 and VOH10 retain significantly higher values, indicating that these compositions have strong interactions with the VO matrix. Both VOC10 and VOH10 achieved a 3.5-fold improvement following a glassy to a viscoelastic state transition.
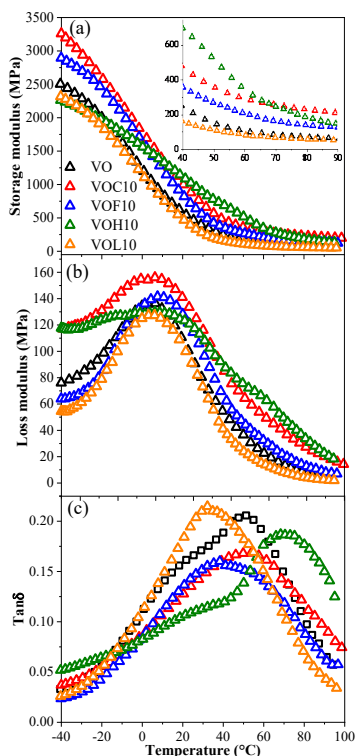

Fig. 3.11. Storage modulus (a), loss modulus (b), and loss factor tanδ (c) curves of the VO and 10 wt% compositions.

In tanδ curves (Fig. 3.11 (c)), peak splitting can be seen for some of the compositions. An interesting observation can be made that compositions with fillers formed more uniform tanδ peaks, while blends with H made the shoulder part more pronounced. With peak deconvolution, two glass transition peaks were obtained for some compositions, and the obtained values can be seen in Table 3.4. VOL10 has a single glass transition peak that is 19 °C lower than the main peak of VO. VOH10 showed the opposite effect to VOL10 and shifted peaks to higher temperatures. The first peak (shoulder part) has a significantly lower tanδ value, but most notable was that the main peak was shifted by 22 °C to a higher temperature when compared to VO. This is assumed to be achieved by hydrogen bonding. The decrease in tanδ values matches well with the increase in storage modulus values and indicates a more rigid response of VOH10 compared to VO. In contrast, VOC10 and VOF10 remained similar to the initial VO curve, but their peaks were narrower and shifted by approximately 10 °C to a higher temperature.

Table 3.4

T_g from tanδ of the VO and 10 wt% Compositions

	T_{g1}, °C	T_{g2}, °C
VO	9	52
VOC10	9	51
VOF10	41	-
VOH10	23	74
VOL10	33	-

3.2.1.7. Summary

The present study investigates lignocellulose components' (nanocrystalline cellulose (C), nanofibrillated cellulose (F), hemicellulose (H), and lignin (L)) effects on vegetable oil-based UV-curable resin performance. 5 wt% and 10 wt% loads of the lignocellulosic components were introduced in vegetable oil-based resin (VO), emphasizing the 10 wt% compositions (VOC10, VOF10, VOH10, and VOL10 for C, F, H, and L, respectively). Transparency measurements showed a 14.6 %, 16.7 %, 18.8 %, and 26.0 % decrease in transparency for 10 wt% H, C, LN, and F compositions, respectively. Structural analysis showed a slight increase in density for all the compositions, an increase by 2 % in curing efficiency (DBC%) for C 10 wt% composition, and a decrease by 3 %, 8 %, and 54 % for H, F, and L 10 wt% compositions, respectively. Thermomechanical analysis shows no changes in glass transition temperature for 10 wt% C composition, a decrease for F (11 °C) and LN (19 °C), and an increase for H (14 °C and 22 °C) composition, indicating lignocellulosic components' interaction with the matrix. Thermal stability investigations revealed a 0.5 % drop in stability for 10 wt% C and F compositions and a 3.8 % and 4.3 % drop for H and L compositions. Char yield increased by 2 % for C and F compositions and 6 % for H and L compositions. The application of Lambert–Beer's law revealed strong interaction with the polymer matrix for C, F, and H components. C shows the strongest interaction with the matrix triglyceride's carbonyl group, F shows similar interaction with both carbonyl groups (triglycerides and acrylates), and H prefers to interact

with the acrylate carbonyl groups. Meanwhile, the L composition appears to interact more in the resin form than in the cured composition, owing to the lower *DBC%*.

However, until now, H and L in their unmodified form have been avoided in UV-curable compositions. This work demonstrates significant results where both may bring exceptional property improvements necessary for a particular application involving hydrophobicity or 2-phase nanostructured polymer blends. Hence, it is concluded that H has excellent potential to be a bio-based, nonreactive diluent for UV-curing resins. Furthermore, since L also has value, hybrid combinations of lignocellulosic components in UV-curing resins could be interesting for future investigations. The developed photocuring resins could be applicable as different coatings on wood or other surfaces; nonetheless, further investigations are still needed. Future research should also concentrate on creating hybrid filler systems in UV-curable resins, therefore adapting nature-based systems.

3.2.2. Hybrid lignocellulose filler loaded resins

*Sample abbreviations: 10 wt% of lignocellulose filler content, where 5 wt% was constant L content and 5 wt% was the C/F/H fillers. For example, C1F1H1 composition contains 33.33 % of C, F, and H lignocellulosic components.

3.2.2.1. Morphology properties

Hybrid composition morphology was characterized by SEM imaging at 10 000× magnification, presented in Fig. 3.12. The green frame accounts for the hemicellulose (H) content decrease from top to bottom SEM image (Fig. 3.12 (a)–(b)), and the red and blue for cellulose nanocrystal (C) (Fig. 3.12 (d)–(b)–(e)) and nanofibrillated cellulose (F) (Fig. 3.12 (f)–(b)–(g)) content decrease, accordingly. The micro-sized particles seen in the images are lignin (L) particles, evidently dispersed homogeneously. The red-framed images in Fig. 3.12 show that the decreasing C content results in a rougher structure. The highest C content shows the smoothest surface, with some evident agglomerates from F and L particles. F decreases in the blue frame images, which, on the contrary, show a more homogeneous structure with fewer F agglomerates. The surface porosity increases for the C3F1H3 (Fig. 3.12 (g)), which is attributed to the H content increase (42.9 %), while the F decrease has no impact. The green-framed images show that surface porosity decreases by decreasing H. Surface morphology can be tuned by adjusting the homogeneity of the lignocellulosic component and C and H's porosity changing content, respectively.
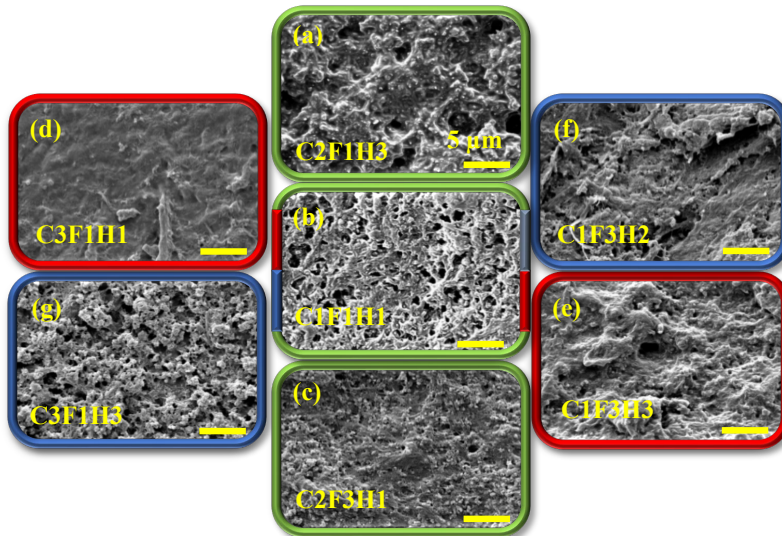

Fig. 3.12. Surface morphology SEM images at 10 000× magnification of hybrid compositions where lignocellulose component content in 5 wt% decreases from top to bottom image H↓ (C2F1H3 (a)→C1F1H1 (b)→C2F3H1 (c)), C↓ (C3F1H1 (d)→C1F1H1 (b)→C1F3H3 (e)), and F↓ (C1F3H2 (f)→C1F1H1 (b)→C3F1H3 (g)).

3.2.2.2. Macromolecular chain network

Figure 3.13 shows $DBC\%$ data over time (a); $DBC\%_{max}$ values (b), $DBC\%$ range from 62 % to 80 % for C3F3H1 and C3F2H3, respectively. All the prepared hybrid resins are completely crosslinked approximately in 8 s under UV-light. L component 5 wt% and 10 wt% loaded resins (Table 3.4) reduced $DBC\%$ values from 78 % for the neat resin to 55 % and 24 %, respectively.
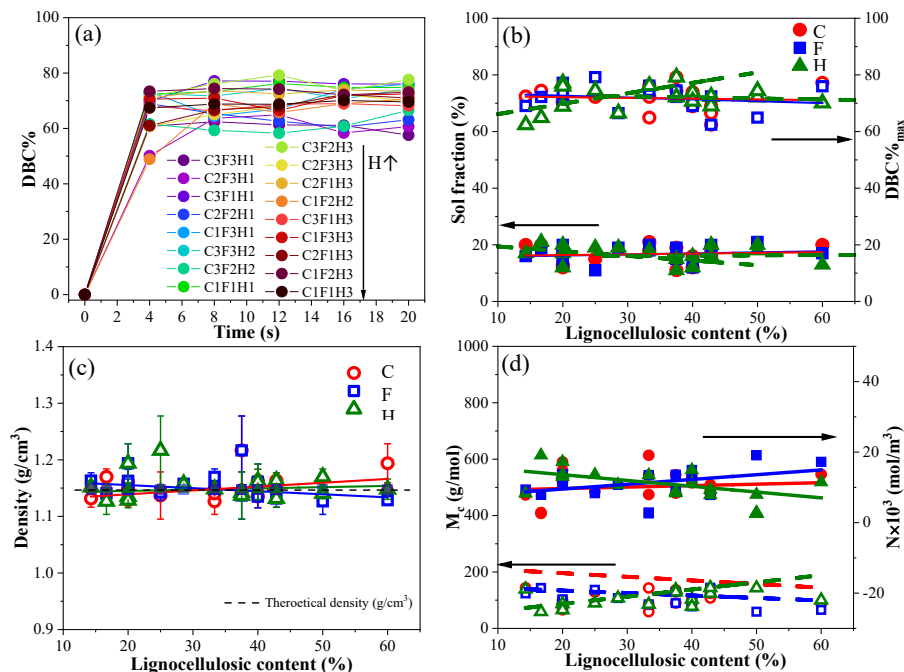

Fig. 3.13. Double bond conversion rate ($DBC\%$) vs. time (a); sol-fraction and maximum $DBC\%$ values ($DBC\%_{max}$) vs. content (b); experimental and theoretical densities (c); and crosslinking density and molecular weight between crosslinks (d) for hybrid lignocellulose nanocomposite resin photocuring.

A closer look at the impact of H content on $DBC\%_{max}$ is presented in Fig. 3.13 (b), which reveals that the optimal H content is 38 % in hybrid fillers for achieving the highest $DBC\%$ value of 80 %. Hence, it is evident that hybrid compositions help to overcome the negative effect of LN's loading on the photopolymerization process, increasing overall $DBC\%_{max}$ values from 55 % up to 80 %. Sol-fraction data in Fig. 3.13 (b) supports the $DBC\%_{max}$ findings, revealing an insignificantly increasing sol-fraction while C and F content increases, and decreases while H content is increased till 38 % and afterwards, the H content increase does not impact the sol-fraction. The sol-fraction data ranges 11–21 % for C3F2H3 and C2F3H1, respectively.

Figure 3.13 (c) reveals that experimental densities vary 1.1–1.3 g/cm^3. However, experimental densities and theoretical densities have minimal deviations. Nevertheless, it is observed that C and H increase density while F causes a decrease in density. While the density

decreases in the case of Fs. While sol-fraction matches $DBC\%_{max}$, crosslinking density N and molecular weight between crosslinks M_c, presented in Fig. 3.13 (d), correspond to the experimental density data. Increasing N and decreasing M_c for samples C and H are shown in Fig. 3.13 (d), while F content increases M_c. Compared to the VO matrix properties (Table 3.4), N for hybrid compositions has increased by 12 mol/cm^3 and M_c has decreased by102 mol/cm^3. However, the highest $N = 23.3$ mol/cm^3 was achieved for the C 10 wt% composition; while the highest $N = 9.1$ mol/cm^3 was achieved for hybrid composition C2F3H1, which is still 4.1-fold higher than for the 5 wt% L sample.

3.2.2.3. Thermomechanical properties

Figure 3.14 (a) shows that all hybrid compositions at low temperatures have enhanced storage modulus values in comparison to the 5 wt% L. For example, the C1F3H1 sample showed $E'_{-45\,°C} = 4250$ MPa, which is a 2-fold increase compared to the 5 wt% LN sample ($E'_{-45\,°C} = 1989$ MPa). Half of the hybrid compositions show higher storage modulus values in comparison to sample 5 wt% H ($E'_{-45\,°C} = 2813$ MPa). The C1F3H1, C3F1H1, and C2F3H1 compositions' storage modulus values are higher than 10 wt% of C compositions ($E'_{-45\,°C} = 3377$ MPa). The C1F3H1 composition has 60 % and C2F3H1 has 50 % F. Hybrid compositions with a lower H content and higher C/F content significantly outperform single filler materials.
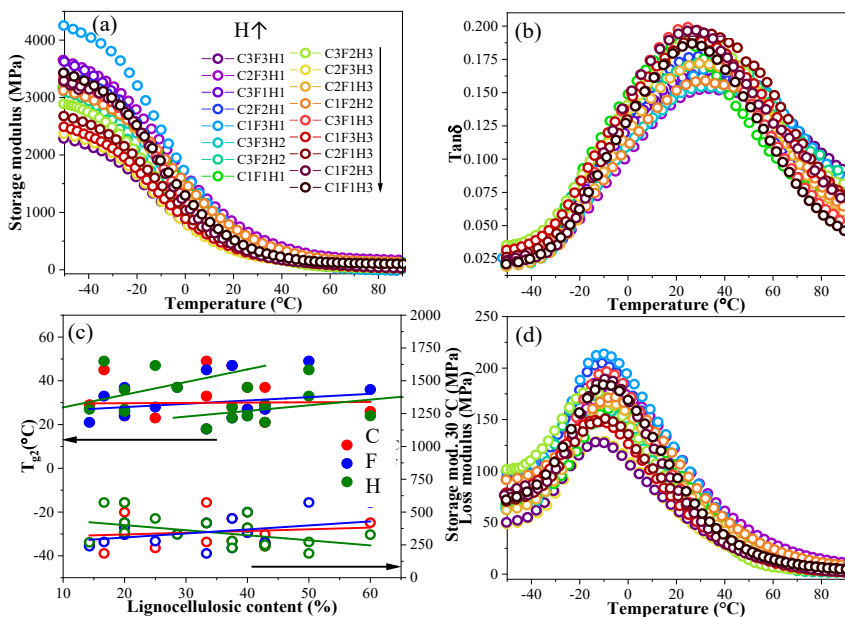

Fig. 3.14. Storage modulus (a), loss modulus (b), loss factor tanδ (c), and glass transition temperature and storage modulus at 30 °C tendencies depending on lignocellulose component content (d).

Figure 3.14 (b) shows that increasing H and decreasing C/F content leads to a drop of tanδ absolute values. These tendencies are consistent with single filler compositions. Tanδ curves

maximum can also be used to obtain glass transition temperatures. Deconvolution was performed on tanδ curves presented in Fig. 3.14 (b) to assess single filler impact, and the calculated T_g were summarized in Table 3.5. The hybrid composition values revealed three T_g, in comparison to single filler compositions that showed two. T_{g2} for the VO matrix is 52 °C and for the 5 wt% L composition – 37 °C; in turn, T_{g2} for hybrid compositions ranges 18–49 °C. Figure 3.14 (c) shows that T_{g2} increases with increasing H and F content, whereas increasing C content has no discernible effect on T_{g2}. T_{g3} is attributed to H influence because 10 wt% H increased significantly up to 74 °C.

Table 3.5

Glass Transition Temperatures from tanδ and Loss Modulus of the Hybrid Compositions

Sample	T_{g1}, °C	T_{g2}, °C	T_{g3}, °C	$T_{g, loss}$, °C
C3F3H1	−7	27	70	−12
C2F3H1	8	49	> 100	−6
C3F1H1	-	26	-	−11
C2F2H1	−8	27	87	−11
C1F3H1	−7	36	> 100	−11
C3F3H2	4	47	100	−10
C3F2H2	−7	37	> 100	−17
C1F1H1	−15	18	76	−4
C3F2H3	−11	28	> 100	−15
C2F3H3	−10	23	71	−13
C2F1H3	0	37	> 100	−8
C1F2H2	-	24	60	−5
C3F1H3	−5	21	66	−8
C1F3H3	−9	29	> 100	−14
C2F1H3	−8	33	> 100	−10
C1F2H3	12	45	> 100	−10
C1F1H3	−9	24	59	−9

Tanδ is better suited for complex resin systems and reinforced composites with strong effects [86, 87]. T_g loss presented in Fig. 3.14 (d), attributed to the matrix AESO −9 °C [79], is the closest to T_{g1} calculated from the tanδ deconvoluted peaks. Meanwhile, the loss modulus provides information on filler matrix interfacial interaction [40, 88]. Single filler compositions showed that the fillers interact with the VO matrix. Hybrid compositions show an even higher viscous response at low temperatures than the single-filler ones.

3.2.2.4. Lignocellulose filler synergy

Figure 3.15 shows two submerging FTIR absorption peaks of the C=O groups attributed to acrylate and triglyceride carbonyl group stretching vibrations at 1716 cm^{-1} and 1727 cm^{-1}, respectively [89]. Hybrid composition spectra in Fig. 3.15 show a tendency with increasing H

content (decreasing C and F content), where triglyceride shows the carbonyl group and acrylate group peaks' shifts, respectively. Hence, one could adjust the interaction between the fillers and matrix by modifying the C, F, H, and L ratios in the hybrid composite material.
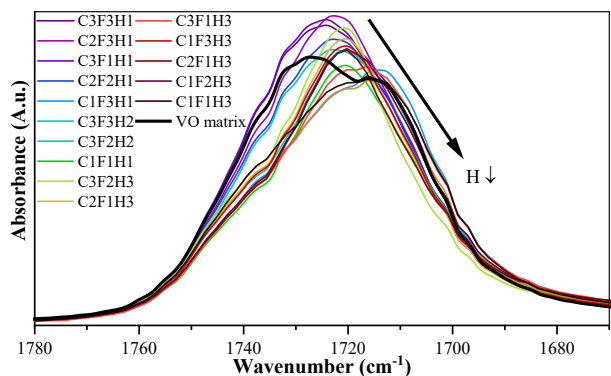

Fig. 3.15. FTIR spectra of the C=O group of hybrid compositions and VO matrix.

3.2.2.5. Thermal stability

Figure 3.16 (a) shows a five-step thermal destruction. T_{max} attributed to degradation of the AESO main matrix and added comonomers HDDA and TMPTA in sectors IV and V (of Fig. 3.16 (a) T_{max4} and T_{max5}, respectively). The 11 °C decrease of T_{max4} relates to the 5 wt% LN and H content in the hybrid compositions. Destruction sectors I, II, and III (T_{max1}, T_{max2}, and T_{max3}, respectively) are assigned to C, H, and F filler. The thermal destruction in sector VI has no significant weight loss changes. Figure 3.16 (b) shows T_{max4} at sector IV tendencies depending on the lignocellulose component content increase. The H content increase has two thermal stability tendencies: increasing, dropping, and increasing again. F shows a slightly decreasing tendency, while C shows an increase of T_{max4}. The C's increase is related to more unstable Cs burning out faster, and therefore, when the temperature reaches sector IV, thermal destruction corresponds to the matrix.
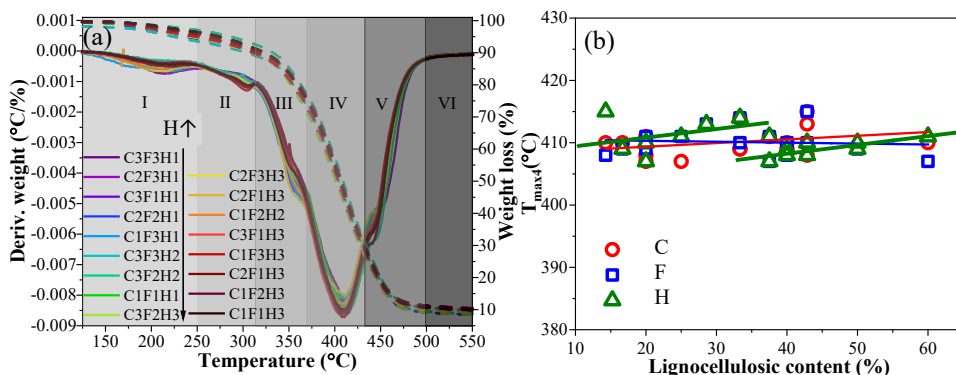

Fig. 3.16. TGA curve of the hybrid compositions (a); T_{max4} tendencies depending on lignocellulose component content (b).

3.2.2.6. Summary

The present study investigates the benefits of hybrid lignocellulose components of nanocrystalline cellulose (C), nanofibrillated cellulose (F), hemicellulose (H), and lignin (L) on the performance of vegetable oil-based (VO) UV-curable resins. 10 wt% of hybrid lignocellulose filler consisting of 5 wt% LN and 5 wt% C/F/H ratios was introduced into the VO-based matrix. Scanning electron microscopy measurements revealed that by loading more H and C, low porosity and smooth surface could be achieved. Investigations revealed optimal H content of 38 % for the highest double bond conversion rate of 80 %. Thermomechanical investigations showed three different glass transition temperatures (T_g) and up to a 4.5-fold increase in storage modulus compared to a 5 wt% L single-filler composition. T_{g1} is assigned to the main AESO matrix –9 °C, T_{g2} by the lignocellulose components around 20–35 °C and T_{g3} of interphase 70–90 °C. Tanδ curves benefit higher glass transition in H and F but do not affect T_{g2} in C. Hybrid lignocellulose fillers mitigate L's UV-light absorption properties and provide beneficial synergies.

Until now, lignocellulose fillers for UV-curing resins have been investigated only in single filler compositions; this work sheds light on the novel role of hybrid lignocellulose reinforcement. The proposed hybrid lignocellulosic composite UV-curing resins could be used as various coatings with wood structure-mimic properties; however, more research is still needed for future application.

3.3. Nanocellulose-reinforced AESO resins for stereolithography

3.3.1. Nanofibrillated cellulose-reinforced AESO resins for stereolithography

*Sample abbreviations: all resin formulations were named in accordance with the filter paper nanofibrillated cellulose (pF) loading (wt%) as follows: 0%, pF0.1%, pF0.5%, and pF1%.

3.3.1.1. Resin viscosity and printing parameters

The resin viscosity at room temperature was tested by a viscometer with rotation speeds of 1 RPM to 100 RPM, as shown in Fig. 3.17 (a). It reveals that effective viscosity absolute values strongly increase in all measured ranges correlating with higher filter paper nanofibrillated cellulose (pF) loading. The viscosity of 0% and pF1% resins at 1 RPM and 100 RPM slightly increases from 0.24 Pa×s to 1.8 Pa×s and decreases from 38.0 Pa×s to 3.8 Pa×s, respectively. The flow behavior index n is 1.09, 0.89, 0.56, and 0.52 for 0%, pF0.1%, pF0.5%, and pF1%, respectively. The pF-loaded resin compositions show $n < 1$, which indicates pseudoplastic fluid shear thinning behavior. In contrast $n > 1$ indicate share thickening shear thickening process (0% resin).
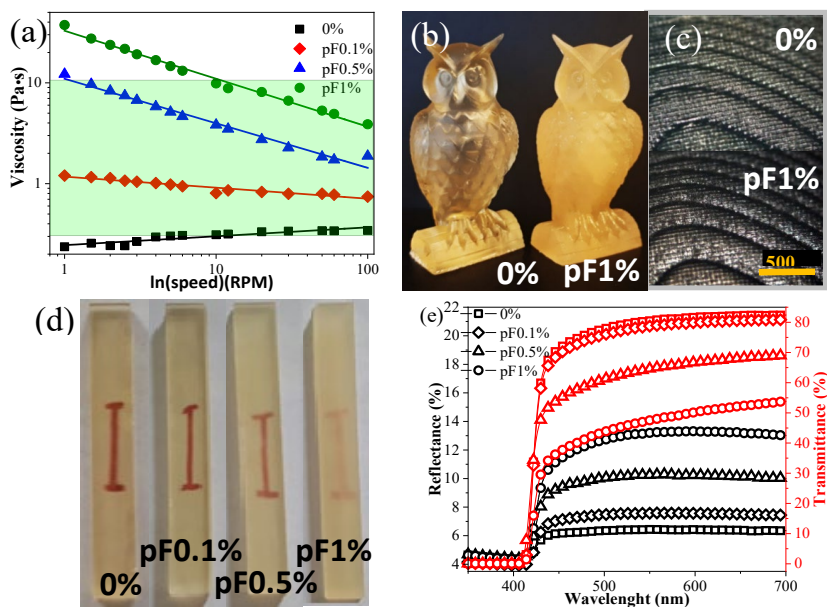

Fig. 3.17. Resin viscosity curves (a); 3D printed owls with 0% and pF1% resins (b); owl's optical microscope images at 5× magnification (c); printed bars' images (d); UV-Vis reflectance and transmittance spectra of printed resins (e).

The high printing accuracy for the owl model was obtained for 0%–pF1% resins, as shown in Fig. 3.17 (b). The closer inspection of the printed objects at 5× magnification (Fig. 3.17 (c)) by optical microscope revealed the excellent resin printing resolution. As shown in Fig. 3.17 (d), the colors and the translucence of the printed objects have been strongly affected by pF loading. The samples were placed on a sheet of paper (Fig. 3.17 (d)) on top of a red line for transparency observations, and they provided a good correlation with the UV-Vis transmittance spectroscopy measurements (Fig. 3.18 (e) – red curves).

Reflectance spectra in Fig. 3.17 (e) (black curves), show minimal reflectance below the visible light, barely reaching 5 %. Absolute values at 500 nm transmittance/reflectance for 0%, pF0.1%, pF0.5%, and pF1% samples are 78 % / 6 %, 76 % / 8 %, 61 % / 10 %, and 44 % / 13 %, respectively. The values of scattered visible light are 16 %, 16 %, 29 %, and 43 % for 0%, pF0.1%, pF0.5%, and pF1%, respectively.

3.3.1.2. Structure analysis

Figure 3.18 (a) represents the printed sample experimental density ρ, calculated theoretical density ρ_t, and the apparent polymer density ρ_{poly}^a calculated by Eqs. (2.4) and (2.5) [80].
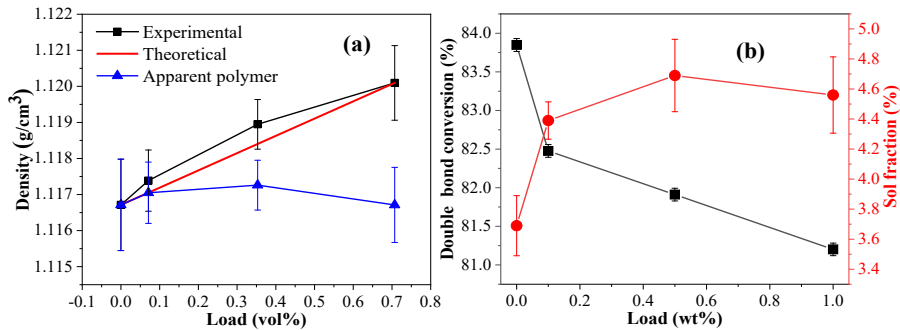

Fig. 3.18. Experimental, apparent, and theoretical polymer densities (a) and double bond conversion rate and sol-fraction (b) for prepared, printed resins.

Figure 3.18 (a) shows that the composite experimental density ρ is within the margin of error compared to ρ_t. There is a slight decrease in $DBC\%$ values with higher pF loading in the resin, while the sol-fraction increases (Fig. 3.18 (b)). The mesh crosslinking density (N) of the resins pF0.1%, pF0.5%, and pF1% has significantly increased by almost 2.4-fold, 5-fold, and 6-fold and molecular weight between crosslinks (M_c) reduced (Table 3.6).

Table 3.6

Molecular Weight Between Crosslinks and Crosslinking Density

content, wt%	content, vol%	M_c, g/mol	N, 10^3 mol/m^3
0	0.000	1024	1.1
0.1	0.070	472	2.4
0.5	0.035	219	5.2
1	0.071	196	5.8

3.3.1.3. Morphology

Figure 3.19 (a) with a 100 µm scale bar shows that surface quality decreased with increasing pF content when the printing accuracy was maintained using a constant layer thickness of 50 µm. Smooth surfaces are observed for the 0% sample, while with increasing pF content, fracture surfaces become rougher. In 10× optical microscopy images, black cracks are seen. According to the crack distribution, fibers agglomerate when the pF content exceeds 0.1 wt%, and overall homogeneity decreases as a consequence. Figure 3.19 (b) shows the SEM microscopy images; while similar fracture patterns are observed in all cases, changes in surface roughness are observed. The pF0.1% composite sample's fracture surface, while similar to that of the 0% sample, displays sharper fracture edges. Further increasing the pF content introduces a combination of smooth regions and sharp-edged fracture paths.
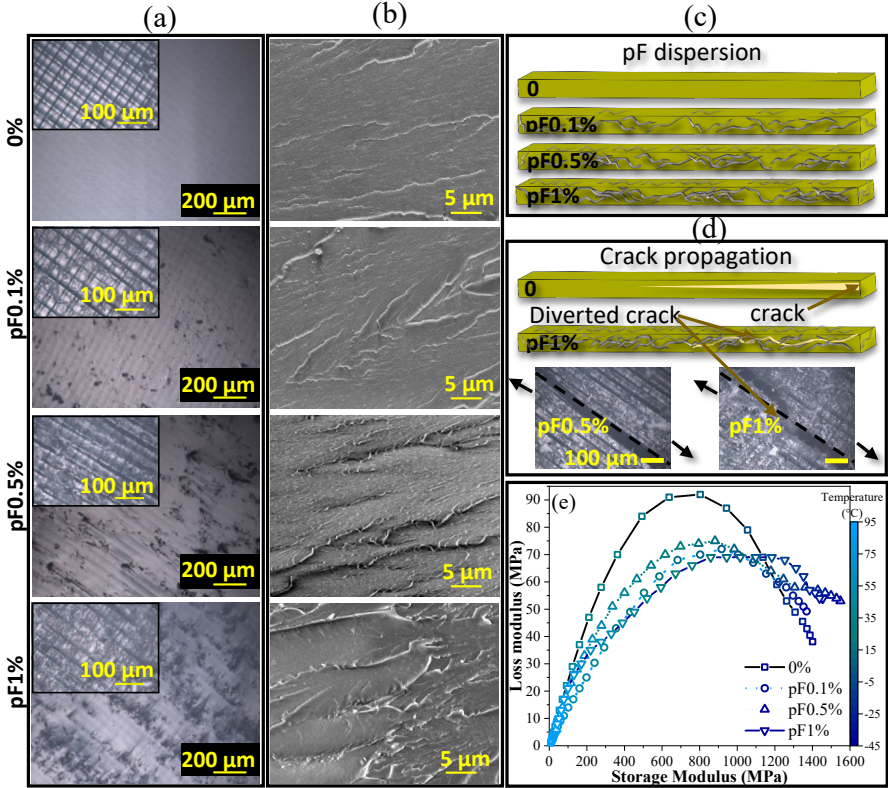

Fig. 3.19. Morphology: optical microscope images of cross-sections (insets, 20× magnification) and freeze-fracture surfaces (10× magnification) (a); SEM micrographs of freeze-fracture surfaces (2 500× magnification) (b); schematic of possible pF distribution (c); illustrations and optical microscope images of crack propagation following tensile testing (20× magnification, tensile test direction indicated with the arrows) (d); and DMA Cole-Cole plots (e) of 3D printed neat (0%) and pF reinforced composite specimens.

Figure 3.19 (c) depicts the modified fracture mechanism with crack propagation in neat polymer matrices and reinforced composites for flexural specimens. Crack deflection is confirmed by the visible cracks on the side of the rectangular samples after flexural testing as shown in the optical microscopy image of the pF1% composite sample (Fig. 3.19 (d)). Again, crack deflection is observed, as well as bifurcation in some instances. No such cracks were observed in the 0% and pF0.1% samples. Nonetheless, black dashed lines (aligned with printing layers) show that these cracks develop perpendicular to the layers, not parallel to them, confirming a high level of interlayer adhesion. The image shows that the most homogeneous specimen is the neat resin, followed by pF0.1%. In contrast, heterogeneity can be seen in the pF0.5% and pF1% samples, where cracks have separated smooth and rough black regions. The heterogeneity with increasing pF content is observed in Fig. 3.19 (c), where nanocellulose distribution in the polymer matrix is shown.

The DMA Cole-Cole plot in Fig. 3.19 (e) also confirms increasing heterogeneity with increased pF content. The Cole-Cole plots for the 0% and pF0.1% samples in Fig. 3.19 (e) possess semi-arch shapes, while at lower temperatures the same plots for the pF0.5% and pF1% specimens show deviations from a semi-arch shape. This confirms optical microscopy and SEM results indicating that, when the pF content exceeds percolation threshold of ~ 0.1 wt%, pF tends to agglomerate in the resin, thereby creating a heterogeneous system.

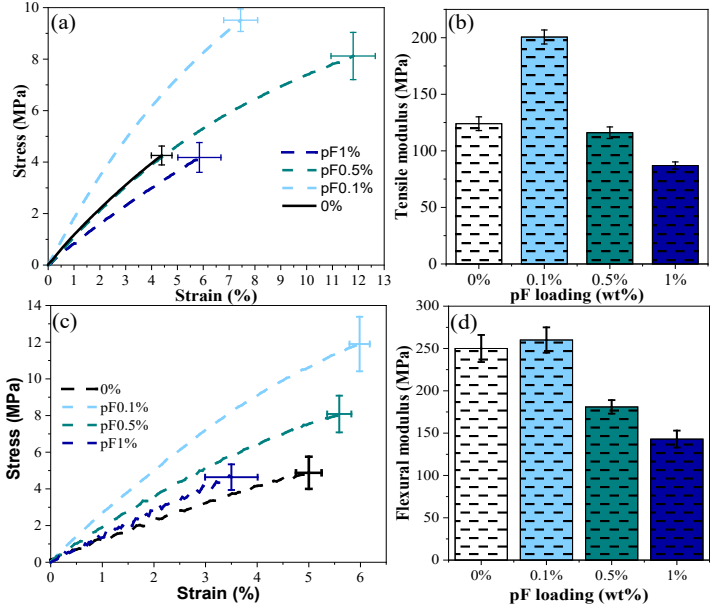### 3.3.1.4. Mechanical properties

Fig. 3.20. Tensile test results for neat and pF reinforced formulations: stress vs. strain (a), tensile modulus (b); flexural tests results: stress vs. strain (c), flexural modulus (d).

The mechanical properties data show the largest increases in tensile and flexural stress, modulus, and flexural strain at 0.1 wt% pF; higher pF concentrations result in decreases (Fig. 3.20). The addition of 0.1 wt% pF resulted in 2.3-fold and 2.4-fold increases in tensile and flexural strength (Fig. 3.20 (a) and (c), respectively). Tensile and flexural strains also show 1.7-fold and 1.2-fold increases, as well as a 1.6-fold and 5 % increase in tensile and flexural moduli (Fig. 3.20 (b) and (d), respectively).

The pF0.5% composite also showed significant enhancements in tensile and flexural strength and strain vs. the neat material. In fact, for the tension test, the largest increase in strain at break (2.7-fold) was achieved at the 0.5 wt% pF content (vs. 0.1 wt% pF in the case of flexural testing). The tensile strain at break for pF0.5% is 1.5-fold higher than for pF0.1% (Fig. 3.20 (a)). However, flexural strain at break in the pF0.5% composite shows a more limited (1.12-fold) increase vs. the neat resin, which is slightly lower than that observed for the pF0.1% composite. An increase in pF content to 1 wt% resulted in a decline in composite mechanical performance. Tensile and flexural strengths are similar, while modulus is reduced by 30 % and 42 %, compared to the neat resin, respectively. However, the tensile strain at the break still shows a 1.3-fold increase (Fig. 3.20 (a)).

3.3.1.5. Thermomechanical properties

The glass transition starts and ends around 0 °C and 75 °C for the 0% sample. The glass transition maximum for the 0% sample registers relatively close to the room temperature at 46 °C. Storage modulus values (Fig. 3.21 (a)) show a 2.6-fold and 13.5-fold decrease for the 0% sample at 30 °C and 50 °C compared to 0 °C. The introduction of the pF filler strongly influences the glass transition temperature (T_g), which is increased up to 82 °C (28 °C to 36 °C higher than 0%), see Fig. 3.21 (b). All three compositions, pF0.1%, pF0.5%, and pF1%, achieved excellent reinforcement in the rubbery state. The optimum filler volume content from the storage modulus values is between the 0.07 vol% and 0.71 vol%. Crosslinking density (Table 3.5) increase is observed with higher pF loadings.

The $C*$ factor as a function of volume content is presented in Fig. 3.21 (c). The lowest values obtained are around 0.2 and are achieved by volume content 0.35 vol% and 0.71 vol% samples (samples pF0.5% and pF1%, respectively), showing about 2-fold improvement compared to 0.07 vol% (sample pF0.1%). Theoretical percolation threshold (v_{rc}) for used pF is 0.07 vol% (calculated using Eq. (2.9)), which coincides with a pF0.1% sample. The reinforcement efficiency factor (r) was calculated from Eq. (2.10). Figure 3.21 (d) shows that the pF0.1% sample achieved r value 16.1, which is 1.5-fold and 2.5-fold higher than for pF0.5% and pF1%, respectively. The maximum stress transfer to reinforcement is achieved by the pF1% sample, while the strongest interaction between the filler and polymer is observed for the pF0.1% sample (r value).
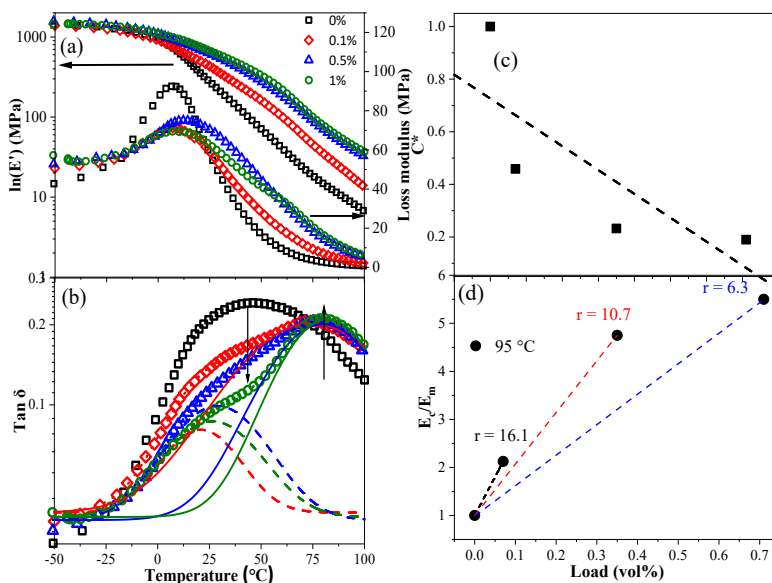
Fig. 3.21. Storage and loss modulus (a) and tanδ (b) for the SLA printed resins. The *C** factor (c) and the *r* factor as functions of volume content (d) for the SLA printed samples.

Loss modulus curves show significant change with the introduction of the pF filler. The loss peak shifts to higher temperatures while increasing the loss modulus values where the rubbery state is registered for printed nanocomposites. The increased values in the rubbery state of the loss modulus represent stronger interfacial interactions between the pF and polymer chains. This shift is visible in the splitting of the T_g peak, which moves to higher temperatures. Therefore, deconvolution was applied to the glass transition peaks (Fig. 3.21 (b)). The first smaller peak matches more with the T_g of the 0% sample, and decreased dampening peak values were observed for all filled compositions. While a new second peak is only observed for samples with the pF reinforcement. The first peak shows a polymer phase in the composite that acts similarly to the 0% sample. However, the second peak at higher temperatures has a significantly higher intensity, indicating the formation of enhanced interphase with pF addition [90]. This structure (interphase) formation dominates the nanocomposites' design and has similar dampening peak values to the 0% resin. This is more pronounced with an increase in pF loading.

pF showed a significantly lower thermal stability than the printed samples, with degradation maximums at 340 °C. However, pF loading up to 1 wt% does not cause a significant thermal stability decrease.

3.3.1.6. pF-polymer interaction

Resin, pF filler, and printed samples were characterized with FTIR spectroscopy (Fig. 3.22). Figure 3.22 (a) shows that some absorption peaks overlap between the matrix and pF filler.

Given the low filler content, there are no new peaks (Fig. 3.22 (b)) that may be attributed to pF in printed samples.
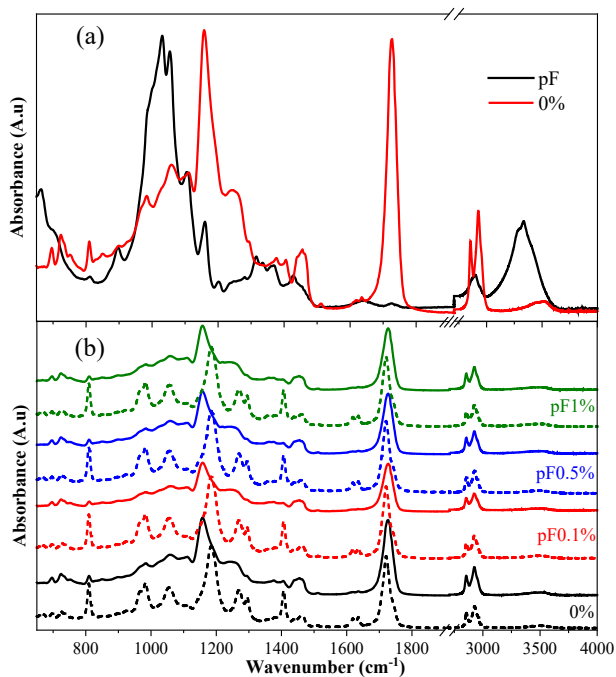

Fig. 3.22. FTIR spectra of 0% printed sample and pF filler (a), spectra of resin and printed samples 0%, pF0.1%, pF0.5% and pF1% samples (b). Dashed lines – resin; solid lines – printed samples.

The decrease of the vinyl group (at 810 cm^{-1}, 981 cm^{-1}, 1409 cm^{-1}, and 1629 cm^{-1}) absorption at 810 cm^{-1} after printing suggests that all compositions achieved excellent polymerization. The pF in a polymer matrix creates its intermolecular bonding through hydrogen bonds, obstructing vinyl group conversion and lowering light transmission [91]. This is confirmed by *DBC*% calculation using a ratio from peak intensities (C=C/COO^{-}) [79] and Flory–Rehner equation, used for Fig. 3.18 (b) and Table 3.5.
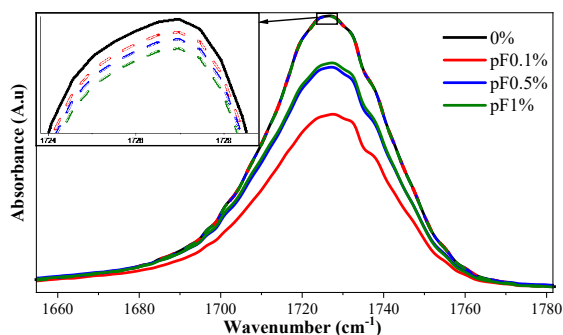
Fig. 3.23. FTIR spectra of (C=O) at 1727 cm^{-1} for printed samples. Dashed lines –
theoretical spectra obtained with Lambert–Beer's equation, solid lines – experimental spectra.

Intermolecular bonding between the filler and matrix has been proposed in other sections of the result analysis. These interactions for FTIR spectra are usually observed as peak shifts or changes in intensity. Theoretical spectra (Fig. 3.23) would be based on the acrylate matrix because there is no pF absorption at 1727 cm^{-1}. However, the C=O peak intensity decreases significantly with the introduction of the pF filler. Thus, the significant decrease in peak intensity can identify the formation of strong hydrogen bonding between the pF and matrix. The pF0.1% printed sample shows the strongest pF interaction with the matrix.

3.3.1.7. Summary

The present study demonstrates the viability of filter paper nanofibrillated cellulose (pF) as a reinforcing filler for UV-curable additive manufacturing (AM) of bio-based composite resins. Moreover, the importance of achieving a balance between agglomeration and filler network formation by utilizing filler loadings close to the percolation threshold is broadly discussed. pF volume concentration of 0.07 vol%, 0.35 vol%, and 0.71 vol% (0.1 wt%, 0.5 wt%, and 1 wt%, respectively) were introduced into the 0% resin. The printability of prepared composite resins and the structural, thermal, and thermomechanical property changes in response to the pF and polymer matrix interaction was investigated. Viscosity measurements of the prepared resins showed high viscosities for the pF0.5% and pF1% resins. Nevertheless, photos of printed objects complemented with optical microscopy images showed high printing quality. Even more so, the pF content did not affect printing accuracy at all. UV-Vis measurements showed decreased transmittance (by 34 %) and increased light scattering (by 27 %) with an increase in the pF content. The pF0.1% composite demonstrated the most significant improvements in overall mechanical performance, including enhanced tensile modulus (1.6-fold), strength (2.3-fold and 2.4-fold) and break strain (1.7-fold and 1.2-fold) in both tension and flexure, increased toughness (3-fold). Thermomechanical analysis shows a 34 °C increase in the glass transition temperature, indicating that pF interacts with the polymer matrix. The splitting of the tanδ peak proved that the introduced pF acts as a reinforcement and leads to an excellent reinforcement in the rubbery state for all reinforced samples. The C^* factor showed a 2-fold increase of reinforcement for the pF0.5% and pF1% samples, but r showed a 1.5-fold and 2.5-fold increase

for the pF0.1% in comparison to the pF0.5% and pF1%. Fourier-transform infrared spectroscopy applying Lambert–Beer's law allowed identifying stronger filler-matrix interaction for the pF0.1% sample. Stronger filler-filler interaction for the pF0.5% and pF1% samples reduces filler-matrix interaction.

All in all, this study shows that by maintaining an ultra-low pF content, pF agglomeration can be minimized, and significant improvements in mechanical performance of the bio-based UV-curable composite AM resin can be realized as a result. This work indicates that carefully designed pF composite resins for vat photopolymerization AM technologies represent promising path for reaching sustainable alternatives to commercial petroleum-based resins. Further research should concentrate on improving the interphase between the hydrophilic filler and the hydrophobic polymer matrix to increase the reinforcement benefit.

3.4. Functionalized nanocellulose-reinforced AESO resins for stereolithography

3.4.1. Nanocellulose surface functionalisation for improved interface between the reinforcement and AESO resin for stereolithography

Sample abbreviations: filter paper nanofibrillated cellulose – pF; vegetable oil (VO) formulation – VO/pF; acrylated pF – pFA; VO formulation – VO/pFA; filter paper nanocrystalline cellulose – pC; VO formulation − VO/pC; and isocyanate-functionalized pC – pCI; VO formulation − VO/pCI.

3.4.1.1. Characterization of nanocellulose fillers

Fourier transform infrared spectroscopy (FTIR) was used to investigate the chemical functionalization of the nanocellulose. FTIR spectra in Fig. 3.24 (a) show the neat pC and functionalized pCI. Absorbance peaks appear, assigned to coupled NH and CN bending vibrations at 1157 cm^{-1}, NH stretching and CN bending vibrations at 1530 cm^{-1}, and hydrogen bonded CO groups in the urethane at 1694 cm^{-1} [92]. When an excess HMDI is added, the urethane groups react with free isocyanate groups. This reaction forms a crosslinked polymer layer on the pC surface, as evidenced by the intense absorption maximum at 1651 cm^{-1} assigned to the carbonyl on the urea group [93]. The NCO peak also confirms the introduction of diisocyanate at 2264 cm^{-1}, as well as characteristic peaks at 1440 cm^{-1}, 2857 cm^{-1}, and 2933 cm^{-1} assigned to CH bending vibrations and symmetric and antisymmetric CH$_2$ vibrations, respectively [92, 94, 95]. The peak at 2890 cm^{-1}, which overlaps with peaks at 2857 cm^{-1} and 2933 cm^{-1}, is related to the CH stretching in the cellulose molecule [95]. The additional peaks at 1256 cm^{-1}, 1618 cm^{-1}, and 1580 cm^{-1} are introduced from amide, amide I, and amide II vibrations, respectively. Furthermore, at 3367 cm^{-1}, the characteristic NH stretching vibration peak can be seen, which can overlap with cellulose OH stretching vibration but appears as a sharper peak [96]. Figure 3.24 (b) represents the FTIR spectra of pF and pFA fillers. Before the functionalization, a broad absorption band at 3340 cm^{-1} corresponds to the stretching vibrations of OH groups in pF molecules. The OH groups in cellulose are replaced with acrylate groups that attach via an ester group. Consequently, the intensity of the OH bond peak is reduced, and additional sharp absorption peaks at 810 cm^{-1}, 982 cm^{-1}, 1184 cm^{-1}, 1407 cm^{-1}, 1631 cm^{-1}, and 1722 cm^{-1} have appeared. The peaks at 810 cm^{-1}, 982 cm^{-1} 1407 cm^{-1}, and 1631 cm^{-1} are attributed to the stretching vibrations of vinyl bonds in acrylic groups; meanwhile, the peaks at 1184 cm^{-1} and 1722 cm^{-1} belong to the stretching vibrations of the ester's carbonyl groups [75, 97].
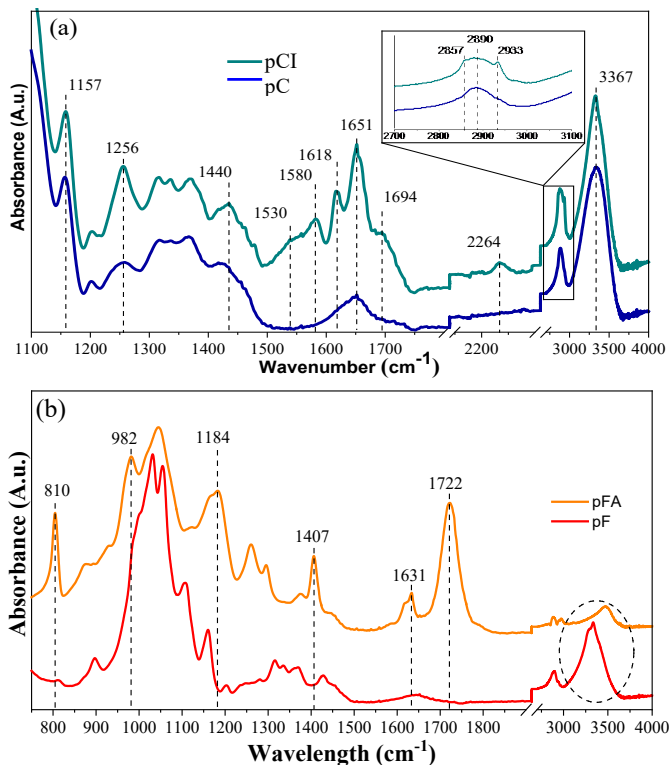
Fig. 3.24. FTIR spectra of neat pC and isocyanate functionalized pC (pCI) (a) and neat pF and acrylated pF (pFA) (b).

Alongside FTIR investigations, water contact angles (θ) of the nanocellulose were measured to assess the impact of functionalization on the hydrophobicity of the fillers. The neat nanocellulose was hydrophilic with the equilibrium θ = 0°. The functionalized nanocelluloses gave θ of 69° and 63° for pCI and pFA, respectively.

3.4.1.2. Vat photopolymerization printability of bio-based resins

The ability to achieve high print resolutions and reproduce fine details is commonly required in order to validate formulated resins. The SL1 standard calibration check model's – Petrin tower and a close up (Fig. 3.25 (a) and (b)) and Prusa clay army and a close up (Fig. 3.25 (c) and (d)) were printed using the developed nanocellulose/VO resin formulations. The bio-based vat photopolymerization resin gave very high printing resolution in the printed structures, as shown in Fig. 3.25 (e)–(i). The measured layer height was constant at 50 µm, as set during the slicing process. At the same time, the Petrin tower calibration structure (Fig. 3.25 (a) and (b)) demonstrates the possibility of printing high-quality, detailed objects with overhangs, no supports, and no missing parts. In tandem, the Prusa clay army models (Fig. 3.25 (c) and (d)) show excellent resolution for small objects with especially fine details.
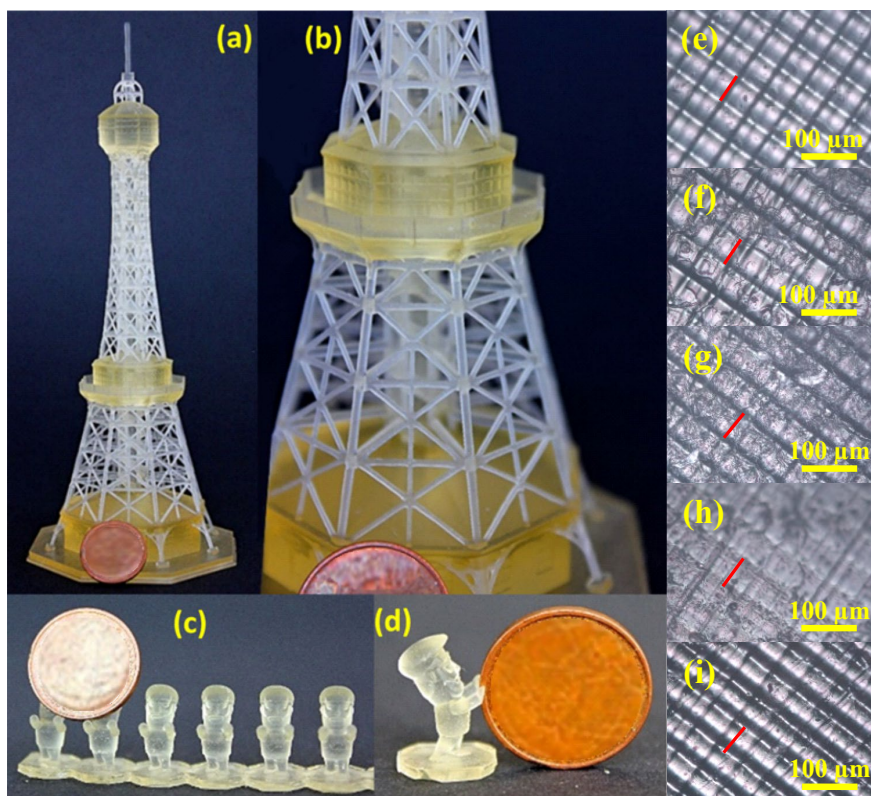
Fig. 3.25. 3D printed SL1 standard calibration check model – Petrin tower (a) and (b); Prusa clay army (c) and (d); optical microscope images of the 3D printed samples: VO (e), VO/pF (f), VO/pFA (g), VO/pC (h), and VO/pCI (i).

Using photography in conjunction with optical microscopy of printed samples provides an additional printability assessment. Polarized light optical microscope images at 20× magnification were captured to assess the layer accuracy of the printed mechanical testing samples in the Z-axis direction perpendicular to the printing plane (Fig. 3.25 (e)–(i)). Excellent printing precision was obtained for all prepared compositions. The best printing accuracy was observed for the VO and VO/pCI resins. Printing layer thickness (50 µm, red lines in Fig. 3.25 (e)–(i)) remains constant and, hence, printing accuracy is considered to be unchanged.

3.4.1.3. Macromolecular network structure

Table 3.7 provides basic physical properties data for the 3D printed polymers (density, sol-fraction) as well as the molecular weight between the crosslinks (M_c) and crosslink density (N). The N values of the composites all show significant increases compared to the VO (N_0). Given prior confirmation via FTIR of similar levels of DBC% in all cases, this result provides clear evidence of significant "physical crosslinking" (nanofiller reinforcement) even at the ultra-low nanofiller concentration of 0.07 vol% and further confirms the importance of nanofiller aspect

ratio as well, given that the higher aspect ratio pF consistently produces larger increases vs. the lower aspect ratio pC, regardless of surface chemistry. Furthermore, surface-modified nanofillers are shown to provide consistently higher crosslink densities than their unmodified counterparts.

<div align="right">Table 3.7</div>

Parameters of 3D Printed Samples

Sample	Density, g/cm³	Sol-fraction, %	DBC%	M_c, g/mol	N, mmol/cm³	$\Delta N/N_0$, %
VO	1.116 ± 0.0012	3.69 ± 0.20	84	1021	1.1	-
VO/pF	1.117 ± 0.0008	4.39 ± 0.12	82	464	2.4	+118
VO/pFA	1.118 ± 0.0017	5.12 ± 0.27	81	426	2.7	+145
VO/pC	1.119 ± 0.0013	4.10 ± 0.41	76	731	1.5	+36
VO/pCI	1.118 ± 0.0016	3.99 ± 0.40	79	568	2.0	+81

Consistent with the very low nanofiller concentrations studied here, the obtained thermograms imply that the addition of cellulose does not significantly affect the degradation mechanism of 3D printed samples.

Fig. 3.26 (a) compares the storage modulus of the VO to composites loaded with different nanocellulose types. At 20 °C, the stiffness of composites improves by 1.34-fold to 1.80-fold compared to the VO. This correlates well with the elastic modulus of the tensile test (Fig. 3.27). In the glassy state, the matrix properties more strongly determine the achieved storage modulus, whereas a transition to a viscoelastic state yields a significant increase in values over the unfilled VO as the reinforcement begins to bear the load [50].

Figure 3.26 (b) shows the changes in loss modulus values after adding nanocellulose fillers. For all composites except VO/pFA, the loss modulus peak became narrower and weaker as compared to the pure VO. Above the glass transition, loss modulus values are higher for all composites vs. the VO.
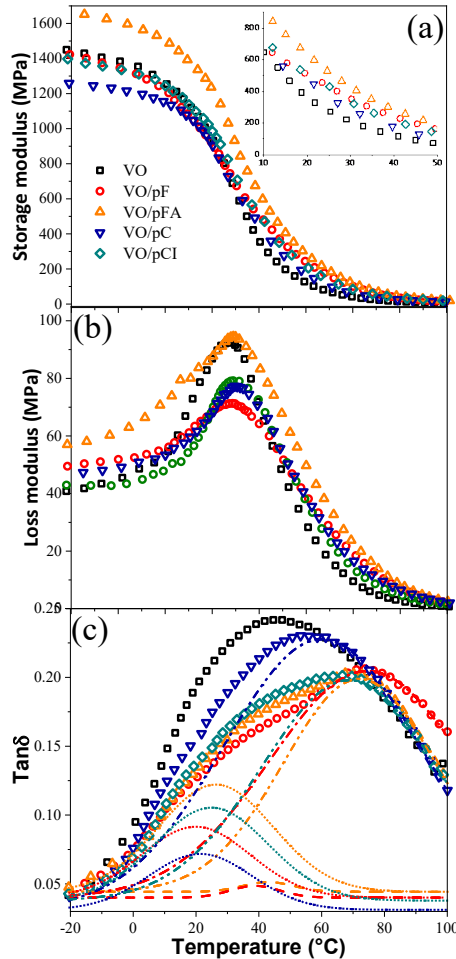
Fig. 3.26. Storage (a), loss modulus (b), and tanδ (c) curves of 3D printed samples.

In line with the observed increases in crosslink densities (Table 3.7), a clear decrease in tanδ around the glass transition was observed for all composites as compared to the VO. The peak of tanδ is commonly attributed to the glass transition temperature (T_{g3}) [98]. The complex photocurable resin composition contributes to a relatively broad VO tanδ peak, which narrows for composites and shows a shoulder for some compositions. To better understand the shift in the composite's structure, deconvolution was applied to tanδ curves (Fig. 3.26 (c)), and the resulting values are presented in T_{g1} and T_{g2}. Compared to VO, a clear shift in the glass transition to higher temperatures was visible for all composites.

The inclusion of nanocellulose fillers drastically improved the mechanical performance of all samples (Fig. 3.27). All composite elastic modulus values increased nearly 2-fold. The stiffness of the VO/pC and VO/pCI composites was the highest, with an increase of up to 95 % compared to neat VO. VO/pC and VO/pCI modulus results are comparable within the margin

of error. VO/pF and VO/pFA show modulus values that are ~ 60 % and ~ 70 % higher, respectively, as compared to VO.
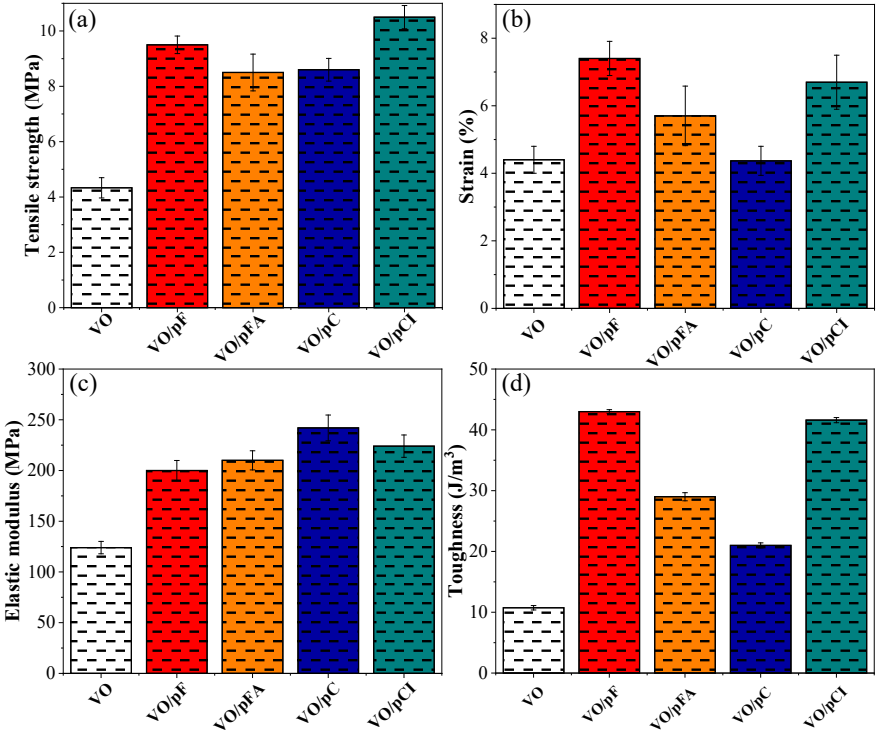

Fig. 3.27. Tensile strength (a), failure strain (b), modulus (c) and toughness (d) graphs of 3D printed samples.

It can be seen in Fig. 3.27 (a) and (b) that the addition of nanocellulose had a significant impact on the tensile strength and failure strain of the composites. Compared to VO, the addition of pF led to a ~ 70 % increase in failure strain. The functionalization of pF to form pFA resulted in a reduction in failure strain but no statistically significant changes in strength. Compared to the VO, VO/pCI showed 144 % and 52 % increases in tensile strength and strain, respectively. The chosen functionalization improves the wettability and adhesion between the VO and pCI. Improved compatibility also results in a more uniform distribution of particles and a lower tendency to form agglomerates. Figure 3.27 (d) displays the toughness of all samples. VO/pF and VO/pCI achieved an impressive toughness increase of ~ 30 J/m^3 (+300 %), consistent with a high resistance to deformation without failure of the material. Toughness is a desirable polymer material property, and it is evident that nanocellulose introduction led to at least a 2-fold increase in composite toughness compared to the VO.

Figure 3.28 shows SEM images of the fracture surfaces of printed samples fractured following exposure to liquid nitrogen. The images show that the fracture surface of the printed VO resin is smooth. However, with the exception of VO/pCI, reinforced resins exhibit a

significantly different fracture pattern. The roughness of the fracture surface increases dramatically after the nanocellulose fillers are incorporated into the VO matrix. The difference between the VO and VO/pCI is less pronounced, but the pattern differs from the smooth fractures of the VO. The roughness is very similar for the VO/pF and VO/pC composites, while VO/pFA exhibits a more intense fracture surface roughness.
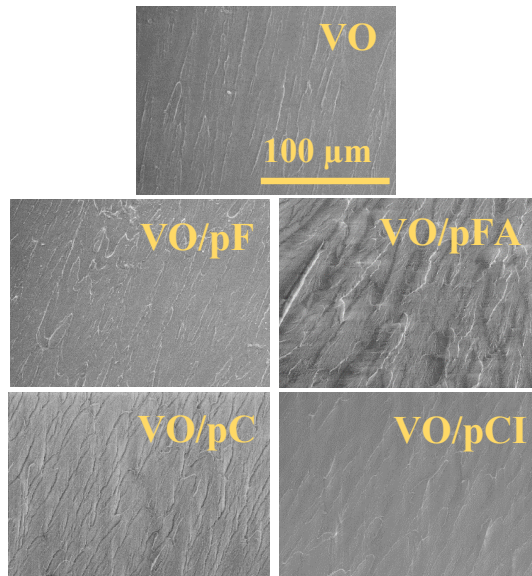

Fig. 3.28. SEM micrographs of the fracture surface of 3D printed samples.

3.4.1.4. Reinforcement efficiency analysis

The developed interphase structure is proposed in Scheme 3.1. It shows both covalent bonding and physical interactions developing at the cellulose-polymer interface. Overall, there are at least three attractive forces that could contribute to filler-matrix interactions: hydrogen bonding (OH ||| O=C for all used fillers; NH ||| O=C for pCI), covalent bonds (pFA), and Van der Waals forces (pCI) (see Scheme 3.1). Scheme 3.1 (b) and (c) shows that even after functionalization in VO/pCI and VO/pFA, respectively, due to the likelihood of incomplete surface modification, the potential for hydrogen bonding with the remaining OH groups of the cellulose remains. For this reason and regardless of modifications, all the fillers studied here are expected to possess the capacity to form OH ||| O=C hydrogen bonds with the polymer matrix. Additionally, in the case of pCI, hydrogen bonding is also possible between the NH moieties introduced thanks to HMDI modification and the carbonyls in the polymer matrix.
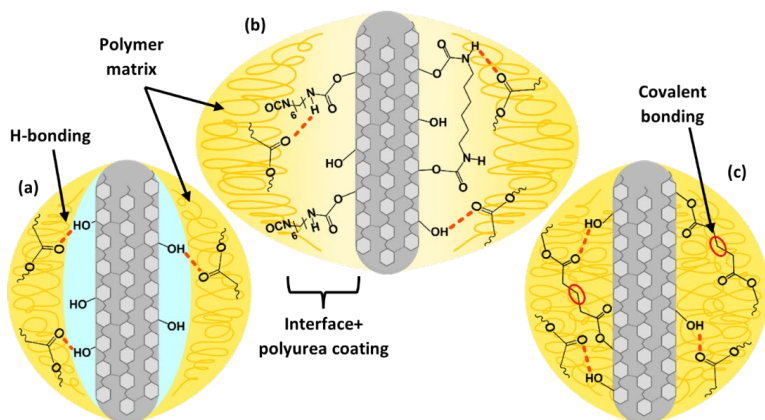
Scheme 3.1. Proposed filler-matrix interaction's schematic representation for VO/pC and VO/pF (a), VO/pCI (b), and VO/pFA (c).

To further assess achieved reinforcement by different nanocellulose, the filler-matrix stress efficiency transfer parameter C^*, adhesion factor A, and reinforcement efficiency parameter r, summarized in Table 3.8, were calculated according to Eqs. (2.8), (2.9), and (2.10). The incorporation of nanocellulose fillers results in stress transfer from the polymer matrix to the nanocellulose, with values of C^* ranging from 0.37 to 0.50. These significant reductions in C^* imply excellent stress transfer from the polymer matrix to the nanocellulose fillers. Remarkably, the VO/pFA and VO/pCI composites show 25 % and 28 % lower C^* parameter values than composites based on the analogous neat (unmodified) fillers, implying better filler effectiveness for composite reinforcement.

Filler functionalization increases interfacial adhesion with the VO matrix in both cases. This is consistent with the ability of pFA to form covalent bonds with the VO matrix (Scheme 3.1), as the A value for the VO/pFA composites is lower compared to pF. It should be noted that the addition of pCI to the VO matrix resulted in an apparent decrease in the A parameter as well, again indicating a significant improvement in adhesion. As shown in Scheme 3.1, this effect is achieved through functionalization, resulting in increased wetting of pCI particles and forming an interface with the VO matrix.

Table 3.8

The r, C^*, and A Parameters of 3D Printed Samples

Sample	r	C^*	A
VO/pF	16.1	0.46	–0.313
VO/pFA	28.6	0.37	–0.339
VO/pC	10.7	0.50	–0.199
VO/pCI	21.4	0.39	–0.287

The increase in the *r* parameter shows improved filler-matrix reinforcement effectiveness. When judged by *r* values, pF appears to be more effective than pC in reinforcing the VO matrix, with the same tendency observed when comparing VO/pFA and VO/pCI. Surface functionalization approximately doubles reinforcement effectiveness, though the effect is slightly more pronounced in the case of VO/pCI. The lower *C** and much higher *r* values in the case of pC in comparison with pF demonstrate that with such low concentrations, pF is a more suitable filler for the VO matrix. Higher aspect ratios facilitate the creation of a filler network, while in the VO/pFA composite, covalent bonding between the filler and the polymer matrix contributes even more to the filler's ability to reinforce the VO matrix.

3.4.1.5. Performance properties comparison

The storage modulus ratio plot in Fig. 3.29 (a) shows an increase at temperatures similar to those determined from the deconvolution of the tanδ peaks. It is seen that until about 20 °C, there is no significant reinforcement evidence for any of the obtained composites. The exception is VO/pFA because of the filler-matrix covalent bonding. The absence of any substantial effect relates to the T_g of the samples. Below the T_g, all segmental mobility is strictly limited, and fillers accept only minimal loads from the polymer matrix, as seen in Fig. 3.29 (a). All composites exhibit reinforcement at the T_{g1} temperature ranging from 20 °C to 26 °C, with the effect increasing until the T_{g3} is reached. As the segmental mobility of the polymer chains continues to rise as T_{g3} is exceeded, the reinforcement effects decrease with further temperature increases.

VO/pFA shows the highest storage modulus ratio across all temperature ranges, consistent with results obtained for *C** and *r* parameters. However, some competition exists between the VO/pCI and VO/pF composites when it comes to the next best system. VO/pCI exhibits a higher relative modulus at temperatures ranging from –10 °C to 25 °C, which it maintains as the glass transition begins thanks to strong adhesion between the pCI and the VO matrix as a result of the surface functionalization of the filler. Nevertheless, as the temperature continues to increase, pF provides a greater relative modulus, presumably thanks to its higher aspect ratio and greater crosslink density.
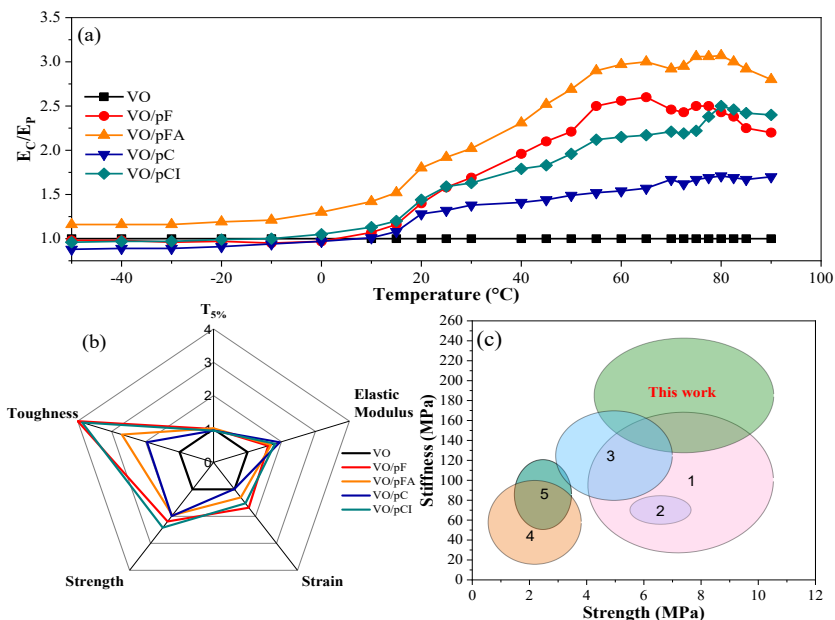
Fig. 3.29. Ratio between composite (E_c) and VO (E_p) storage modulus values (a); relative changes of performance properties for 3D printed samples. Value 1 represents the VO (at 20 °C) (b); comparison of tensile performance of AESO/cellulose composites from this work and the literature (c). 1 – AESO/methyl acrylate functionalized cellulose 5–30 wt% (3D printed) [99]; 2 – AESO/acrylate or HDTMA functionalized C 1–2 wt% (films) [33]; 3 – AESO/micro- or nanocrystalline cellulose 0.15–2.4 wt% (3D printed) [54]; 4 – AESO/macadamia shell microcrystalline cellulose 1–10 wt% (3D printed) [100]; 5 – AESO/cellulose (1 mm particles) 5–10 wt% (cured composites) [101].

The radial plot in Fig. 3.29 (b) displays a summary of mechanical performance observations of 3D printed samples – strain at break, tensile strength, tensile modulus, tensile toughness, and temperature at 5 % mass loss. The relative changes in desired parameters for prepared composites are presented and referenced to VO. The tensile performance of VO/pF and VO/pCI was the highest of all printed composites. Incorporating pF and pCI into the VO matrix resulted in an almost 4-fold increase in toughness while substantially improving other parameters in tandem. VO/pC showed the highest 2-fold increase in tensile modulus of all 3D printed samples. The thermal stability of all composites remained similar to VO, with only minor differences in overall performance. All composites' performance was improved compared to the VO, demonstrating the effectiveness of nanocellulose and its various functionalization methods for the reinforcement of 3D printed bio-based polymer resins. In addition, the variations observed as a function of filler type and surface functionalization provide the ability to tune composite performance for specific applications.

To better understand the mechanical performance of the prepared AESO-based composites with cellulose fillers, tensile test results were compared with those found in the literature and summarized in Fig. 3.29 (c). Liu et al. demonstrated syringe 3D printed AESO composites

loaded with methyl acrylate functionalized cellulose range from 5 wt% to 30 wt% [99]. Highly loaded composites showed increased tensile strength up to 11.5 MPa and modulus values of up to 167 MPa, against 4.3 MPa and 27.4 MPa for neat AESO, respectively. Palucci Rosa et al. used two different cellulose sizes, microcrystalline cellulose and C, to prepare AESO-based composites for vat photopolymerization 3D printing [54]. At low loadings, microcrystalline cellulose and C gave similar tensile strength values (~ 3 MPa), with further increases up to 4.5 MPa and 7 MPa, respectively, at higher concentrations. Noe et al. prepared bio-based resins suitable for vat photopolymerization 3D printing using macadamia shell lignocellulosic waste (1–10 wt%) [100]. Higher filler loadings increased strength from about 0.5 MPa to 2.5 MPa, and modulus from 3.8 MPa to 100 MPa. Seabra et al. prepared thermosetting biodegradable composites by combining AESO-based resin with fragments of sisal rope [101]. The tensile strength results ranged from approximately 3.25 MPa for unfilled samples to 1.75 MPa for the samples containing 10 wt% filler as well as a higher hardener content. Overall, the formulation of neat resin combined with ultra-low loadings of nanofillers, as represented in this paper, appears to provide better mechanical performance than all prior attempts found by our team at the time of this research.

3.4.1.6. Summary

This work successfully demonstrates additive manufacturing (AM) via vat photopolymerization of bio-based vegetable oil (VO) resins containing ultra-low concentrations of neat and functionalized nanocellulose with high printing resolution and favourable filler-matrix interactions. To the best of the authors' knowledge, this report is the first to demonstrate the use of acrylate-functionalized pF as an efficient reinforcement in a 3D printing resin. The introduction of nanofillers did not affect the printing quality. The introduction of nanocellulose into VO resins provided up to a 2.5-fold increase in strength and a 4-fold increase in toughness of the 3D printed samples, with an even more pronounced effect for functionalized fillers. Functionalization of the fillers led to improved filler-matrix adhesion in the case of VO/pCI and chemical bonding for VO/pFA, a prerequisite condition for improving composite properties, with these results reflected in crosslink density calculations as well. Reinforcement efficiency, VO/pFA showed 1.24-fold lower C^* and 1.77-fold higher r parameters than VO/pF. VO/pCI achieved a 1.28-fold lower C^* and a 2-fold higher r than VO/pC.

Overall, this work shows that the addition of ultra-low concentrations (0.07 vol%) of nanocellulose into a VO resin represents a promising means of strengthening sustainable vat photopolymerization resins. Even more so, more remarkable improvement can be achieved by using pF rather than pC at the ultra-low concentration. At the same time, the functionalization of fillers can help to overcome filler-matrix compatibility issues at the interface. As a result, well-designed VO-based composite resins could represent sustainable alternatives to conventional petroleum resins. Furthermore, the combination with nanocellulose fillers promises new types of reinforced materials, driving even greater adoption of UV-assisted AM techniques.

3.5. Accelerated weathering performance analysis of nanocellulose-reinforced vegetable oil-based resins for stereolithography

3.5.1. Nanofibrillated-cellulose effect on vegetable oil-based composite durability during QUV accelerated weathering

*Sample abbreviations: all resin formulations were named in accordance with the filter paper nanofibrillated cellulose (pF) loading as follows: 0%, pF0.1%, and pF0.5%.

3.5.1.1. Morphology

Visual examination in Fig. 3.30 (a) clearly shows the yellowing of all samples already after 250 h in the UV weathering camera for all compositions, while precise quantitative colorimetric values are summarized in Fig. 3.30 (b). Filter paper nanofibrillated cellulose (pF) addition (both concentrations of 0.1 and 0.5 wt%) has prevented surface cracking observed for the 0% composition. UV-Vis spectroscopy measurements (in Fig. 3.30 (a)) data show that the 0% composition has the highest transparency (78.0 %) at 500 nm, followed by pF0.1% and pF0.5% compositions (76.0 % and 60.5 %, respectively). For all compositions, after 1000 h of UV weathering, transparency decreases to 49.0 %, 47.8 %, and 37.0 % for 0%, pF0.1%, and pF0.5% compositions. 0% and pF0.1% compositions act similarly (transparency decreases by 29.0 % and 28.2 %, respectively), while the pF0.5% sample's transparency decrease is less pronounced (23.5 %). Scattering shows that the pF0.5% composition has the highest values of 29.5 % and 54.8 % at 0 h and 1000 h, respectively.
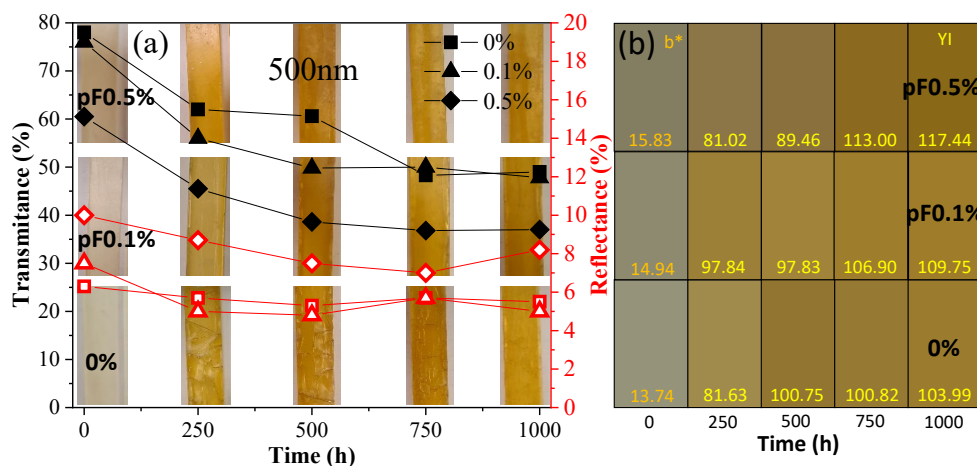
Fig. 3.30. Images of the sample surfaces during UV weathering with a UV-Vis 500 nm overlay tracking changes in transmittance and reflectance data (a) and colorimetry data (b).

Colorimetry images and the yellowing index (YI) with b* (attributes for yellow color) can be seen in Fig. 3.30 (b). pF introduction makes samples slightly more yellow, while the L* parameter (lightness/brightness) shows that pF makes the samples darker: 60.63, 56.90, and

51.68 for 0%, pF0.1%, and pF0.5% 0 h samples, respectively (visually, the samples with pF are more matte). 0%, pF0.1%, and pF0.5% samples get more yellow between 250 h and 1000 h by 27.39 %, 12.17 %, and 44.95 %, respectively. It was also observed that pF delays yellowing. 0% showed the most incredible jump between 250 h and 500 h, while for pF0.1%, there was almost no difference between 250 h and 500 h, and a shift can be observed at 750 h. In turn, the pF0.5% sample shows a steady climb in yellowing throughout the weathering.

After flexural testing, additional visual investigations were performed with optical microscopy imaging at 200× magnification of the sample top and side surfaces. The obtained top and side images of the weathered samples can be seen in Fig. 3.31. Optical microscopy confirms the conclusion of the visual examination analysis. The top surface of the 0% sample cracked during the weathering in the UV chamber, while pF0.1% and pF0.5% showed no cracks (cracking observed before flexural testing). There are no cracks for the 0% sample top surfaces with 0 h exposure to UV weathering, but cracks are visible for the samples after UV weathering. It is visible that flexural testing has introduced large cracks through the sample volume.
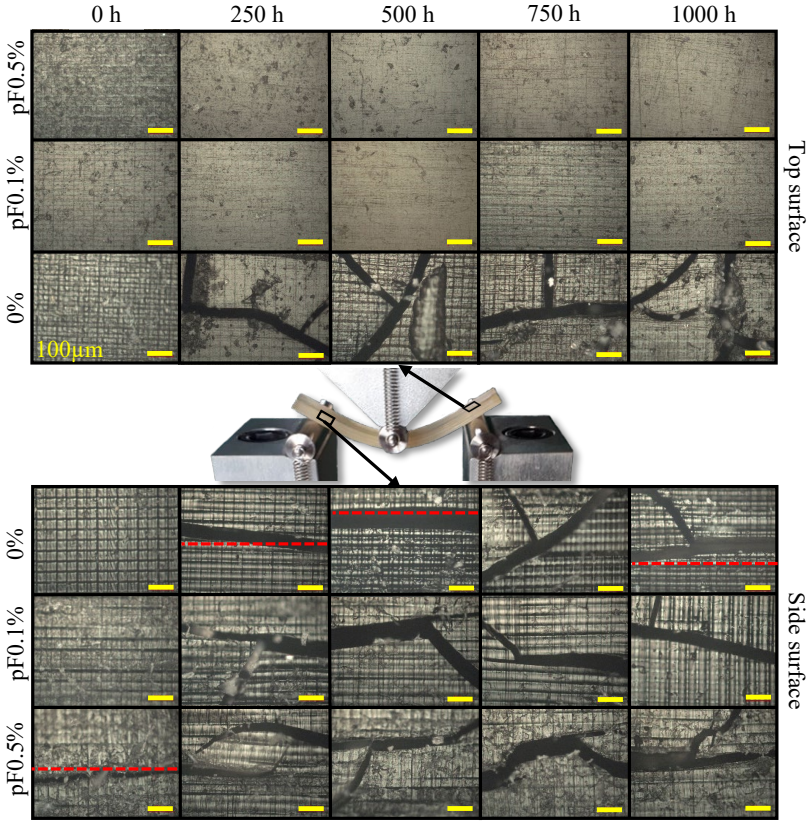

Fig. 3.31. Optical microscopy images at magnification 200× of the prepared composition sample top and side surfaces during UV weathering after flexural testing are depicted in the middle of the image.

In Fig. 3.31, 0% and pF0.1% samples show no cracks at 0 h exposure, while a pF0.5% sample shows a crack. Crack propagation for the 0 h pF0.5% sample and the rest of the samples during UV weathering happens crossing the printed layers. For better observation, red dotted lines in Fig. 3.31 are provided where crack paths crossing the layers could be in question. The observed crack propagation paths testify to excellent layer adhesion during the printing [102], which is not affected by UV weathering at all. Also, crack path sharp edges and direction changes can be observed with increased pF content, testifying to the reinforcement effect of the introduced pF causing crack deflection [55, 103, 104].

All samples show weight increases (Fig. 3.32 (a)), which can be attributed to the absorbed water that fills the space between polymer molecules [105]. In addition, increasing hydrophilic pF content leads to a higher weight increase. Sol-fraction decreased (Fig. 3.32 (b)) due to the additional UV-light exposure during weathering, acting as additional post-curing that would reduce sol-fraction. The low content of the introduced pF correlated with an increase in sample weight and density.
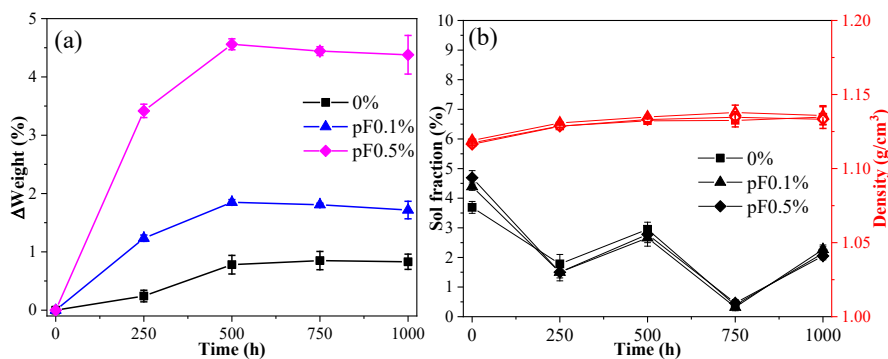
Fig. 3.32. The prepared composition samples' weight changes (a), sol-fraction, and densities (b) during the UV weathering.

3.5.1.2. Chemical degradation processes

FTIR measurements were performed to characterize the chemical modifications imposed by UV weathering (Fig. 3.33). A schematic representation of a crosslinked polymer network is shown in Fig. 3.33 (a), where potential photodegradation locations are marked (circled ester bonds), and blue bonds show the crosslinks between monomers. Figure 3.33 (b) shows the ester bond cleavage in the middle of the chain network, while Fig. 3.33 (c) shows the ester bond at a terminal, located close to the chain network end (terminal group).
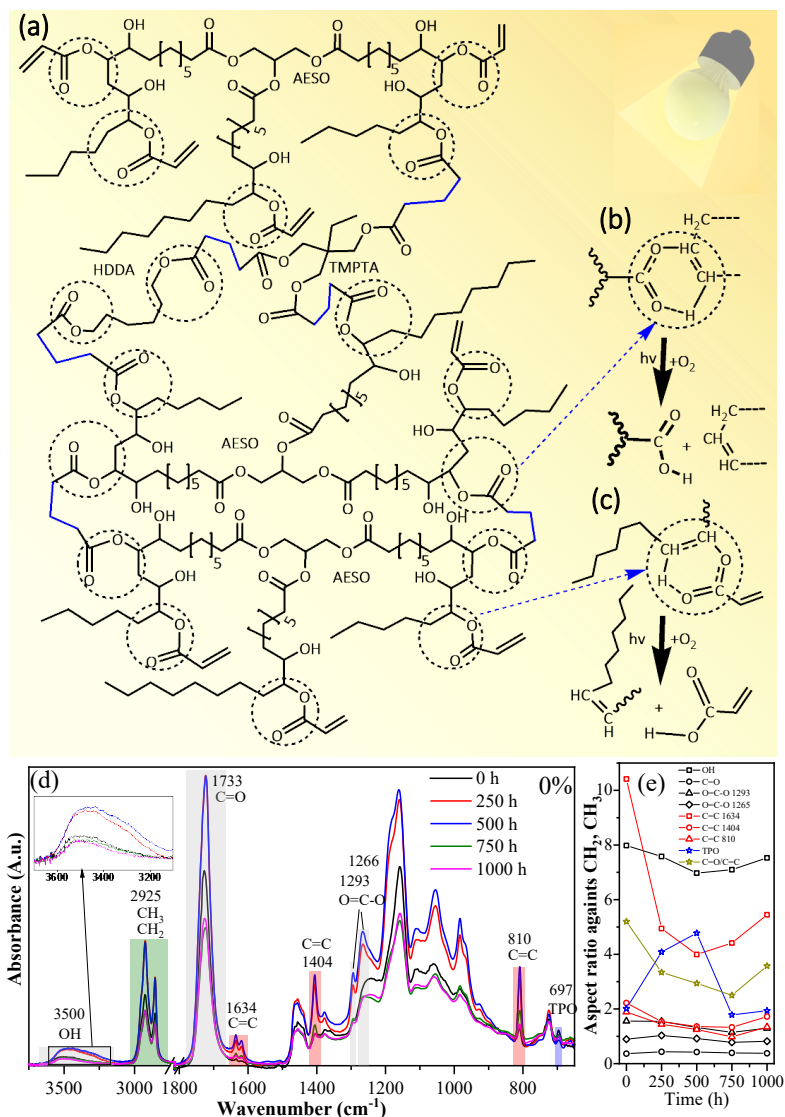
Fig. 3.33. Crosslinked polymer matrix with dash circles marking possible degradation spots and blue bonds where monomers are crosslinked (a), photocleavage mechanisms and products at the crosslinked network (b), and close to terminal group (c); 0% sample FTIR spectra (d), and peak intensity ratios (e) during UV weathering.

FTIR spectra reveal a trend of increasing C=C bonds, marked red in Fig. 3.33 (d). Simultaneously, the generated C=C bonds can be used in new crosslinks to form oligomers or to add chain length to the existing network. The peak intensity ratio graph was created in Fig. 3.33 (e) for better visualization of characteristic peak changes. As a reference peak, the 2925 cm^{-1} peak attributed to the CH$_2$ and CH$_3$ was chosen, and other appropriate intensities (attributed accordingly to C=C, OH, O=C-O, or TPO, as shown in Fig. 3.33 (d)) were used to

divide its intensity. The peak at 697 cm^{-1} was attributed to TPO. Figure 3.33 (e), with the peak intensity ratios, shows that the TPO content during UV weathering decreases while C=C increases, confirming the reported photo-cleavage [106]. Similar observations can be seen for the OH peak at 3500 cm^{-1}. The pF0.1% and pF0.5% photodegradation spectra, compared to 0%, show the same trends but are less pronounced. This indicates a lesser weathering impact on the samples, confirming the beneficial aspect of introducing pF.

3.5.1.3. Thermomechanical properties
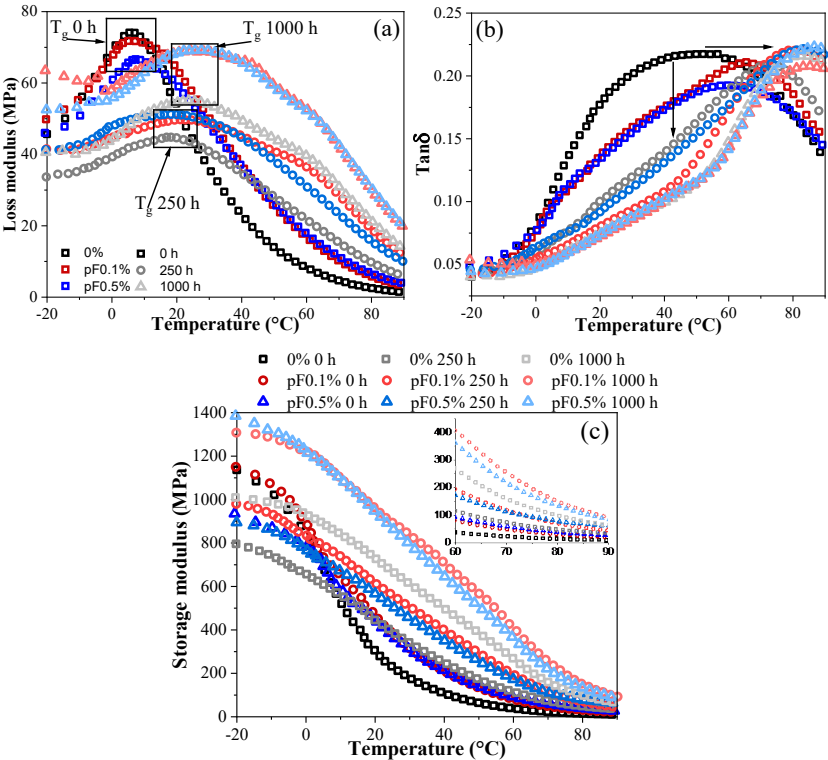
Fig. 3.34. DMA measurement results: loss moduli (a), tanδ (b), and storage moduli (c) during UV weathering at 0 h, 250 h, and 1000 h.

Mechanical and thermomechanical performance changes were measured depending on weathering to show bulk property changes. DMA curves of samples before and after 250 h and 1000 h weathering are shown in Fig. 3.34. Significant structural changes are indicated by loss modulus curves depicting about a 20 °C increase in the glass transition temperature. For the 0 h samples, the glass transitions temperature ranges from 6 °C to 7 °C, 250 h from 18 °C to 22 °C, and 1000 h from 23 °C to 26 °C. This indicates that initial UV exposure works as an additional post-curing of the acrylate matrix, while further UV exposure has a relatively limited effect.

By having a wider tanδ peak with a large shoulder at lower temperatures, it is clear that the degradation results in less uniform structures. The main peak of tanδ depicts the relaxation of the primary phase; the long trailing shoulder indicates the presence of lower molecular weight molecules and the plasticizing effect of absorbed water [107, 108]. Both loss modulus and tanδ peaks indicate that the 1000 h samples are more crosslinked than the 0 h and 250 h samples.

Storage modulus curves indicate that pF filler has not been compromised by the presence of water or photodegradation. In all three cases for 0 h, 250 h, and 1000 h above the glass transitions, the pF filled samples show significantly higher storage modulus values in the measured temperature range. The increase of storage modulus at room temperature is up to 4-fold. At the same time, it is visible that the storage modulus values for pF0.1% and pF0.5% are close, and more often, pF0.1% shows higher values.

3.5.1.4. Mechanical properties

Figure 3.35 depicts tensile and flexural testing results after weathering. The initial properties at 0 h of composites favor the pF0.1% sample in tensile properties, while both pF loadings scale well with flexural properties. The observed overall tendency for tensile strain is to decrease with increased exposure time. Tensile strain values shown in Fig. 3.35 (a) reveal that ductility decreases after just 250 h for the 0% sample; however, pF0.1% and pF0.5% samples retain some of the ductility and see a more gradual decline before 1000 h weathering, where they reach similar values to that of 0%. The mechanical testing was performed at 20 °C, while DMA shows that during weathering, the glass transition significantly jumped from 6 °C up to 26 °C. This indicates that samples at 0 h have higher segmental mobility and, thus, should have higher strain values. Surprisingly, flexural strain in Fig. 3.35 (a), shows somewhat different tendencies to those observed for the tensile strain before reaching 1000 h, where a notable drop occurs. Flexural strain increase seems to correlate with the absorbed water content, which relates to pF content, thus explaining the relatively large values observed for pF0.5%.

Both tensile (Fig. 3.35 (b)) and flexural (Fig. 3.35 (c)) moduli increase after weathering. Table 3.9 shows all the moduli increasing as folds compared to the neat 0 h sample. For the tensile moduli, the increase is higher than for the flexural moduli, and the final values after weathering are within a margin of error for all compositions. In the case of flexural moduli, the values started to scale with pF loading from 250 h.

Figure 3.35 (d) with tensile and flexural stress values shows that for the 0% sample, the tensile stress increases after 250 h of weathering and stays constant within the error bar range throughout the weathering. The stress bars for samples pF0.1% and pF0.5% increased to 750 h, but a sharp drop in performance was observed at 1000 h. The already discussed increase in the glass transition temperature would indicate that at 1000 h, the properties should depend more on the matrix rather than reinforcement. Still, it can be observed that flexural stress values scaled with pF content even after 1000 h of exposure, and only tensile stress values were somewhat levelled. The weathering shows that the appropriate pF content for tensile properties is 0.1 wt%, and for flexural properties it is 0.5 wt%.
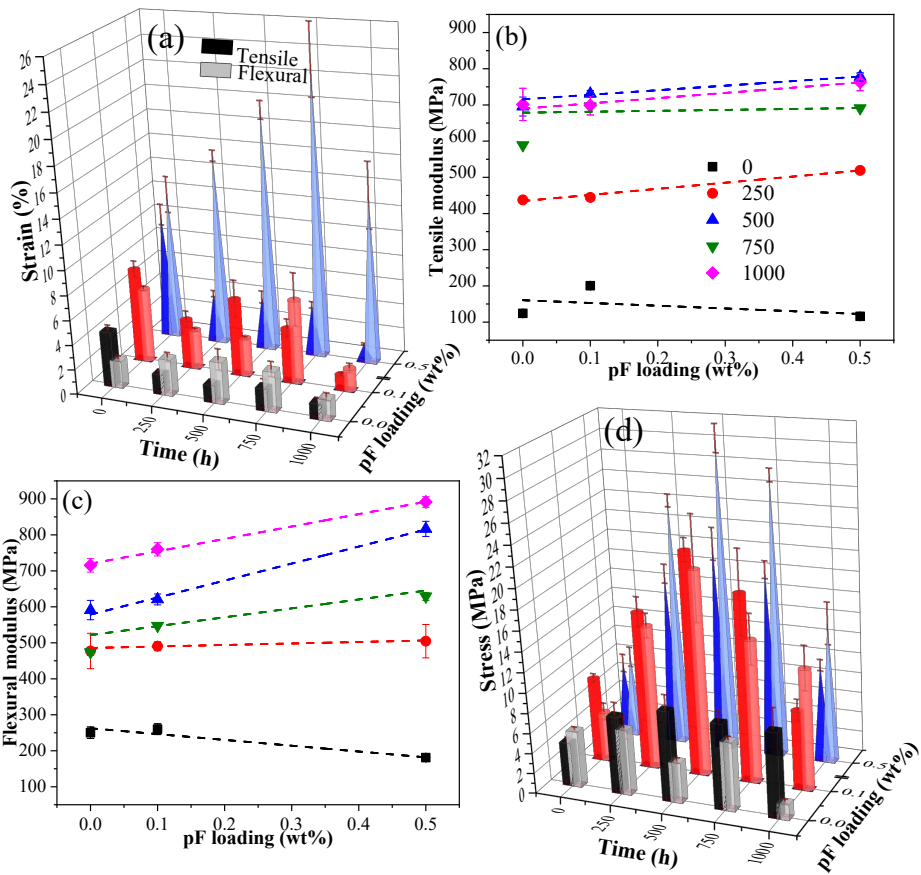
Fig. 3.35. Tensile test results of the prepared composition samples during the UV weathering: tensile (left column) and flexural (right column) strain (a); tensile modulus (b); tensile (left column) and flexural (right column) stress (c); and flexural modulus (d).

Table 3.9

Increase in Mechanical Moduli of the Prepared Composition Samples after UV Weathering

Weathering time	0%		pF0.1%		pF0.5%	
	Tensile (x-fold)	Flexural (x-fold)	Tensile (x-fold)	Flexural (x-fold)	Tensile (x-fold)	Flexural (x-fold)
250 h	2.5	0.91	1.22	0.88	3.47	1.78
500 h	4.6	1.36	2.65	1.38	5.70	3.51
750 h	3.75	0.90	2.48	1.10	4.96	2.47
1000 h	4.65	1.86	2.81	1.92	5.58	3.92

3.5.1.5. Summary

A bio-based acrylic resin for vat photopolymerization was prepared using acrylated epoxidized soybean oil and filter paper nanofibrillated cellulose (pF). The QUV accelerated weathering impact on 3D-printed rectangular-shape samples was examined to understand complex relationships between the surface and bulk degradation processes. Morphology investigations showed that pF introduction delays the yellowing and prevents surface cracking of the samples. Chemical analysis with FTIR measurements proved simultaneous chain scission and other crosslinking processes during QUV weathering. The samples with pF reinforcement showed less pronounced chemical degradation than the reference sample. DMA measurements showed an increase in glass transition temperature of up to 20 °C after the weathering. The storage modulus revealed pF reinforcement preservation even after 1000 h of weathering. Introduced pF ensured ductility and retention of the flexural and tensile properties. Two pF loadings (pF0.1% and pF0.5%) were chosen to evaluate the effect on materials' performance during weathering. The 0.1 wt% loading showed optimal performance for tensile properties, while a higher loading of 0.5 wt% benefitted flexural properties. The introduction of pF also came with drawbacks. Increased water uptake correlated with introduced pF loading, showing a 5-fold increase for a pF0.5% loaded sample (water contributed to less than 5 wt% of the total sample weight) compared to a 0% sample.

4. CONCLUSIONS

In the Doctoral Thesis research, 43 different UV-curable resin formulations were prepared with filler loading (0.1–30 wt%). Six different types of lignocellulose components (2 nanocrystalline cellulose, 2 nanofibrillated cellulose, hemicellulose, and lignin with variating biomass source, particle size, geometry, and surface functionalization) were successfully introduced into the vegetable oil-based resin formulation. Resin formulations were tested by coating/film photocuring processing and UV-light-assisted 3D printing fabrication. Single and hybrid filler approaches were evaluated. Acrylation and isocyanate (nanocellulose surface functionalization) were evaluated to improve matrix-filler interface interaction.

1. The addition of reactive diluents 1,6-hexanediol diacrylate and trimethylolpropane triacrylate into the soybean oil acrylate resin (AESO) resulted in increased double bond conversion rate (DBC%) by 10 %, increased thermal stability by 30 °C and storage modulus 4-fold at room temperature. Reactive diluents decreased viscosity, allowing the bio-based resin formulation to be validated for UV-assisted 3D printing showing excellent printing accuracy.

2. Performance properties improved further by introducing 5–30 wt% nanocrystalline cellulose, nanofibrillated cellulose, hemicellulose, and lignin as single and hybrid fillers. Hemicellulose increased glass transition temperature by 22 °C, and nanocrystalline cellulose most increased the storage modulus. Lignin reduced the DBC% down to 20 % and reduced surface hydrophilicity. Hybrid lignocellulose filler compositions, in turn, increased DBC%, reaching 80 % (resin with no fillers 82 %). Adjusting the hybrid filler composition allowed precise control of the sample surface morphology. Hybrid composition (C1F3H1, C3F1H1, and C2F3H1) showed higher storage modulus values than any of the 10 wt% single filler compositions. Adjusting the hybrid filler composition allowed precise control of the sample performance properties, surface morphology, etc.

3. Significant improvements in the overall mechanical performance of the 3D printed composite samples were observed with the introduction of ultra-low loading (down to 0.1 wt%) of nanofibrillated cellulose. The 0.1 wt% composite showed 1.6-fold, 2.4-fold, and 1.7-fold increases in tensile modulus, strength, and break strain, respectively. A 34 °C increase in glass transition indicated nanocellulose interaction with the polymer matrix. Additional FTIR analysis showed hydrogen bonding in the cured composite samples.

4. Nanocellulose surface functionalization improved filler-matrix compatibility – increased crosslinking density and interfacial adhesion. Functionalization resulted in a 1.77-fold and 2-fold reinforcement efficiency factor r increase in comparison to unfunctionalized nanofibrillated cellulose and nanocrystalline cellulose, respectively.

5. The introduction of nanofibrillated cellulose protected the 3D printed samples from cracking during the accelerated weathering. Nanocellulose reinforcement provided ductility and retention of the flexural and tensile properties after weathering.

REFERENCES

1. Market Trends on Bio-based and Plant-based Resins. Availabe online: https://coatings.specialchem.com/tech-library/article/market-trends-on-biobased-and-plant-based-resins (accessed on 2023 19 October).

2. Zhang, C.; Garrison, T. F.; Madbouly, S. A.; Kessler, M. R. Recent advances in vegetable oil-based polymers and their composites. *Progress in Polymer Science* **2017**, *71*, 91–143, doi:10.1016/j.progpolymsci.2016.12.009.

3. Meier, M. A. R.; Metzger, J. O.; Schubert, U.S. Plant oil renewable resources as green alternatives in polymer science. *Chemical Society Reviews* **2007**, *36*, 1788–1802, doi:10.1039/B703294C.

4. Su, Y.; Lin, H.; Zhang, S.; Yang, Z.; Yuan, T. One-Step Synthesis of Novel Renewable Vegetable Oil-Based Acrylate Prepolymers and Their Application in UV-Curable Coatings. *Polymers* **2020**, *12*, doi:10.3390/polym12051165.

5. Zhang, P.; Zhang, J. One-step acrylation of soybean oil (SO) for the preparation of SO-based macromonomers. *Green Chemistry* **2013**, *15*, 641-645, doi:10.1039/c3gc36961g.

6. Ma, Y.; Ye, Y.; Wan, H.; Chen, L.; Zhou, H.; Chen, J. Chemical modification of graphene oxide to reinforce the corrosion protection performance of UV-curable polyurethane acrylate coating. *Progress in Organic Coatings* **2020**, *141*, doi:10.1016/j.porgcoat.2020.105547.

7. Fu, J.; Yu, H.; Wang, L.; Lin, L.; Khan, R.U. Preparation and properties of UV-curable hyperbranched polyurethane acrylate hard coatings. *Progress in Organic Coatings* **2020**, *144*, doi:10.1016/j.porgcoat.2020.105635.

8. Huang, M.; Liu, Y.; Klier, J.; Schiffman, J.D. High-Performance, UV-Curable Cross-Linked Films via Grafting of Hydroxyethyl Methacrylate Methylene Malonate. *Industrial & Engineering Chemistry Research* **2020**, *59*, 4542–4548, doi:10.1021/acs.iecr.9b06618.

9. Zhang, T.; Jiang, B.; Huang, Y. Combined use of methacrylate/epoxy functionalized silanes for tuning of hyperbranched polysiloxane structure. *Materials Chemistry and Physics* **2020**, *254*, doi:10.1016/j.matchemphys.2020.123525.

10. Stouten, J.; Vanpoucke, D. E. P.; Van Assche, G.; Bernaerts, K. V. UV-Curable Biobased Polyacrylates Based on a Multifunctional Monomer Derived from Furfural. *Macromolecules* **2020**, *53*, 1388–1404, doi:10.1021/acs.macromol.9b02659.

11. Tajau, R.; Rohani, R.; Alias, M. S.; Mudri, N. H.; Abdul Halim, K. A.; Harun, M. H.; Mat Isa, N.; Che Ismail, R.; Muhammad Faisal, S.; Talib, M.; Rawi Mohamed Zin, M.; Izni Yusoff, I.; Khairul Zaman, N.; Asyila Ilias, I. Emergence of Polymeric Material Utilising Sustainable Radiation Curable Palm Oil-Based Products for Advanced Technology Applications. *Polymers (Basel)* **2021**, *13*, doi:10.3390/polym13111865.

12. Addis, C. C.; Koh, R. S.; Gordon, M. B. Preparation and characterization of a bio-based polymeric wood adhesive derived from linseed oil. *International Journal of Adhesion and Adhesives* **2020**, *102*, doi:10.1016/j.ijadhadh.2020.102655.

13. Tan, J.; Liu, B.; Fu, Q.; Wang, L.; Xin, J.; Zhu, X. Role of the Oxethyl Unit in the Structure of Vegetable Oil-Based Plasticizer for PVC: An Efficient Strategy to Enhance Compatibility and Plasticization. *Polymers* **2019**, *11*, doi:10.3390/polym11050779.

14. Singh, Y.; Sharma, A.; Singla, A. Non-edible vegetable oil-based feedstocks capable of bio-lubricant production for automotive sector applications-a review. *Environmental Science and Pollution Research* **2019**, *26*, 14867–14882, doi:10.1007/s11356-019-05000-9.

15. Volison-Klimentiev, A.; Cullari, L.; Shachar-Michaely, G.; Dor, S.; Peretz-Damari, S.; Afik, N.; Regev, O. Vegetable-Oil-Based Intelligent Ink for Oxygen Sensing. *ACS Sensors* **2020**, *5*, 3274–3280, doi:10.1021/acssensors.0c01777.

16. Rincón-Iglesias, M.; Lizundia, E.; Lanceros-Méndez, S. Water-Soluble Cellulose Derivatives as Suitable Matrices for Multifunctional Materials. *Biomacromolecules* **2019**, *20*, 2786–2795, doi:10.1021/acs.biomac.9b00574.

17. Hegde, M. B.; Mohana, K. N. A Sustainable and Eco-Friendly Polymer Based Graphene Oxide Nanocomposite Anti-Corrosion Coating on Mild Steel. *ChemistrySelect* **2020**, *5*, 1506–1515, doi:10.1002/slct.201904534.

18. Rosu, L.; Varganici, C. D.; Mustata, F.; Rosu, D.; Rosca, I.; Rusu, T. Epoxy Coatings Based on Modified Vegetable Oils for Wood Surface Protection against Fungal Degradation. *ACS Applied Materials & Interfaces* **2020**, *12*, 14443–14458, doi:10.1021/acsami.0c00682.

19. Galià, M.; de Espinosa, L. M.; Ronda, J. C.; Lligadas, G.; Cádiz, V. Vegetable oil-based thermosetting polymers. *European Journal of Lipid Science and Technology* **2010**, *112*, 87–96, doi:10.1002/ejlt.200900096.

20. Alam, M.; Akram, D.; Sharmin, E.; Zafar, F.; Ahmad, S. Vegetable oil based eco-friendly coating materials: A review article. *Arabian Journal of Chemistry* **2014**, *7*, 469–479, doi:10.1016/j.arabjc.2013.12.023.

21. Hermens, J. G. H.; Freese, T.; van den Berg, K. J.; van Gemert, R.; Feringa, B. L. A coating from nature. *Sci Adv* **2020**, *6*, doi:10.1126/sciadv.abe0026.

22. Dai, J.; Ma, S.; Wu, Y.; Zhu, J.; Liu, X. High bio-based content waterborne UV-curable coatings with excellent adhesion and flexibility. *Progress in Organic Coatings* **2015**, *87*, 197–203, doi:10.1016/j.porgcoat.2015.05.030.

23. Zhu, G.; Zhang, J.; Huang, J.; Yu, X.; Cheng, J.; Shang, Q.; Hu, Y.; Liu, C.; Hu, L.; Zhou, Y. High-performance 3D printing UV-curable resins derived from soybean oil and gallic acid. *Green Chemistry* **2021**, *23*, 5911–5923, doi:10.1039/D1GC01934A.

24. Standard SLA, DLP & LCD photopolymer resins for General Purpose applications. Availabe online: https://www.3dresyns.com/pages/standard-sla-dlp-lcd-photopolymer-resins-for-general-purpose-applications (accessed on 2023 15 March).

25. The toughest 3D-printing resins available. Availabe online: https://www.liqcreate.com/supportarticles/the-tough-3d-printing-resin-sla-dlp-lcd-msla/ (accessed on 2023 15 March).

26. Kousaalya, A. B. Sustainable Photo-curable Polymers in Additive Manufacturing Arena: A Review. In *Sustainability & Green Polymer Chemistry Volume 1: Green Products and Processes*, H. N. Cheng, Gross, R. A., Eds. American Chemical Society: 2020; Vol. 1, pp. 89–98.

27. Ma, S.; Jiang, Y.; Liu, X.; Fan, L.; Zhu, J. Bio-based tetrafunctional crosslink agent from gallic acid and its enhanced soybean oil-based UV-cured coatings with high performance. *RSC Advances* **2014**, *4*, 7, doi:10.1039/c4ra01311e.

28. Khot, S. N.; Lascala, J. J.; Can, E.; Morye, S. S.; Williams, G. I.; Palmese, G. R.; Kusefoglu, S. H.; Wool, R. P. Development and application of triglyceride-based polymers and composites. *Journal of Applied Polymer Science* **2001**, *82*, 703–723, doi:10.1002/app.1897.

29. Rosace, G.; Palucci Rosa, R.; Arrigo, R.; Malucelli, G. Photosensitive acrylates containing bio-based epoxy-acrylate soybean oil for 3D printing application. *Journal of Applied Polymer Science* **2021**, *138*, 51292–51303, doi:10.1002/app.51292.

30. Chandra, M. R. G. S.; Madakka, M. Comparative Biochemistry and Kinetics of Microbial Lignocellulolytic Enzymes. In *Recent Developments in Applied Microbiology and Biochemistry*, **2019,** 147–159.; doi:10.1016/b978-0-12-816328-3.00011-8.

31. Khan, M. U.; Usman, M.; Ashraf, M. A.; Dutta, N.; Luo, G.; Zhang, S. A review of recent advancements in pretreatment techniques of lignocellulosic materials for biogas production: Opportunities and Limitations. *Chemical Engineering Journal Advances* **2022**, *10*, 100263–100278, doi:10.1016/j.ceja.2022.100263.

32. Auclair, N.; Kaboorani, A.; Riedl, B.; Landry, V. Effects of surface modification of cellulose nanocrystals (CNCs) on curing behavior, optical, and thermal properties of soybean oil bio-nanocomposite. *Journal of Coatings Technology and Research* **2019**, *17*, 57–67, doi:10.1007/s11998-019-00237-y.

33. Auclair, N.; Kaboorani, A.; Riedl, B.; Landry, V.; Hosseinaei, O.; Wang, S. Influence of modified cellulose nanocrystals (CNC) on performance of bionanocomposite coatings. *Progress in Organic Coatings* **2018**, *123*, 27–34, doi:10.1016/j.porgcoat.2018.05.027.

34. Liu, Z.; Tisserat, B. H. Coating applications to natural fiber composites to improve their physical, surface and water absorption characters. *Industrial Crops and Products* **2018**, *112*, 196–199, doi:10.1016/j.indcrop.2017.12.002.

35. Poothanari, M. A.; Schreier, A.; Missoum, K.; Bras, J.; Leterrier, Y. Photocured Nanocellulose Composites: Recent Advances. *ACS Sustainable Chemistry & Engineering* **2022**, *10*, 3131–3149, doi:10.1021/acssuschemeng.1c07631.

36. Li, X.; Zhang, X.; Yao, S.; Chang, H.; Wang, Y.; Zhang, Z. UV-blocking, transparent and hazy cellulose nanopaper with superior strength based on varied components of poplar mechanical pulp. *Cellulose* **2020**, *27*, 6563–6576, doi:10.1007/s10570-020-03236-0.

37. Emmert, K.; Amberg-Schwab, S.; Braca, F.; Bazzichi, A.; Cecchi, A.; Somorowsky, F. bioORMOCER((R))-Compostable Functional Barrier Coatings for Food Packaging. *Polymers (Basel)* **2021**, *13*, 1257–1279, doi:10.3390/polym13081257.

38. Espinosa, E.; Bascon-Villegas, I.; Rosal, A.; Perez-Rodriguez, F.; Chinga-Carrasco, G.; Rodriguez, A. PVA/(ligno)nanocellulose biocomposite films. Effect of residual lignin content on structural, mechanical, barrier and antioxidant properties. *Int J Biol Macromol* **2019**, *141*, 197–206, doi:10.1016/j.ijbiomac.2019.08.262.

39. Mohamad Aini, N. A.; Othman, N.; Hussin, M. H.; Sahakaro, K.; Hayeemasae, N. Lignin as Alternative Reinforcing Filler in the Rubber Industry: A Review. *Frontiers in Materials* **2020**, *6*, doi:10.3389/fmats.2019.00329.

40. Barkane, A.; Platnieks, O.; Grase, L.; Gaidukovs, S. Simultaneous wettability and stiffness control of UV-curing vegetable oil resin composites by lignocellulosic components. *Polymer* **2022**, *255*, 125154–125164, doi:10.1016/j.polymer.2022.125154.

41. Gaidukovs, S.; Barkane, A. Chapter 16 Smart Wood-like Materials Based on Lignocellulose Nanoparticles. In *Cellulose Nanoparticles: Volume 1: Chemistry and Fundamentals*, The Royal Society of Chemistry: 2021; Vol. 1, pp. 402–423.

42. Dadhania, S. *3D Printing Materials Market 2022–2032*; IDTechEx: 2022.

43. Hull, C.W.; Arcadia, C. United States Patent (19) Hull (54) (75) (73) 21) 22 (51) 52) (58) (56) APPARATUS FOR PRODUCTION OF THREE-DMENSONAL OBJECTS BY STEREO THOGRAPHY. **1984**, US005485919A, doi:US005485919A.

44. van Wijk, A.; van Wijk, I. 3D printing with biomaterials: Towards a sustainable and circular economy. *3D Printing with Biomaterials: Towards a Sustainable and Circular Economy* **2015**, 10.3233/978-1-61499-486-2-i, 1-85, doi:10.3233/978-1-61499-486-2-i.

45. Chaunier, L.; Guessasma, S.; Belhabib, S.; Della Valle, G.; Lourdin, D.; Leroy, E. Material extrusion of plant biopolymers: Opportunities & challenges for 3D printing. *Additive Manufacturing* **2018**, *21*, 220–233, doi:10.1016/j.addma.2018.03.016.

46. Lawrence, W. H.; Bass, G. E.; Purcell, W. P.; Autian, J. Use of Mathematical Models in the Study of Structure-Toxicity Relationships of Dental Compounds: I. Esters of Acrylic and Methacrylic Acids. *Journal of Dental Research* **1972**, *51*, 526–535, doi:10.1177/00220345720510024701.

47. Voet, V. S. D.; Guit, J.; Loos, K. Sustainable Photopolymers in 3D Printing: A Review on Biobased, Biodegradable, and Recyclable Alternatives. *Macromol Rapid Commun* **2021**, *42*, e2000475, doi:10.1002/marc.202000475.

48. Maines, E. M.; Porwal, M. K.; Ellison, C. J.; Reineke, T. M. Sustainable advances in SLA/DLP 3D printing materials and processes. *Green Chemistry* **2021**, *23*, 6863–6897, doi:10.1039/D1GC01489G.

49. Glaskova-Kuzmina, T.; Starkova, O.; Gaidukovs, S.; Platnieks, O.; Gaidukova, G. Durability of Biodegradable Polymer Nanocomposites. *Polymers (Basel)* **2021**, *13*, doi:10.3390/polym13193375.

50. Barkane, A.; Kampe, E.; Platnieks, O.; Gaidukovs, S. Cellulose Nanocrystals vs. Cellulose Nanofibers: A Comparative Study of Reinforcing Effects in UV-Cured Vegetable Oil Nanocomposites. *Nanomaterials* **2021**, *11*, 1791–1809, doi:10.3390/nano11071791.

51. Starkova, O.; Platnieks, O.; Sabalina, A.; Gaidukovs, S. Hydrothermal Ageing Effect on Reinforcement Efficiency of Nanofibrillated Cellulose/Biobased Poly(butylene succinate) Composites. *Polymers (Basel)* **2022**, *14*, doi:10.3390/polym14020221.

52. Piras, C. C.; Fernandez-Prieto, S.; De Borggraeve, W. M. Nanocellulosic materials as bioinks for 3D bioprinting. *Biomater Sci* **2017**, *5*, 1988–1992, doi:10.1039/c7bm00510e.

53. Palaganas, N. B.; Mangadlao, J. D.; de Leon, A. C. C.; Palaganas, J. O.; Pangilinan, K. D.; Lee, Y. J.; Advincula, R. C. 3D Printing of Photocurable Cellulose Nanocrystal Composite for Fabrication of Complex Architectures via Stereolithography. *ACS Applied Materials & Interfaces* **2017**, *9*, 34314–34324, doi:10.1021/acsami.7b09223.

54. Palucci Rosa, R.; Rosace, G.; Arrigo, R.; Malucelli, G. Preparation and Characterization of 3D-Printed Biobased Composites Containing Micro- or Nanocrystalline Cellulose. *Polymers (Basel)* **2022**, *14*, doi:10.3390/polym14091886.

55. Vidakis, N.; Petousis, M.; Michailidis, N.; Kechagias, J. D.; Mountakis, N.; Argyros, A.; Boura, O.; Grammatikos, S. High-performance medical-grade resin radically reinforced with cellulose nanofibers for 3D printing. *Journal of the Mechanical Behavior of Biomedical Materials* **2022**, *134*, doi:10.1016/j.jmbbm.2022.105408.

56. Xu, X.; Liu, F.; Jiang, L.; Zhu, J.Y.; Haagenson, D.; Wiesenborn, D.P. Cellulose Nanocrystals vs. Cellulose Nanofibrils: A Comparative Study on Their Microstructures and Effects as Polymer Reinforcing Agents. *ACS Applied Materials & Interfaces* **2013**, *5*, 2999–3009, doi:10.1021/am302624t.

57. Hakimi, N. M. F.; Lee, S. H.; Lum, W. C.; Mohamad, S. F.; Osman Al Edrus, S. S.; Park, B. D.; Azmi, A. Surface Modified Nanocellulose and Its Reinforcement in Natural Rubber Matrix Nanocomposites: A Review. *Polymers (Basel)* **2021**, *13*, doi:10.3390/polym13193241.

58. Lasenko, I.; Grauda, D.; Butkauskas, D.; Sanchaniya, J.V.; Viluma-Gudmona, A.; Lusis, V. Testing the Physical and Mechanical Properties of Polyacrylonitrile Nanofibers Reinforced with Succinite and Silicon Dioxide Nanoparticles. *Textiles* **2022**, *2*, 162–173, doi:10.3390/textiles2010009.

59. Zwawi, M. A Review on Natural Fiber Bio-Composites, Surface Modifications and Applications. *Molecules (Basel, Switzerland)* **2021**, *26*, 404, doi:10.3390/molecules26020404.

60. Redondo, A.; Mortensen, N.; Djeghdi, K.; Jang, D.; Ortuso, R. D.; Weder, C.; Korley, L. T. J.; Steiner, U.; Gunkel, I. Comparing Percolation and Alignment of Cellulose Nanocrystals for the Reinforcement of Polyurethane Nanocomposites. *ACS Applied Materials & Interfaces* **2022**, *14*, 7270–7282, doi:10.1021/acsami.1c21656.

61. Giri, J.; Adhikari, R. A Brief review on extraction of nanocellulose and its application. *BIBECHANA* **2012**, *9*, 81–87, doi:10.3126/bibechana.v9i0.7179.

62. Wang, B.; Ding, G.; Chen, K.; Jia, S.; Wei, J.; Wang, Y.; He, R.; Shao, Z. A physical and chemical double enhancement strategy for 3D printing of cellulose reinforced nanocomposite. *Journal of Applied Polymer Science* **2020**, *137*, doi:10.1002/app.49164.

63. Mekonnen, T. H.; Haile, T.; Ly, M. Hydrophobic functionalization of cellulose nanocrystals for enhanced corrosion resistance of polyurethane nanocomposite coatings. *Appl. Surf. Sci.* **2021**, *540*, 148299, doi:10.1016/j.apsusc.2020.148299.

64. Maturi, M.; Spanu, C.; Fernández-Delgado, N.; Molina, S. I.; Comes Franchini, M.; Locatelli, E.; Sanz de León, A. Fatty acid – functionalized cellulose nanocomposites for vat photopolymerization. *Addit. Manuf.* **2023**, *61*, 103342, doi:10.1016/j.addma.2022.103342.

65. Q-Lab. QUV. Corporation, Q.-L., Ed. 2022.

66. Chiantore, O.; Trossarelli, L.; Lazzari, M. Photooxidative degradation of acrylic and methacrylic polymers. *Polymer* **2000**, *41*, 1657–1668, doi:10.1016/S0032-3861(99)00349-3.

67. Decker, C.; Zahouily, K.; Valet, A. Weathering Performance of Thermoset And Photoset Acrylate Coatings. *Journal of Coatings Technology* **2002**, *74*, 87–92, doi:10.1007/BF02720154.

68. Nowrouzi, Z.; Mohebby, B.; Ebrahimi, M.; Petrič, M. Weathering performance of thermally modified wood coated with polyacrylate containing olive leaf extract as a bio-based additive. *European Journal of Wood and Wood Products* **2021**, *79*, 1551–1562, doi:10.1007/s00107-021-01712-3.

69. Decker, C.; Zahouily, K. Photodegradation and photooxidation of thermoset and UV-cured acrylate polymers. *Polymer Degradation and Stability* **1999**, *64*, 293–304, doi:10.1016/S0141-3910(98)00205-5.

70. Sung, L.-P.; Jasmin, J.; Gu, X.; Nguyen, T.; Martin, J. W. Use of laser scanning confocal microscopy for characterizing changes in film thickness and local surface morphology of UV-exposed polymer coatings. *Journal of Coatings Technology and Research* **2004**, *1*, 267–276, doi:10.1007/s11998-004-0029-8.

71. Decker, C.; Masson, F.; Schwalm, R. Weathering resistance of waterbased UV-cured polyurethane-acrylate coatings. *Polymer Degradation and Stability* **2004**, *83*, 309–320, doi:10.1016/s0141-3910(03)00276-3.

72. Firdous, H.; Madhu, B.; Habib, F.; Bajpai, M.; Firdous, H.; Madhu, B. Synthesis and Characterization of Acrylated Epoxidized Soybean Oil for UV Cured Coatings. *Chemistry & Chemical Technology* **2011**, *5*, 1–10.

73. Tehfe, M.; Louradour, F.; Lalevée, J.; Fouassier, J.-P. Photopolymerization Reactions: On the Way to a Green and Sustainable Chemistry. *Applied Sciences* **2013**, *3*, 490–514, doi:10.3390/app3020490.

74. Kunwong, D.; Sumanochitraporn, N.; Kaewpirom, S. Curing behavior of a UV-curable coating based on urethane acrylate oligomer: The influence of reactive monomers. *Songklanakarin Journal of Science and Technology* **2011**, *33*, 201–207.

75. Qian, Y. Q.; Han, N.; Bo, Y. W.; Tan, L. L.; Zhang, L. F.; Zhang, X. X. Homogeneous synthesis of cellulose acrylate-g-poly (n-alkyl acrylate) solid-solid phase change materials via free radical polymerization. *Carbohydr Polym* **2018**, *193*, 129–136, doi:10.1016/j.carbpol.2018.03.057.

76. Bojanić, V., Jovanović, S., Tabaković, R., Tabaković, I. Synthesis and electrochemistry of grafted copolymers of cellulose with 4-vinylpyridine, 1-vinylimidazole, 1-vinyl-2-pyrrolidinone, and 9-vinylcarbazole. *J. Appl. Polym. Sci.* **1996**, *60*, 1719–1725, doi:10.1002/(sici)1097-4628(19960606)60:10<1719::aid-app24>3.0.co;2-y.

77. Chen, Z.; Xiao, P.; Zhang, J.; Tian, W.; Jia, R.; Nawaz, H.; Jin, K.; Zhang, J. A facile strategy to fabricate cellulose-based, flame-retardant, transparent and anti-dripping protective coatings. *Chemical Engineering Journal* **2020**, *379*, doi:10.1016/j.cej.2019.122270.

78. Gafurov, T. G.; Pilosov, M. Y.; Adylov, A.; Mannanova, D.; Suvorova, Y. V.; Tashpulatov, Y.T.; Nikonovich, G.V.; Usmanov, K.U. The reaction of cellulose with hexamethylene diisocyanate. *Polym. Sci. U.S.S.R.* **1970**, *12*, 2848–2853, doi:10.1016/0032-3950(70)90430-2.

79. Barkane, A.; Platnieks, O.; Jurinovs, M.; Kasetaite, S.; Ostrauskaite, J.; Gaidukovs, S.; Habibi, Y. Uv-light curing of 3d printing inks from vegetable oils for stereolithography. *Polymers* **2021**, *13*, doi:10.3390/polym13081195.

80. Gaidukovs, S.; Zukulis, E.; Bochkov, I.; Vaivodiss, R.; Gaidukova, G. Enhanced mechanical, conductivity, and dielectric characteristics of ethylene vinyl acetate copolymer composite filled with carbon nanotubes. *Journal of Thermoplastic Composite Materials* **2017**, *31*, 1161–1180, doi:10.1177/0892705717734603.

81. Sharma, A.; Thakur, M.; Bhattacharya, M.; Mandal, T.; Goswami, S. Commercial application of cellulose nano-composites – A review. *Biotechnol Rep (Amst)* **2019**, *21*, e00316, doi:10.1016/j.btre.2019.e00316.

82. Kong, D.; Meng, Y.; McKenna, G. B. Determination of the molecular weight between cross-links for different ambers: Viscoelastic measurements of the rubbery plateau*. *Polymer Engineering & Science* **2022**, *62*, 1023–1040, doi:10.1002/pen.25903.

83. Pelletier, H.; Belgacem, N.; Gandini, A. Acrylated vegetable oils as photocrosslinkable materials. *Journal of Applied Polymer Science* **2006**, *99*, 3218–3221, doi:10.1002/app.22322.

84. Mysiukiewicz, O.; Kosmela, P.; Barczewski, M.; Hejna, A. Mechanical, Thermal and Rheological Properties of Polyethylene-Based Composites Filled with Micrometric Aluminum Powder. *Materials* **2020**, *13*, 1242.

85. Essien, C.; Via, B. K.; Cheng, Q.; Gallagher, T.; McDonald, T.; Wang, X.; Eckhardt, L.G. Multivariate modeling of acoustomechanical response of 14-year-old suppressed loblolly pine (Pinus taeda) to variation in wood chemistry, microfibril angle and density. *Wood Science and Technology* **2017**, *51*, 475–492, doi:10.1007/s00226-017-0894-9.

86. Maalihan, R. D.; Chen, Q.; Tamura, H.; Sta. Agueda, J. R. H.; Pajarito, B. B.; Caldona, E. B.; Advincula, R. C. Mechanically and Thermally Enhanced 3D-Printed Photocurable Polymer Nanocomposites Containing Functionalized Chitin Nanowhiskers by Stereolithography. *ACS Applied Polymer Materials* **2022**, *4*, 2513–2526, doi:10.1021/acsapm.1c01816.

87. Jesuarockiam, N.; Jawaid, M.; Zainudin, E .S.; Thariq Hameed Sultan, M.; Yahaya, R. Enhanced Thermal and Dynamic Mechanical Properties of Synthetic/Natural Hybrid Composites with Graphene Nanoplateletes. *Polymers (Basel)* **2019**, *11*, 1085–1103, doi:10.3390/polym11071085.

88. Naveen, J.; Jawaid, M.; Zainudin, E. S.; Sultan, M. T. H.; Yahaya, R.; Abdul Majid, M. S. Thermal degradation and viscoelastic properties of Kevlar/Cocos nucifera sheath reinforced

epoxy hybrid composites. *Composite Structures* **2019**, *219*, 194–202, doi:10.1016/j.compstruct.2019.03.079.

89. Sung, J.; Sun, X. S. Cardanol modified fatty acids from camelina oils for flexible bio-based acrylates coatings. *Progress in Organic Coatings* **2018**, *123*, 242–253, doi:10.1016/j.porgcoat.2018.02.008.

90. Huang, J.; Zhou, J.; Liu, M. Interphase in Polymer Nanocomposites. *JACS Au* **2022**, doi:10.1021/jacsau.1c00430.

91. Mohan, D.; Sajab, M. S.; Kaco, H.; Bakarudin, S.B.; Noor, A.M. 3D Printing of UV-Curable Polyurethane Incorporated with Surface-Grafted Nanocellulose. *Nanomaterials (Basel)* **2019**, *9*, 1726–1741, doi:10.3390/nano9121726.

92. Verdolotti, L.; Stanzione, M.; Khlebnikov, O.; Silant'ev, V.; Postnova, I.; Lavorgna, M.; Shchipunov, Y. Dimensionally Stable Cellulose Aerogel Strengthened by Polyurethane Synthesized In Situ. *Macromolecular Chemistry and Physics* **2019**, *220*, 1800372, doi:10.1002/macp.201800372.

93. Shen, Z.; Zheng, L.; Song, D.; Liu, Y.; Li, C.; Liu, J.; Xiao, Y.; Wu, S.; Zhou, T.; Zhang, B., et al. A Non-Isocyanate Route to Poly(Ether Urethane): Synthesis and Effect of Chemical Structures of Hard Segment. *Polymers* **2022**, *14*, 2039.

94. Stenstad, P.; Andresen, M.; Tanem, B.S.; Stenius, P. Chemical surface modifications of microfibrillated cellulose. *Cellulose* **2008**, *15*, 35–45, doi:10.1007/s10570-007-9143-y.

95. Stern, T. Side-reactions in diisocyanate-derived bulk polyurea synthesis. *J. Appl. Polym. Sci.* **2020**, *137*, 49034, doi:10.1002/app.49034.

96. Tenorio-Alfonso, A.; Sánchez, M. C.; Franco, J. M. Preparation, Characterization and Mechanical Properties of Bio-Based Polyurethane Adhesives from Isocyanate-Functionalized Cellulose Acetate and Castor Oil for Bonding Wood. *Polymers* **2017**, *9*, 132.

97. Fareghi, A. R.; Moghadam, P. N.; Khalafy, J.; Bahram, M.; Moghtader, M. Preparation of a new molecularly imprinted polymer based on self-crosslinkable cellulose acrylate in aqueous solution: A drug delivery system for furosemide. *J. Appl. Polym. Sci.* **2017**, *134*, 45581, doi:10.1002/app.45581.

98. Kletetschka, K.; Rimstidt, J. D.; Long, T. E.; Michel, F. M. Suitability of 3D-Printed devices for low-temperature geochemical experiments. *Appl. Geochem.* **2018**, *98*, 121–126, doi:10.1016/j.apgeochem.2018.08.012.

99. Liu, Z.; Knetzer, D. A.; Wang, J.; Chu, F.; Lu, C.; Calvert, P. D. 3D printing acrylated epoxidized soybean oil reinforced with functionalized cellulose by UV curing. *Journal of Applied Polymer Science* **2021**, *139*, 51561–51571, doi:10.1002/app.51561.

100. Noè, C.; Cosola, A.; Tonda-Turo, C.; Sesana, R.; Delprete, C.; Chiappone, A.; Hakkarainen, M.; Sangermano, M. DLP-printable fully biobased soybean oil composites. *Polymer* **2022**, *247*, 124779, doi:10.1016/j.polymer.2022.124779.

101. Seabra, C. P.; Sousa, A. C.; Bragança, I. M. F.; Silva, C. M. A.; Robalo, M. P.; Loja, M. A. R.; Martins, P. A. F. On the Performance and Recyclability of a Green Composite Based on AESO Resin. *J. Manuf. Mater. Process.* **2020**, *4*, 65, doi:10.3390/jmmp4030065.

102. Gojzewski, H.; Guo, Z.; Grzelachowska, W.; Ridwan, M. G.; Hempenius, M. A.; Grijpma, D. W.; Vancso, G. J. Layer-by-Layer Printing of Photopolymers in 3D: How Weak is the Interface? *ACS Appl Mater Interfaces* **2020**, *12*, 8908–8914, doi:10.1021/acsami.9b22272.

103. Meng, L.; Li, S.; Yang, W.; Simons, R.; Yu, L.; Liu, H.; Chen, L. Improvement of Interfacial Interaction between Hydrophilic Starch Film and Hydrophobic Biodegradable Coating. *ACS*

Sustainable Chemistry & Engineering **2019**, *7*, 9506–9514, doi:10.1021/acssuschemeng.9b00909.

104. Lamm, M. E.; Wang, L.; Kishore, V.; Tekinalp, H.; Kunc, V.; Wang, J.; Gardner, D. J.; Ozcan, S. Material Extrusion Additive Manufacturing of Wood and Lignocellulosic Filled Composites. *Polymers* **2020**, *12*, doi:10.3390/polym12092115.

105. Briede, S.; Barkane, A.; Jurinovs, M.; Thakur, V. K.; Gaidukovs, S. Acrylation of biomass: a review of synthesis process – know how and future application directions. *Current Opinion in Green and Sustainable Chemistry* **2022**, doi:10.1016/j.cogsc.2022.100626.

106. Shanti, R.; Hadi, A. N.; Salim, Y. S.; Chee, S. Y.; Ramesh, S.; Ramesh, K. Degradation of ultra-high molecular weight poly(methyl methacrylate-co-butyl acrylate-co-acrylic acid) under ultra violet irradiation. *RSC Advances* **2017**, *7*, 112–120, doi:10.1039/c6ra25313j.

107. Oliveira, M. S.; da Luz, F. S.; da Costa Garcia Filho, F.; Pereira, A. C.; de Oliveira Aguiar, V.; Lopera, H. A. C.; Monteiro, S. N. Dynamic Mechanical Analysis of Thermally Aged Fique Fabric-Reinforced Epoxy Composites. *Polymers (Basel)* **2021**, *13*, doi:10.3390/polym13224037.

108. Rocha, I. B. C. M.; Raijmaekers, S.; Nijssen, R. P. L.; van der Meer, F. P.; Sluys, L. J. Hygrothermal ageing behaviour of a glass/epoxy composite used in wind turbine blades. *Composite Structures* **2017**, *174*, 110–122, doi:10.1016/j.compstruct.2017.04.028.

Anda Barkāne was born in 1994 in Riga. She obtained a Bachelor's degree in Chemical Technology (2018) and a Master's degree in Nanotechnologies (2020) from Riga Technical University (RTU). Since 2018, she has been a scientific assistant at the Polymer Materials Institute of the Faculty of Material Science and Applied Chemistry of RTU and since 2020, a researcher. Currently, she is a researcher at the Institute of Chemistry and Chemical Technology of the Faculty of Natural Sciences and Technologies, of RTU and Head of the RTU Doctoral School. Parallel to her bachelor's studies, Anda was actively involved in the Student Parliament of RTU, where she was head of the Science Department and the coordinator of the Latvian Student Association's Science Fund. During her bachelor's studies, Anda completed an internship at Sakret Plus JSC.

She has participated in several research projects and has received RTU Doctoral Grants, a grant for PhD students and academic personnel of Riga Technical University and BA School of Business and Finance in the strategic fields of specialization. Anda is a laureate of the L'Oréal-UNESCO For Women in Science Young Talents Program – Baltic, with the support of the Latvian National Commission for UNESCO and the Latvian Academy of Sciences award. She has supervised the development of four bachelor's theses and has been actively involved in academic work, teaching various courses.

Anda specializes in photopolymer synthesis, working on resin formulation, photopolymerization studies, composite development, and 3D printing technologies. Her research focuses on the development of bio-based resin formulations and lignocellulose as fillers.